Influence of variable oxidation states of certain metals on the adsorption, electrokinetic and photocatalytic properties of M^{+n}-TiO_2 nanocatalysts

A Thesis
Submitted for the partial fulfilment of the requirements for the award of the degree of

DOCTOR OF PHILOSOPHY

Submitted by

Sakshi Bhardwaj

(Regn. No. 901509019)

Under the Supervision of

Dr. Bonamali Pal

(Professor, SCBC)

SCHOOL OF CHEMISTRY AND BIOCHEMISTRY
THAPAR INSTITUTE OF ENGINEERING AND TECHNOLOGY,
PATIALA-147004
PUNJAB (INDIA)

JULY-2020

Certificate

This is to certify that the thesis entitled ***"Influence of variable oxidation states of certain metals on the adsorption, electrokinetic and photocatalytic properties of M^{+n}-TiO_2 nanocatalysts"***, is being submitted by **Miss Sakshi Bhardwaj** in fulfillment of the requirement for the award of Degree of Doctor of Philosophy to the School of Chemistry and Biochemistry, Thapar Institute of Engineering and Technology, Patiala. It is a record of the candidate's own work carried out by her under our supervision and guidance. The matter presented in this thesis has not been submitted in part or full for the award of any degree in any other University or Institute.

Dr. Bonamali Pal
(Professor and Supervisor)

Dr. Amjad Ali
(Professor and Head)
School of Chemistry and Biochemistry
Thapar Institute of Engineering and Technology,
Patiala - 147004
Punjab (India)

Candidate's declaration

I, hereby declare that the work presented in the thesis entitled ***"Influence of variable oxidation states of certain metals on the adsorption, electrokinetic and photocatalytic properties of M^{+n}-TiO_2 nanocatalysts"***, in fulfillment of the requirement for the award of the Degree of Doctor of Philosophy, is an authentic record of my own work carried out under the supervision of Dr. Bonamali Pal, Professor and Supervisor, School of Chemistry and Biochemistry, Thapar Institute of Engineering and Technology, Patiala, India. The matter embodied in this thesis has not been submitted in part or full to any other university or institute for the award of any degree in India or abroad.

Sakshi

Sakshi Bhardwaj

Dr. Bonamali Pal

(Professor and Supervisor)

Dedicated to
my Parents

Acknowledgements

First and above all, I thank the **Lord Almighty** to whom I owe my very existence for providing me this opportunity and granting me the capability to proceed successfully. I am grateful for his provision of joys, challenges and grace for growth that have been bestowed upon me during this research work, and indeed, throughout my life.

With immense gratitude and profound thanks, I acknowledge the support and help of my guide and supervisor **Dr. Bonamali Pal** in completing this thesis. His excellent guidance, priceless advices, insightful discussion, constant encouragement, profuse assistance, skillful suggestions and continuous support throughout the experimental and thesis works are the basis for the success of this research. With deepest gratitude, I acknowledge my guide for picking me up as one of his research students and providing me an excellent experimental atmosphere for completing the research work in time. In fact, the encouragement, support and freedom rendered by him provided me a lot of opportunity to build my confidence in accomplishing the experimental work successfully.

I am also indebted to **Dr. Satnam Singh** for correcting me at every stage of writing and supporting all the time in every aspect.

My sincere thanks to **Dr. Amjad Ali**, Professor and Head, School of Chemistry and Biochemistry, Thapar Institute of Engineering and Technology, Patiala. I am highly indebted to my doctoral committee members; **Dr. O. P. Pandey, Dr. Susheel Mittal** and **Dr. Soumen Basu** for their timely valuable suggestions. I extend my thanks to **Mr. Chander Thakur** and **Mr. Mayank Sharma** for their help and support every time.

I want to thank Dean R & SP **Dr. Rafat Siddique** and **Thapar Institute of Engineering and Technology** for continuous help and financial assistance for this research work.

I am highly thankful to **Dr. Joginder Rohilla** for giving me right direction and pushing me positively towards success.

With deep sense of gratitude, I thank **Dr. Ranjana Prakash** and **Dr. Tejo Prakash** for providing me moral support and encouragement throughout my research work.

I would like to acknowledge my research colleagues **Manpreet Kaur, Samriti Thakur, Aadil Bathla** and my **seniors and juniors Pooja Kumari, Manjusha, Harpreet Kaur, Karanveer** for their help and support in doing laboratory work and providing cheerful company.

The help from all the analytical laboratories and institutes such as **SAI labs, TIET, Patiala, Avantha Centre for Industrial R & D, Yamunanagar, IIT Bombay, Sprint testing solutions** is highly acknowledged. I also want to appreciate the support by **Dr. Banibrata Maity** for the analysis purpose.

I wish to thank my best friends **Sudesh, Deepti, Archana** for their love, care and moral support especially at times when things were going tough.

Sudesh deserves a special mention for being always there when no one was. I owe you for being unselfishly helping me every time and in any situation of life and research too.

Words fall short to express my gratitude for my parents; **Manju Bhardwaj** and **Sushil Kumar Bhardwaj,** for having faith in me and letting me do the things the way I wanted to. I salute you for all the love, care, sacrifices and pains you suffered to shape my life. I want to express my thanks to my loving brother **Parth Bhardwaj** for always cheering my mood in bad times. You always played the role of an encouraging and positive energy factor for me.

I am fortunate to acknowledge my Late grandfather **Om Prakash Bhardwaj** in heaven who must have been praying and blessing me all the times. I thank my grandmother **Jagati Bhardwaj** for her blessings and wishes to gain success by me. I will never be able to repay their affection and love towards me.

Special thanks to my sister **Isha Joshi,** jiju **Jatin Joshi** for their love, care and valuable suggestions which uplifted my moral in crucial times. I appreciate my little nephew **Arjunveer Joshi** and Niece **Akshdha Joshi** for keeping my mood alive and happy always.

My heartfelt regard goes to my mother in law **Neelam Sharma**, father in law **Arun Sharma** and brother in law **Dushyant Sharma** for their care and moral support which strengthened me always. I appreciate their support by maintaining a positive environment around me in difficult times.

My final and most special thanks goes to the love of my life **Sidharth Sharma** who always encouraged, appreciated and supported me in every aspect. Your continuous faith,

suggestions and enthusiastic words always pushed me towards the success of this work. This work was not possible without your presence in my life. I am lucky to have you as a life partner.

Table of contents

Chapter 1
Introduction and literature

Chapter 2

SECTION - 2A

To study the effect of variable oxidation states of Mn(II/VII)-TiO_2 photocatalysts on electrokinetic, surface structural and photocatalytic properties

SECTION - 2B

Effective photooxidative degradation of methyl viologen using Mn^{2+}/Mn^{7+}-TiO_2 nanocomposites under solar irradiation

Chapter 3

Improved charge carrier dynamics and catalyst substrate associations as a consequence of different oxidation states of Cr^{n+}-TiO_2 nanocomposites

List of abbreviations

UV	Ultravoilet
VB	Valence band
CB	Conduction band
E_f	Fermi energy level
M^{+n}	Metal ions
PR	Photoreduction
PO	Photooxidation
NPs	Nanoparticles
M	Metal
PZC	Point of zero charge
IEP	Isoelectric point
DI	Distilled water
DRS	Diffuse reflectance spectroscopy
PL	Photoluminescence
DLS	Dynamic Light Scattering
PCD	Particle charge detector
SEM-EDS	Scanning electron microscopy and energy dispersive spectroscopy
TEM	Transmission electron microscopy
HRTEM	High resolution transmission electron microscopy
XPS	X-ray photoelectron spectroscopy
XRD	X-ray diffractometry
SAXS	Small angle x-ray scattering

TPD	Temperature Programmed Desorption
SPR	Surface plasmon resonance
a.u.	Arbitrary unit
nm	Nanometer
mL	Millilitre
mM	Millimolar
mg	Milligram
mA	Milliampere
mm	Millimeter
cm	Centimeter
kV	Kilovolt
µL	Microlitre
µM	Micromolar
µg/mL	Microgram per millilitre
µeq/g	Microequivalent per gram
wt%	Weight percent
vol%	Volume percent
mW/cm^2	Milliwatt per centimeter square

List of symbols

TiO_2	Titanium dioxide
H_2O	Water
$OH^{\cdot}$	Hydroxyl radicals
$O_2^{\cdot}$	Superoxide radicals
e^-	Electrons
h^+	Holes
E_g	Band gap energy
ζ	Zeta potential
τ_{av}	Average lifetime
A°	Angstrom
°	Degree
λ	Wavelength
%	Percentage
θ	Theta
μ	Micro
ν	Frequency
g	Gram
m	Meter
°C	Degree celsius

Abstracts

Chapter 1

This chapter describes the function of various metal/metal ions (M/M^{+n}) as co-catalysts and their role in enhancing the catalytic or photocatalytic reaction mechanisms. The importance of variable oxidation states of some metals and their impact on the interfacial, electrokinetic and surface properties of catalysts has been discussed. Further, how these M/M^{+n} co-catalysts improve the optical, band gap, surface structural and heterojunction behaviour of TiO_2 has been elaborated. In this respect, realized research gaps have been mentioned and related methodologies adopted to complete the objectives have been presented.

Chapter 2

Section 2A

This work signifies the importance of oxidation state and ionic size of Mn(II) and Mn(VII) co-catalyst impregnated TiO_2 for the observed electrokinetic, adsorption and photocatalytic properties of Mn^{+n}-TiO_2 nanocatalysts. Due to difference in net electronic charge and ionic size of Mn(II) and Mn(VII) ions, the zeta potential, streaming potential and surface charge demand of Mn(II)-TiO_2 and Mn(VII)-TiO_2 nanocomposites are greatly varied. The absorption edge of Mn^{+n}-TiO_2 nanocatalysts revealed the red shift (515 nm to 550 nm) with increased oxidation state (II to VII) of Mn^{+n} due to $^6A_{1g} \rightarrow {}^4T_{1g}$ transition. The photoluminescence (404-530 nm) of Mn(II)-TiO_2 is highly quenched relative to Mn(VII)-TiO_2 during 340 nm excitation. HRTEM analysis showed the presence of Mn(VII) (~ 20-45 nm) and Mn(II) (~ 40-60 nm) nanodeposits over TiO_2 surface. Formation of new crystal phases (orthorhombic) in Mn(VII)-TiO_2 and Mn(II)-TiO_2 catalyst (tetragonal and orthorhombic) provided different photocatalytic efficiencies. Binding energies at 639.1 and 640.3 eV confirmed the presence of Mn in (0) and (II) oxidation state for Mn(II)-TiO_2 and 646 eV alongwith a satellite peak for Mn(VII)-TiO_2 co-catalyst. As a result, the adsorption and photocatalytic degradation of cationic (Fuchsin blue and methylene blue) and anionic (Salicylic acid and Salicylaldehyde) substrates by Mn^{+n}-TiO_2 nanocatalysts are notably improved relative to bare TiO_2 depending on their respective surface morphological features. It is observed that Mn(VII)-TiO_2 display higher adsorption capacity (0.049 μmol) and photodegradation rate (0.015 and 0.126×10^{-3}

min^{-1}) for cationic fuchsin blue and methylene blue dye, respectively, than Mn(II)-TiO_2 nanocatalyst under visible light irradiation.

Section 2B

Transition metal/metal ions are reported to impart very efficient co-catalytic activity to TiO_2 for various photocatalytic reactions depending on the nature and oxidation state of metal ions. However, when certain metals (M^{n+}) having different oxidation states like Mn^{2+}/Mn^{7+} or Cr^{3+}/Cr^{6+} act as co-catalysts, the photocatalytic properties of M^{n+}-TiO_2 nanocomposites may vary significantly. Different surface morphologies, electron transfer phenomena and adsorption efficacy provided by these co-catalysts will govern the M^{n+}-TiO_2 photoactivity. In this context, this study demonstrates the preparation and characterization of Mn^{2+}/Mn^{7+}-TiO_2 nanocomposites for investigating the above physicochemical properties for the degradation of toxic herbicide Methyl viologen under sunlight irradiation. The optical spectra of these catalysts showed bathochromic shifts (from 355 to 572 nm) due to the presence of Mn^{2+} and Mn^{7+} ions. The higher co-catalyst stability, smaller D_{max} (maximum average diameter) and mixed morphological characteristics have been illustrated by SAXS and TEM analysis with size range ~ 25-30 and 20-35 nm for Mn^{2+}-TiO_2 and Mn^{7+}-TiO_2 nanocomposites, respectively. The adsorption-desorption studies using NH_3 gas revealed that Mn^{7+} ions generate enhanced Lewis acidity on the co-catalyst surface compared to Mn^{2+} impregnations. The best fit for Freundlich adsorption isotherm (K_f = 23.44 μg/mg) was possessed by Mn^{7+}-TiO_2 than Mn^{2+}-TiO_2 and TiO_2 photocatalyst confirming its higher substrate affinity and photodegradation efficiency. The Mn^{2+} and Mn^{7+} impregnations displayed 2.6 and 3.7 times higher photoactivity than bare TiO_2 which has been correlated to different oxidation states and surface structural properties imparted by Mn^{n+} ions.

Chapter 3

The present work focuses on the effect of different oxidation states of impregnated Cr^{n+} ionic species over TiO_2 surface. The resulting Cr^{n+}-TiO_2 nanocomposites have been revealed to have improved optical response, charge carrier relaxation dynamics, adsorption and photocatalytic behaviour which is correlated to variable oxidation states of these composite materials. The optical absorption spectra (400-500 nm and 583-800 nm) covered the entire visible region after Cr^{n+} incorporation to have maximum photoresponse. These bands have

been assigned to the $^4A_{2g} \rightarrow {}^4T_{1g}$ and $^4A_{2g} \rightarrow {}^4T_{2g}$ transitions, respectively. A remarkable quenching of photoluminescence peaks and further successive enhanced carrier relaxations from 3.62 ns (bare TiO_2) to 3.73 and 4.09 ns for Cr^{3+} and Cr^{6+} loaded TiO_2 catalysts were observed. The XPS analysis confirmed the presence of Cr^{3+} and Cr^{6+} oxidation states while reduction in particle sizes with increased oxidation state (Cr^{3+}; 16.9 nm and Cr^{6+}; 8.6 nm) was witnessed by HRTEM images. The electrokinetic parameters such as surface charge demand, zeta and streaming potentials were also found to vary as a function of oxidation state of the nanocatalysts. These Cr^{n+}-TiO_2 catalysts were then analyzed for the photooxidation of aspirin and paracetamol drugs with some interesting behaviour. For aspirin, Cr^{6+}-TiO_2 with rate constant, $k = 18.815 \times 10^{-3}$ min^{-1} while in case of paracetamol, Cr^{3+}-TiO_2 catalyst with $k = 8.052 \times 10^{-1}$ h^{-1} showed maximum activity under solar irradiation. The observed photoactivity has been correlated to different chemical nature of substrate molecules, catalyst oxidation state effects and catalyst-substrate associations.

1.1. Introduction and literature survey

1.1.1. Role of metal/metal ions (M/M^{+n}) as co-catalysts

Since many years, metal/metal ions (M/M^{+n}) have been studied and explored a lot for their catalytic, co-catalytic and photocatalytic properties in the fields of synthesis, energy and environment [1-4]. In this concern, oxides of basic metals (Ca^{+2}, Mg^{+2}, Mn^{+2} and Sr^{+2} etc.) have been proven efficient co-catalysts for the synthesis of methanol from CO_2 and H_2 [5]. In another report, Pt and Ru oxides have been incorporated with other transition metal oxides to form ternary systems which improved the oxidation of methanol appreciably [6]. Up to so many years, the role of metal/metal ions was considered as promoters only but recent works have concluded that metals in combination with other semiconductor photocatalysts can become bi-functional catalysts [7-10]. The adsorption of useful species, activation of the catalyst's surface, its sensitivity and structure of the metal/metal ionic species have led to many advancements in the area of catalysis [11,12]. The metals in different oxidized, reduced and ionic forms or in combination with other catalysts exhibit potential applications. For example, the CuO, MnO, NiO and Co_2O_3 loaded rutile TiO_2 nanorods showed enhanced degradation of orange (II) dye due to greater synergetic effect offered by the metal oxide co-catalysts [13]. The Ni, Mn, Fe and Co oxide (MO_x) based TiO_2 photocatalysts exhibited stronger electronic communication and hydrogen-oxygen evolution capabilities as a result of the unique nature of every metal oxide [14].

The metal/metal oxide co-catalysts are generally deposited on the surface of other catalyst materials either by using some surfactants or via photodeposition, sol-gel and wet impregnation methods [15,16]. These methods generate different forms, oxidation states, dispersions, shapes and sizes of the various metal co-catalysts. The catalyst preparation route adopted has been established to influence the photocatalytic performance and other photophysical and optical properties to a great extent [17]. The hydrothermally prepared Ni/ZnO nanoparticles (NPs) have been found to be efficient for the degradation of tartrazine under UV light [18]. The higher activity has been credited to the well and uniform dispersion of Ni particles over the ZnO surface. The Cu, Ag, Au and Pt noble metals are typically photo deposited on the surface of the support photocatalysts [19,20]. These metals due to their strong optical response, electronic behaviour and stability have been investigated a lot.

Therefore, Cu, Ag and Au metals photodeposited over g-C_3N_4 catalyst have been assessed for the degradation of Bisphenol A under natural sunlight [21]. The higher activity of metal deposited binary systems has been correlated to better interfacial properties at M/g-C_3N_4 heterojunction. The photo reduced Cu nanoparticles over TiO_2 surface improved the hydrogen production under ultraviolet (UV) and visible irradiation due to their strong surface plasmon resonance (SPR) effect [22]. The reduction approach to prepare Ag NPs over TiO_2 was also explored to form Ag/TiO_2 and Ag@TiO_2 (core-shell) photocatalysts [23]. The enhanced photoreduction of 4-nitrophenol by these composites was found to depend on the contact between two catalytic systems and surface-active centres.

Apart from depositing metals in their reduced or lower oxidation states, there have been studies which reveal the loading/impregnating metals in their ionic or oxidized forms. These metal ions supported photocatalysts have also gained much attention due to the formation of the charged catalysts. The various metal ions; Mn^{+2}, Cr^{+3}, Fe^{+3}, Co^{+2}, Ni^{+2}, Zn^{+2} and La^{+3} with an acidic ionic liquid have been investigated to produce higher glucose yields and cellulose hydrolysis as a result of their significant co-catalytic effect [24,25]. The photocatalytic removal of cationic dye methyl violet has been achieved by Mn^{+2}, Co^{+2} and Ni^{+2} doped ZnS quantum dots [26]. Different metal ions on the surface of a semiconductor act as electron sinks which improves the charge carrier separation time of the photocatalysts. The introduction of divalent ions Co^{+2}, Ni^{+2}, Cu^{+2} and Zn^{+2} in a perovskite structure have induced vacancy defects enabling a greater number of photogenerated electrons and enhanced activities [27]. The non-precious co-catalysts of $CoSe_2$ have also been verified to increase hydrogen production rates up to 37.5 times than in their absence [28]. It has been inferred from the above research works that most of the catalytic and photocatalytic reactions are accelerated in the presence of the M/M^{+n} co-catalysts. The various metals (M), metal ions (M^{+n}) and their oxides serve as efficient co-catalysts by providing new catalytically active sites, charge transfer and adsorption-desorption equilibria.

1.1.2. Importance of variable oxidation states of metal ions (M^{+n})

It has been unveiled that most of the noble and precious metals like Pt, Cu, Ag and Au are photo deposited in reduced or zero oxidation states. However, these metals in their oxidized form also show greater photocatalytic activities due to changes in the work function of cation oxidation states [29]. Ag(I)/TiO_2 catalyst has been found to show much higher photocatalytic oxidation of methyl blue dye than Ag(0)/TiO_2 catalyst due to the formation of active sites on the catalyst's surface [30]. The MgO supported Au(I) catalysts have also been investigated to

have higher CO oxidation rates than Au(0) species [31]. The Au^{+3}-TiO_2 photocatalysts are considered to act as electron and hole trappers as compared to Au^{+1}-TiO_2 catalysts showing better activities for wastewater treatment purposes by X. Z. Li *et al* [32]. Another study suggests the sensitivity of interchanging the type of metal ions in the co-ordination polymers for improving the photocatalysis [33]. Similarly, Fe^{+3} and Ag^{+} ions have also been investigated to exhibit a pronounced effect on the oxidation of sucrose [34]. This is evident now that metals in their oxidized states act as better co-catalysts for many redox processes. The kind of metal ions and their respective concentrations have been considered to have much influence on the catalytic phenomena. Many studies have confirmed that surface area and shape of NPs are less important factors than the metal oxidation states. Accordingly, the higher selectivity yields of H_2O_2 have been obtained from oxidized Pd catalysts [35]. The Pd^{+2} modified TiO_2 catalysts prepared via impregnation method have been proved to have a profound increase in NO oxidation mainly due to availability of new adsorption sites [36]. This work showed that during the photocatalytic process, the oxidation states of Pd metal underwent dynamic electronic change ($Pd^{+2} \rightarrow Pd^{+4}$) which depicts the importance of variable oxidation states. The higher oxidation state Co catalysts provide effective reaction pathways for the oxidation of methanol [37]. Thus, the charged metal ions act as better electron trappers compared to neutral catalysts/co-catalysts due to their higher surface charge density, electron affinity and redox behaviour as shown in scheme 1.1. These catalysts tend to reduce the activation energy barrier of many redox processes also by acting as electrophilic centres [38]. Therefore, it has been concluded that the oxidation states of loaded metal co-catalysts play a significant role in the photocatalytic systems.

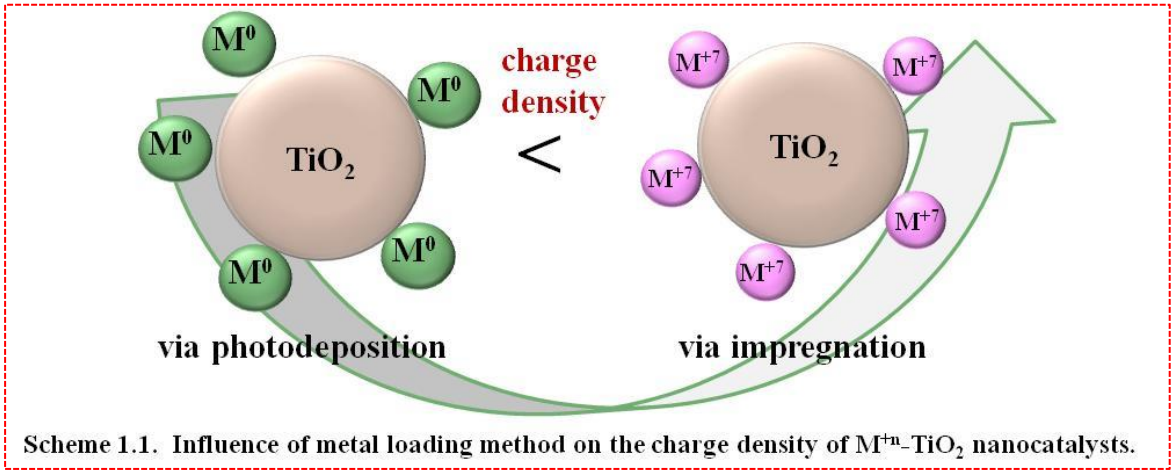

Scheme 1.1. Influence of metal loading method on the charge density of M^{+n}-TiO_2 nanocatalysts.

1.1.3. Effect of metal loading over TiO_2

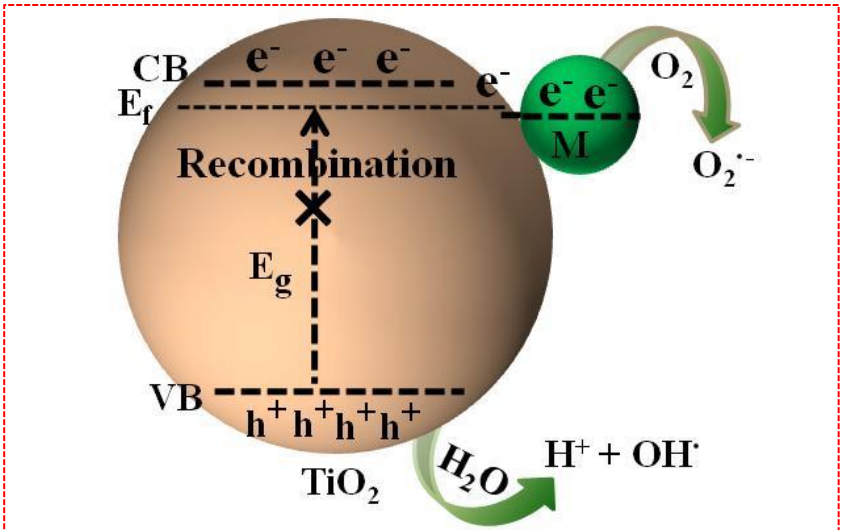

Scheme 1.2. Effect of metal loading over TiO_2 photocatalyst.

Metal-TiO_2 (M-TiO_2) nanocomposites show better and enhanced photocatalytic activities due to reduced recombination rates of generated charge carriers (e^-/h^+ pairs) and extended visible light absorptions (Scheme 1.2). At metal-TiO_2 heterojunction, fermi level equilibration takes place due to work function difference between the metal and TiO_2, enhancing the interfacial charge transfer process [39,40]. In this regard, TiO_2 has been loaded/doped with various kind of metals or non-metals and their oxides [41]. Generally, the photodeposition [42] and co-precipitation [43] methods have been used for the preparation of metal loaded TiO_2 nanoparticles (NPs). In the photodeposition method, metal ionic species having redox potential more positive than the conduction band (CB) potential of TiO_2 act as electron scavengers and are reduced to lower or zero oxidation states in an inert atmosphere of argon and get adsorbed on the surface of TiO_2 [44]. Coinage metals viz. Cu, Ag and Au have been photo deposited on the surface of TiO_2 in elemental (zero oxidation) states due to their suitable redox potentials (Cu = 0.337 eV, Ag = 0.799 eV, Au = 1 eV). These elements (Cu, Ag and Au) due to their strong surface plasmonic effects exhibit higher photocatalytic activities and have been utilised for various photocatalytic applications [45]. Different metals such as Fe, Co, Ni, Pd and Pt etc. have also been loaded on the surface of TiO_2 using various methods. The Pt, Ag, Rh and Pd modified TiO_2 nanoparticles have been investigated to have higher photocatalytic degradation rates for 4-nitrophenol and glucose than unmodified TiO_2 [46]. The plasmonic coinage metals due to their dual role in surface sensitizations and visible light absorptions have been used in a wide range of applications.

Although Cu, Ag and Au have many advantages but due to high cost and some other disadvantageous properties, these metals are not of commercial and frequent use. There are other metals such as Fe, Mn, Cr, Ce [47], Sn [48] and Al [49] etc. (underpotential metals) which cannot be photo deposited on TiO_2 due to their more negative reduction potentials and have been impregnated in their ionic forms showing appreciable photo activities. These metals are cheap, cost-effective and exhibit variable oxidation states. These oxidation states of various metals can be useful for various photocatalytic redox processes. The impregnation of a specific metal on the surface of TiO_2 in different oxidation states can lead to changes in surface charge, zeta potential and point of zero charge (PZC) which in turn will lead to changes in the surface properties and electronic energies. As a result, the amount/degree of adsorption changes which is accountable for different photocatalytic activities. Thus, the surface charge of M^{+n}-TiO_2 nanocatalysts can be controlled by loading a particular metal in variable oxidation states. For example, if Fe(III) and Fe(0) are loaded on the surface of TiO_2, there will be more oppositely charged ionic interactions in case of Fe(III) as compared to Fe(0) state. Thus, if the surface charge of the prepared catalyst can be controlled, adsorption and photocatalytic activities can be tuned accordingly. Based on the literature survey, here is the data chart representing some important and useful research findings:

Table 1: Role of different type of metal/metal ion co-catalysts for various photocatalytic processes.

Sr. No.	Photocatalysts	Method of preparation	Activity	Result findings
1.	Ni, Mn, Fe and Co oxides as co-catalysts for TiO_2	Wet impregnation	Water splitting	For hydrogen evolution = NiO_x-TiO_2 only Oxygen evolution = FeO_x-TiO_2 > CoO_x-TiO_2 > NiO_x-TiO_2 [14].
2.	Ag, Au and Pd as co-catalysts	Photodeposited under sunlight	Bisphenol A degradation	Particle size and Schottky barrier are more important than the light-harvesting capability of catalysts [21].
3.	Mn^{+2}, Co^{+2} and Ni^{+2} doped ZnS catalysts	Wet chemical precipitation method	Methyl violet removal	Mn^{+2} doping provided maximum degradation efficiency [26].

4.	Cr^{+3}, Co^{+2}, Ni^{+2}, Cu^{+2} and Zn^{+2} as co-catalysts	Sol-gel auto combustion method	Safranine-O and remazol brilliant yellow dye degradation	Maximum activity by Zn^{+2} occurs due to oxygen vacancies and reduced bandgap [27].
5.	Ag-TiO_2 catalyst	Photoreduction-thermal method	Methyl blue degradation	Higher oxidation state catalyst provides more active sites than the lower oxidation state catalyst [30].
6.	Fe^{3+} and Ag^{+} modified TiO_2	Impregnation method	Sucrose oxidation	Different metal ions govern different reaction mechanisms [34].
7.	Pd^{+2}-TiO_2 catalyst	Wet impregnation	NO oxidation	Pd^{2+} provide better adsorption sites to the catalyst [36].
8.	Fe, Co, Ce, Cr, Mn, Mg, Ni and Ag ions doped TiO_2 catalysts	Ultrasonic method	Rhodamine B degradation	Dye sensitization by metal ions plays an important role [47].

Literature suggests that if a particular (same) metal is incorporated in different oxidation states, it will lead to different d-electronic states of the same metal, different work functions, lewis acidities, different sizes and charge densities leading to different affinities for organic and inorganic molecules. For example, if Mn^{+2} (0.081 nm) and Mn^{+7} (0.060 nm) having different ionic radii are deposited over TiO_2, there will be higher charge density per unit volume in Mn^{+7} co-catalysts compared to Mn^{+2}. As a result, greater attractions of oppositely charged species will be achieved in Mn^{+7} catalysts. All the above-mentioned factors will lead to greater inter-ionic attractions between the photocatalysts and the substrate molecules enhancing the photodegradation efficiencies. In this manner, photocatalysts having high adsorption capabilities can be utilized for the separation and degradation of different kind of pollutants such as pharmaceuticals, disinfectants, pesticides, herbicides and wastewater dye molecules that possess different ionic structural characteristics.

Therefore, based on various literature studies, we realized the following research gaps which have been fulfilled in the present research work:

1.2. Research Gaps

1. There are reports available on the impregnation/grafting of different metals in single ionic forms on the surface of TiO_2 nanocatalysts i.e. Ce^{+4}, Sn^{+4}, Mn^{+2}, Cr^{+3}, Al^{+3}, Re^{+5}, Os^{+3} and Ru^{+3} etc [50-52]. However, there are no reports found on grafting a particular metal in its different oxidation states (e.g. Mn^{+2} and Mn^{+7}) comparing the effects of variable oxidation states of the same metal on photocatalytic behaviours of M^{+n}-TiO_2 nanocatalysts. For example, Cr metal having various oxidation states (I-VI) has been used in single ionic form (Cr^{+3}) to evaluate its photocatalytic activities but on the other hand, its various oxidation states can be utilized for manipulating different surface structural properties of nanocatalysts, adsorptions and effective photocatalytic degradation processes.

If a particular metal will be deposited in its different oxidation states, there will be different metal ionic radii depending on the oxidation states (Scheme 1.3). This ionic radii of the metallic species will affect the surface and other electrokinetic properties of M^{+n}-TiO_2 nanocatalysts differently. Also, the metal incorporation will be impregnated or doped depending on the sizes of different metal ions.

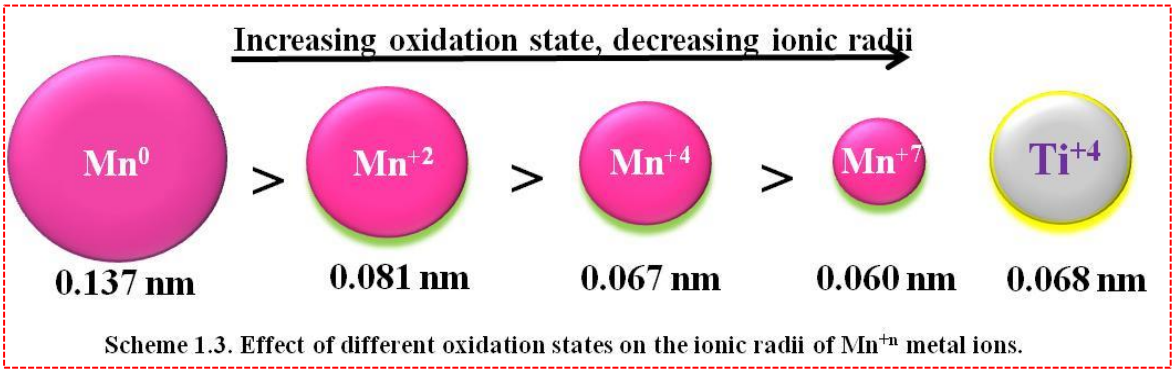

Scheme 1.3. Effect of different oxidation states on the ionic radii of Mn^{+n} metal ions.

2. There are also reports on the study of electrokinetic parameters (surface charge, zeta potential and isoelectric points (IEP/PZC) of titania nanoparticles of different shapes and morphologies, but no reports are present on tuning these surface electrokinetic parameters by different oxidation states of same metal ion doping.

We believe that as the oxidation state of the deposited metal will increase, charge density per unit area will increase leading to greater catalyst-substrate associations with the otherwise non-separable and non-reactive substrate molecules.

Based on the above-mentioned research gaps, my research focuses on the synthesis of metal impregnated TiO_2 NPs of the same metal in different oxidation states. Further, the effect of variable oxidation states of a particular metal on various electrokinetic parameters of catalysts, adsorption isotherms and degradation kinetics for the photocatalytic degradations of the organic and inorganic water pollutants produced by pharmaceutical, agricultural, textile and dyeing industries.

1.3. Objectives

1. To study the effect of different oxidation states (n = 0 to VII) of some metals (Mn^{+n}, Cr^{+n} etc.) on the surface structural properties of M^{+n}-TiO_2 catalysts.

2. To measure the comparative electrokinetic properties (surface charge, zeta potential and point of zero charge (PZC/IEP) of M^{+n}-TiO_2 catalysts.

3. To evaluate the adsorption isotherms and photocatalytic properties for degradation of some toxic pollutants by M^{+n}-TiO_2 catalysts.

1.4. Methodology

1.4.1. Synthesis of M^{+n}-TiO_2 nanocatalysts

Wet impregnation method: Metal ion-TiO_2 (M^{+n}-TiO_2) nanocomposites were prepared by using different salts of a specific metal having different oxidation states via wet impregnation technique [53]. The commercially available form of TiO_2 (Degussa P25) was used as support and further processed to impregnate different metal ionic species. This process consisted of dispersing the TiO_2 NPs in distilled water (DI) followed by the introduction of required amount of respective metal salt solutions (0.01 M) under continuous stirrings for 48 h (Scheme 1.4). Afterwards, the above solutions were repeatedly washed with ethanol and DI water to remove the effect of any unwanted anions or counter ions and then dried in an oven at 80 °C.

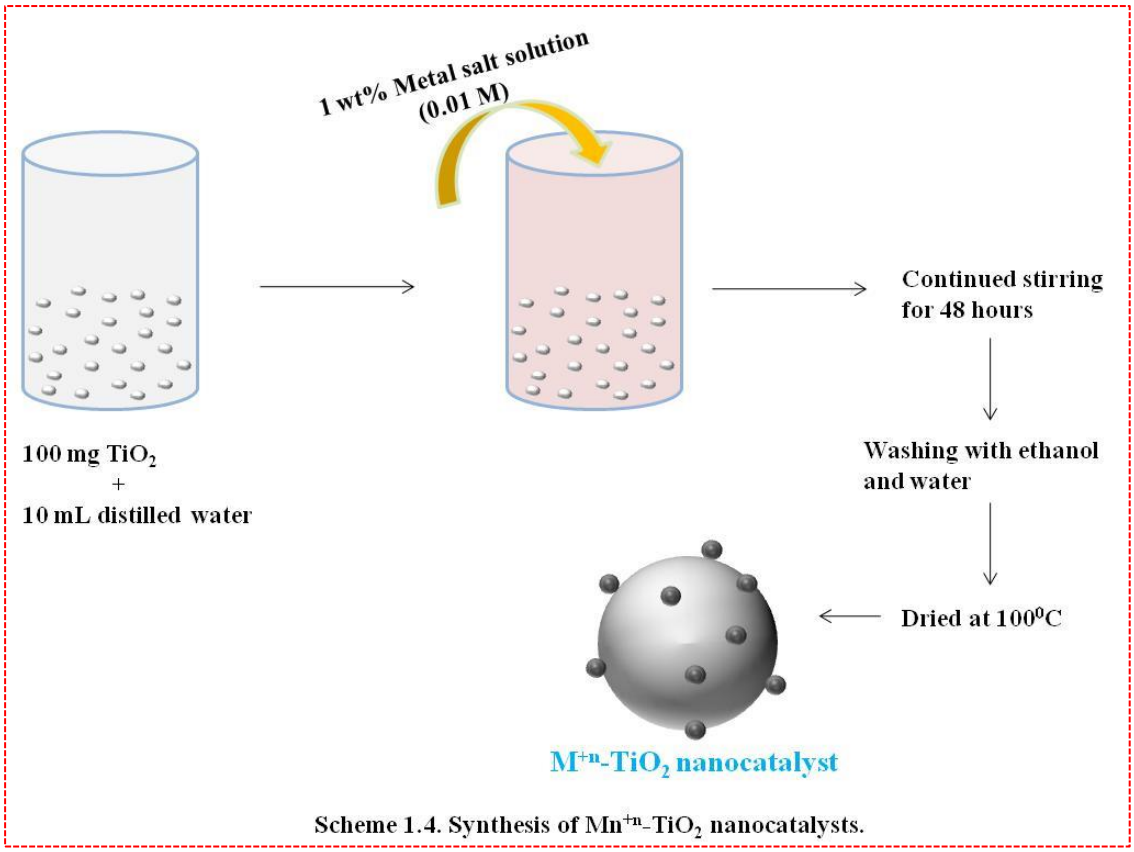

Scheme 1.4. Synthesis of Mn^{+n}-TiO_2 nanocatalysts.

1.5. Characterization techniques

The prepared nanocatalysts were characterized to study their optical, electrokinetic and morphological characteristics. For this, the techniques used are described below:

1.5.1. Diffuse Reflectance Spectroscopy (DRS)

This technique was used to determine the absorbed or reflected amount of light energy by the M^{+n}-TiO_2 nanocatalysts. For this, initially, the dark spectrum was recorded in the absence of light and then the light spectra of $BaSO_4$ was taken as a reference. Then, the spectra of various catalysts were measured by taking a small amount of catalyst (2-5 mg) on a glass plate and putting the light source probe over it. The whole analysis was done using the diffuse reflectance spectrophotometer (DRS, Avantes).

1.5.2. Photoluminescence (PL) measurements

PL analysis was done to determine the fate of charge carriers and recombination rate of prepared catalysts so that impact on the catalytic efficiency could be found out. The instrument used was spectrofluorimeter Perkin Elmer LS 55. The minimum amount of

catalysts was dispersed in DI water and followed by sonication until a uniform solution was formed. This solution was then photoexcited between wavelength range of 200-350 nm with a slit width of 3.5:3.5 having an emission range of ~ 380-600 nm.

1.5.3. Time resolved Spectroscopy

The time resolved spectra were recorded to know the lifetime of charge carrier i.e. an electron in its excited states. It was recorded using a fluorescence spectrophotometer (Edinburgh instruments; LifeSpec-II model, U.K.). The catalysts were converted into a thick mass with the help of ethanol solvent and then were processed for laser pulsation to know the fate of relaxation times. For the purpose, samples were exposed to an excitation wavelength of 340 nm and spectra were fitted using the bi-exponential decay function to obtain the intensity weighted average lifetimes. The average lifetimes (τ_{av}) and results obtained for different nanocatalysts were calculated using the following equation:

$$\tau_{av} = \frac{\Sigma a_i \times \tau_i^2}{\Sigma a_i \times \tau_i}$$

where, τ_1 and τ_2 are the fast and slow decay components, respectively while a_1 and a_2 are their respective emission amplitudes.

1.5.4. Dynamic Light Scattering (DLS)

This technique as the name suggests detects the light scattered by the NPs dissolved in a particular medium. When laser light falls on the surface of the catalyst, it is scattered at certain angles depending upon the hydrodynamic size of the NPs. This scattered light is analyzed by a detector and measures the nanoparticle size. For this, the samples (1 mg) were well dispersed in (5 mL) DI water, filtered by 0.2 μm filter and studied using ZEN 3600, Malvern, U.K. instrument.

1.5.5. Zeta potential measurements

When nanoparticles of a catalyst are dispersed in a dispersion medium, there exists some potential difference between the dispersion phase and the stationary layer of liquid attached known as zeta (ζ) potential. This potential difference develops a new charge on the catalyst's surface that also determines its stability and so is needed to be measured. This was analyzed by ZEN 3600, Malvern, U.K. instrument by putting the dispersed solution of catalysts in a cuvette consisting of palladium electrode at 25 °C.

1.5.6. Streaming potential and Surface charge demand analysis

The fluid flow pressure accelerates the transport of counter ions which gives rise to a net charge transport which is measured in terms of streaming potential. Based on this charge transport effect, the surface demand of various nanocatalysts for the oppositely charged species is measured. Both of these measurements were done using a particle charge detector (PCD, Mutek). For the measurements, samples (30-50 mg) were dispersed in a suitable solvent carrying the opposite charge as that expected on the surface of the catalyst was used and allowed to stream through the sample. Based on obtained streaming potential, further the charge demand in μeq/g by the catalyst was also recorded.

1.5.7. Scanning Electron Microscopy and Energy Dispersive Spectroscopy (SEM-EDS)

The SEM-EDS analysis was done to know the surface and elemental characteristics of the catalysts. This technique utilises the high beam of electrons that falls on the surface of substance and ejects electrons (secondary electrons) from it which are then analyzed by a detector. The secondary electrons tell the surface/topographic image of the sample while reflected/backscattered electrons depict the surface structure and elemental composition. The analysis was done using SEM-EDS, JEOL JSM-7600 F, 01 operating at 30 kV instrument.

1.5.8. Transmission Electron Microscopy (TEM)

This technique consists of interactions where a beam of electrons is transmitted through the sample of not more than 100 nm thickness placed over a grid. Due to this interaction, an image is formed which is then magnified and focused onto an imaging device. These morphological images obtained are of higher resolutions with the exact shape, boundary, interface, crystallography and atomic structure of the material. This study was carried out by high-resolution transmission electron microscope; HRTEM, FEI Tecnai G2 F20, the Netherlands operating at 200 kV. For this, the sample was dispersed in aqueous media and put on a copper grid coated with a film of carbon.

1.5.9. X-ray Photoelectron Spectroscopy (XPS)

The XPS is a phenomenon which tells us about the oxidation or valence state of elements, their chemical environment and bonding state qualitatively and quantitatively. A focussed beam of X-rays is made to fall on the surface of a material which ejects electrons from a depth of 0 to 10 nm under vacuum conditions. The ejected electrons are then collected by a collector lens which then measures the kinetic energy and number of electrons and further signal is amplified on a screen by a detector. The sample is used in its natural form or sometimes is scraped, etched to remove any kind of contamination or to expose deeper layers. This whole analysis was determined by X-ray photoelectron spectroscope; XPS, KRATOS axis 165 Shimadzu, UK having Mg Kα radiation (1252.6 eV at 75 W).

1.5.10. X-ray Diffractometry (XRD) and Raman Spectroscopy

The XRD analysis makes use of X-rays that are produced by striking a beam of electrons on a target metal (Mo, Cu, Co, Fe or Cr) having a wavelength corresponding to the crystal plane spacing of the catalyst material. These radiations penetrate the bulk of sample and the diffracted beam is then analyzed by a detector. The sample is prepared in the form of a palette which is prepared under high pressure. All these measurements were done using XRD, analytical Xpert pro with Cu-Kα (1.54 A°) operating at 45 kV having diffraction angle 2θ (20-80 °). Further, the small angle x-ray scattering (SAXS) experiments were also performed using X-ray generator-ID3003 - Cu Kα (α = 0.1542 nm) having power 40 kV/50 mA and beam collimation line = 0.3 × 20 mm^2. The detector used was 1D CMOS (Mythen 1K) with an exposure time of 15 minutes × 1 frame at a temperature of 22 ^{0}C. Various structural, stability, crystallographic and electron density profile parameters were detected using this analysis. To further carry out the crystal studies, the Raman spectroscopy was performed on the prepared catalysts. The spectra were recorded within 100-700 cm^{-1} range with 1404 double monochromator having 2400 grooves/mm gratings. The liquid nitrogen-cooled CCD detector was employed to record the spectra with an Ar^+ line of 514.5 nm for sample excitation.

1.5.11. Temperature Programmed Desorption (TPD)

This analysis was performed to determine the acidic behaviour and adsorption-desorption phenomena on the catalyst's surface. The measurements were done using MicrotracBEL Corp. BELCAT II instrument. For this purpose, 0.05 g of the photocatalyst was flushed with

He gas at 300 ^{0}C to remove the moisture content or any other adsorbed gases. Then, NH_3 gas was allowed to adsorb at 100 ^{0}C for 0.5 h followed by purging with He gas again to remove the unadsorbed gas molecules. Afterwards, the NH_3 gas was made to desorb in the temperature range 100 - 500 ^{0}C under He flow and was detected via a thermal conductivity detector.

1.6. Adsorption and photocatalytic activity

The photocatalytic activity of different M^{+n}-TiO_2 nanocatalysts was carried out in different test tubes. The appropriate substrate concentration was maintained which could follow the Lambert-Beer's law. Then, 5 mL of this solution was put in the test tube containing a magnetic bead and treated with a required minimum amount of the catalyst (20 mg). The mouth of each test tube was covered with a foil after creating some small holes in it to maintain an oxygenated atmosphere. These reaction samples were then kept with continuous stirrings in the absence of light to bring adsorption-desorption equilibria. The total amount of substrate/adsorbate adsorbed on the catalyst's surface was calculated using the equation:

$$q_e = \frac{(C_0 - C_e)V}{W}$$

where C_0 and C_e are the initial and equilibrium substrate concentrations (µg/mL), V is the total volume of solution (mL) and W is the mass (mg) of nanocatalysts used.

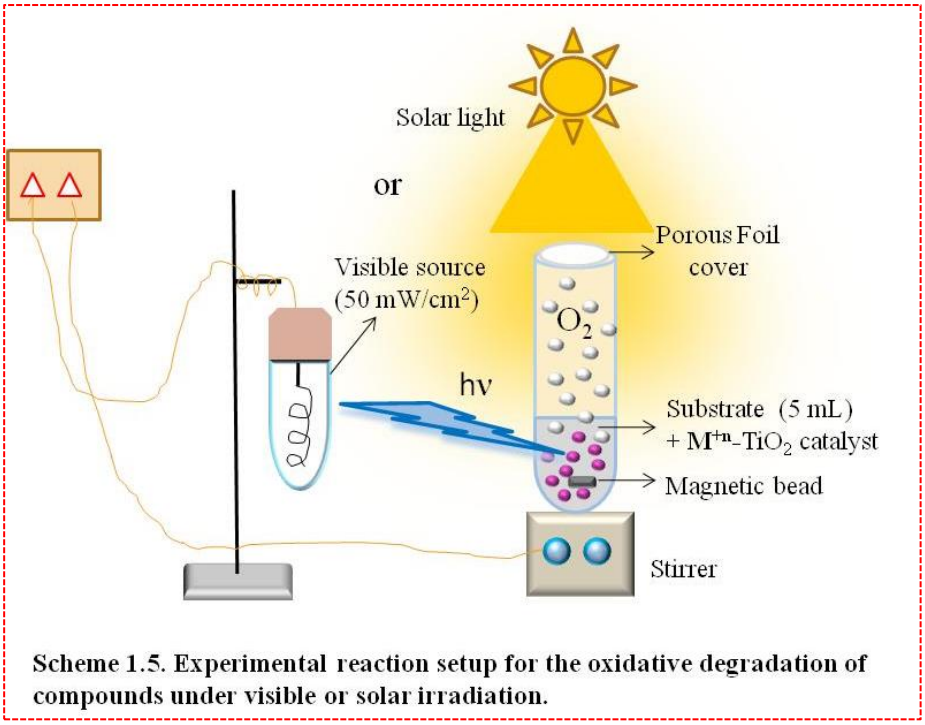

Scheme 1.5. Experimental reaction setup for the oxidative degradation of compounds under visible or solar irradiation.

After the adsorption measurements were done, the reaction mixtures were placed under solar or visible irradiation (50 mW/cm^2) as shown in scheme 1.5 until the complete oxidation or degradation of the compound took place. The samples were then separated by centrifugation and analyzed at regular time intervals using UV-visible spectrophotometer (Shimadzu). Further, the reaction kinetics were studied using decreased concentrations of substrates at different time periods during the photooxidation process.

Following are the compounds which were photo degraded using the prepared M^{+n}-TiO_2 nanocatalysts:

Table 2: Various compounds used to study the photooxidation behaviour of the catalysts

Sr.No.	Name of compound	Structure
1.	Methylene blue dye	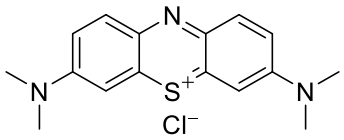
2.	Methyl viologen (Gramoxone)	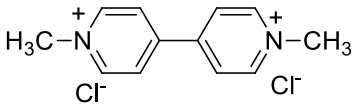
3.	Aspirin	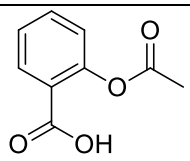
4.	Paracetamol	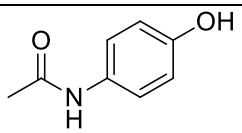
5.	Basic Fuchsin dye	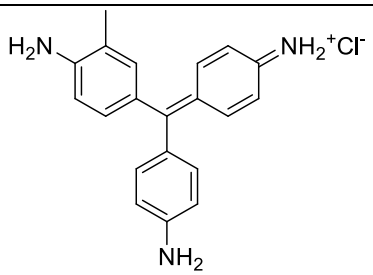

6.	Salicylic acid	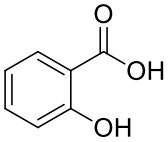
7.	Salicylaldehyde	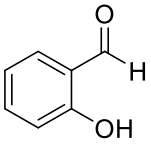

References

[1] S. Bai, X. Wang, C. Hu, M. Xie, J. Jiang, Y. Xiong, Chem. commun. 50(46) (2014) 6094-6097.

[2] P. Christopher, H. Xin, S. Linic, Nat. Chem. 3(6) (2011) 467.

[3] Y. Sakata, Y. Matsuda, T. Yanagida, K. Hirata, H. Imamura, K. Teramura, Catal. Lett. 125 (2008) 22-26.

[4] A.S. Amarasekara, B. Wiredu, Catal. Commun. 81 (2016) 41-44.

[5] A. Gotti, R. Prins, J. Catal. 175 (1998) 302-311.

[6] K. Lasch, L. Jorissen, J. Garche, J. Power Sources 84 (1999) 225-230.

[7] S.K. Dutta, S.K. Mehetor, N. Pradhan, J. Phys. Chem. Lett. 6 (2015) 936-944.

[8] S. Gao, X. Jia, Z. Li, Y. Chen, J. Nanopart. Res. 14(3) (2012) 748.

[9] J.Y. Park, S.M. Kim, H. Lee, B. Naik, Catal. Lett. 144(12) (2014) 1996-2004.

[10] S. I. Mogal, M. Mishra, V.G. Gandhi, R.J. Tayade, Mater. Sci. Forum 734 (2013) 364-378.

[11] B.R. Cuenya, Thin Solid Films 518 (2010) 3127-3150.

[12] K. Chang, X. Hai, J. Ye, Adv. Energy Mater. 6(10) (2016) 1502555.

[13] L.K. Dhandole, M.A. Mahadik, S.G. Kim, H.S. Chung, Y.S. Seo, M. Cho, J. Ryu, J.S. Jang, Appl. Mater. Interfaces 9(28) (2017) 23602-23613.

[14] J.S. Schubert, J. Popovic, G.M. Haselmann, S.P. Nandan, J. Wang, A. Giesriegl, A.S. Cherevan, D. Eder, J. Mater. Chem. A 7 (2019) 18568-18579.

[15] M. Khairy, W. Zakaria, Egypt. J. Pet. 23 (2014) 419-426.

[16] M.A. Behnajady, N. Modirshahla, M. Shokri, B. Rad, Glob. Nest J. 10(1) (2008) 1-7.

[17] S.C. Lee, H.O. Lintang, L. Yuliati, Beilstein J. Nanotechnol. 8 (2017) 915-926.

[18] S.S. Turkyilmaz, N. Guy, M. Ozacar, J. Photochem. Photobiol. A 341 (2017) 39-50.

[19] P. Gomathisankar, K. Hachisuka, H. Katsumata, T. Suzuki, K. Funasaka, S. Kaneco, Int. J. Hydrog. Energy 38 (2013) 11840-11846.

[20] Y.F. Yang, P. Sangeetha, Y.W. Chen, Int. J. Hydrog. Energy 34 (2009) 8912-8920.

[21] C.H. Hak, L.C. Sim, K.H. Leong, P.F. Lim, Y.H. Chin, P. Saravanan, Environ. Sci. Pollut. Res. 25 (2018) 25401-25412.

[22] L. Clarizia, G. Vitiello, G. Luciani, I.D. Somma, R. Andreozzi, R. Marotta, Appl. Catal. A 518 (2016) 142-149.

[23] J. Ma, X. Guo, Y. Zhang, H. Ge, Chem. Eng. J. 258 (2014) 247-253.

[24] B. Wiredu, A.S. Amarasekara, Catal. Commun. 70 (2015) 82-85.

[25] B. Wiredu, A.S. Amarasekara, Bioresour Technol. 189 (2015) 405-408.

[26] H.R. Rajabi, M. Farsi, J. Mol. Catal. A Chem. 399 (2015) 53-61.

[27] M. Dhiman, M. Tripathi, S. Singhal, Mater. Chem. Phys. 202 (2017) 40-49.

[28] E.H. Kim, D.A. Reddy, H. Lee, S. Jeong, D.P. Kumar, J.K. Song, M. Lim, T.K. Kim, Catal. Sci. Technol. 9(17) (2019) 4702-4710.

[29] M.T. Greiner, L. Chai, M.G. Helander, W.M. Tang, Z.H. Lu, Adv. Funct. Mater. 22(21) (2012) 4557-4568.

[30] H. Zhang, G. Wang, D. Chen, X. Lv, J. Li, Chem. Mater. 20(20) (2008) 6543-6549.

[31] J. Guzman, B.C. Gates, J. Am. Chem. Soc. 126(9) (2004) 2672-2673.

[32] X. Li, F. Li, Environ. Sci. Technol. 35(11) (2001) 2381-2387.

[33] Z. Shao, C. Huang, X. Han, H. Wang, A. Li, Y. Han, K. Li, H. Hou, Y. Fan, Dalton Trans. 44(28) (2015) 12832-12838.

[34] V. Vamathevan, H. Tse, R. Amal, G. Low, S. Mcevoy, Catal. Today 68 (2001) 201-208.

[35] V.R. Choudhary, C. Samanta, T.V. Choudhary, Appl. Catal. A 308 (2006) 128-133.

[36] Z. Wu, Z. Sheng, H. Wang, Y. Liu, Chemosphere 77 (2009) 264-268.

[37] S. Zafeiratos, T. Dintzer, D. Teschner, R. Blume, M. Havecker, A. Knop-Gericke, R. Schlogl, J. Catal. 269 (2010) 309-317.

[38] K. Muniz, C.H. Hovelmann, J. Streuff, J. Am. Chem. Soc. 130 (2008) 763-773.

[39] S.G. Kumar, L.G. Devi, J. Phys. Chem. A 115 (2011) 13211-13241.

[40] Z. Zhang, J.T. Yates Jr, Chem. Rev. 112(10) (2012) 5520-5551.

[41] A. Zaleska, Recent Pat. Eng. 2(3) (2008) 157-164.

[42] S.C. Chan, M.A. Barteau, Langmuir 21(12) (2005) 5588-5595.

[43] L. Wang, T. Egerton, J. Mater. Sci. Res. 1(4) (2012) 19.

[44] M.I. Litter, Appl. Catal. B 23(2) (1999) 89-114.

[45] A. Roguska, A. Kudelski, M. Pisarek, M. Opara, M. Janik-Czachor, Appl. Surf. Sci. 257(19) (2011) 8182-8189.

[46] M. Bellardita, H.A. El Nazer, V. Loddo, F. Parrino, A.M. Venezia, L. Palmisano, Catal. Today 284 (2017) 92-99.

[47] H. Feng, E.Y. Liya, M.H. Zhang, Mater. Res. Bull. 48(2) (2013) 672-681.

[48] Z. Xiufeng, L. Juan, L. Lianghai, W. Zuoshan, J. Nanomater. 2011 (2011) 47.

[49] D. Ariyanti, J. Dong, J. Dong, W. Gao, Bull. Chem. React. Eng. Catal. 11(1) (2016) 40-46.

[50] A.S. Ganeshraja, K. Zhu, K. Nomura, J. Wang, Appl. Surf. Sci. 441 (2018) 678-687.

[51] H. Zhu, J. Tao, X. Dong, J. Phys. Chem. C 114 (2010) 2873-2879.

[52] R. Li, Y. Zhao, R. Hou, X. Ren, S. Yuan, Y. Lou, Z. Wang, D. Li, L. Shi, J. Photochem. Photobiol. A 319-320 (2016) 62-69.

[53] B. Pal, R. Kaur, I.S. Grover, J. Ind. Eng. Chem. 33 (2016) 178-184.

Chapter 2

SECTION - 2A

To study the effect of variable oxidation states of Mn(II/VII)-TiO_2 photocatalysts on electrokinetic, surface structural and photocatalytic properties

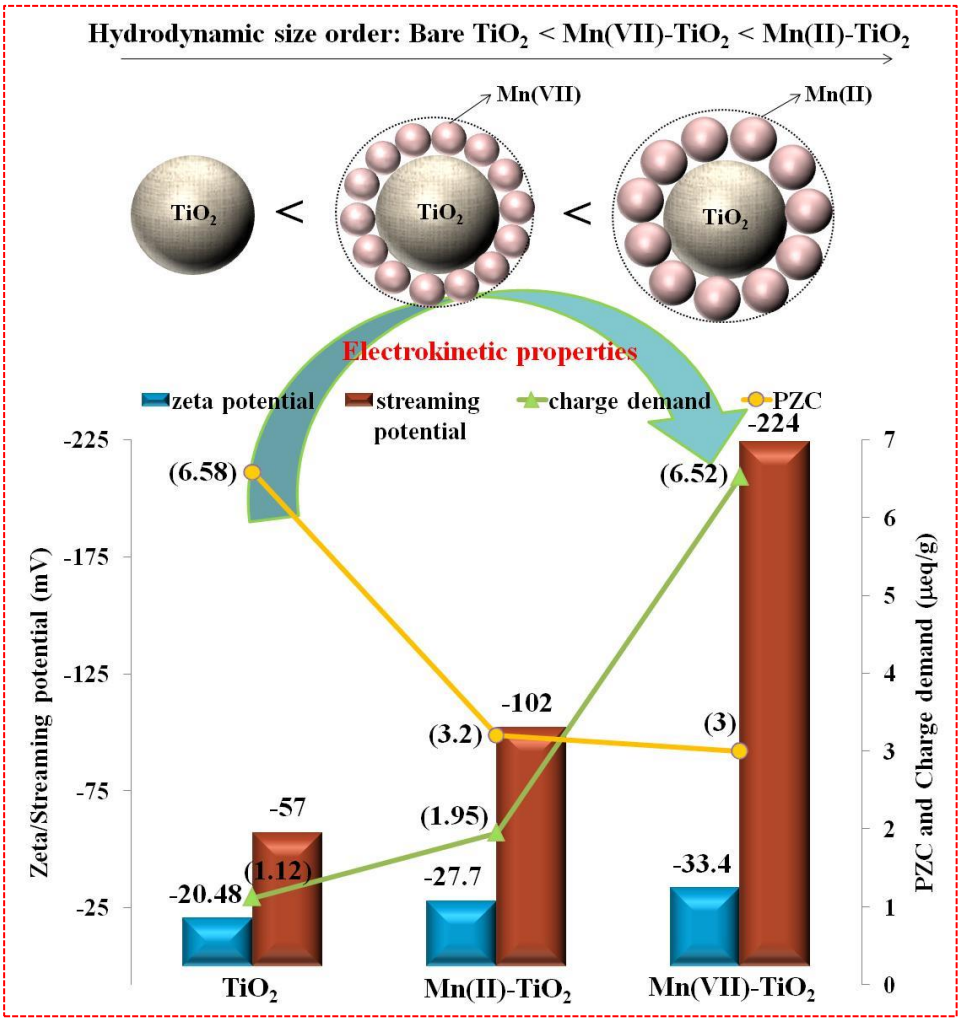

Summary:

This chapter summarizes the Mn(II)/Mn(VII) imparted influence on the co-catalytic activity of Mn^{+n}-TiO_2 catalysts. The absorption edge of Mn^{+n}-TiO_2 nanocatalysts revealed red shifts (515 nm to 550 nm) with increased oxidation state (II to VII) of Mn^{+n} due to $^6A_{1g} \rightarrow {}^4T_{1g}$ transitions. The optical, electrokinetic and structural properties varied a function of Mn^{+n} impregnations. These catalysts further revealed efficient photocatalytic degradations of cationic/anionic substrates depending on their different electrokinetic parameters.

SECTION - 2B

Effective photooxidative degradation of methyl viologen using Mn^{2+}/Mn^{7+}-TiO_2 nanocomposites under solar irradiation

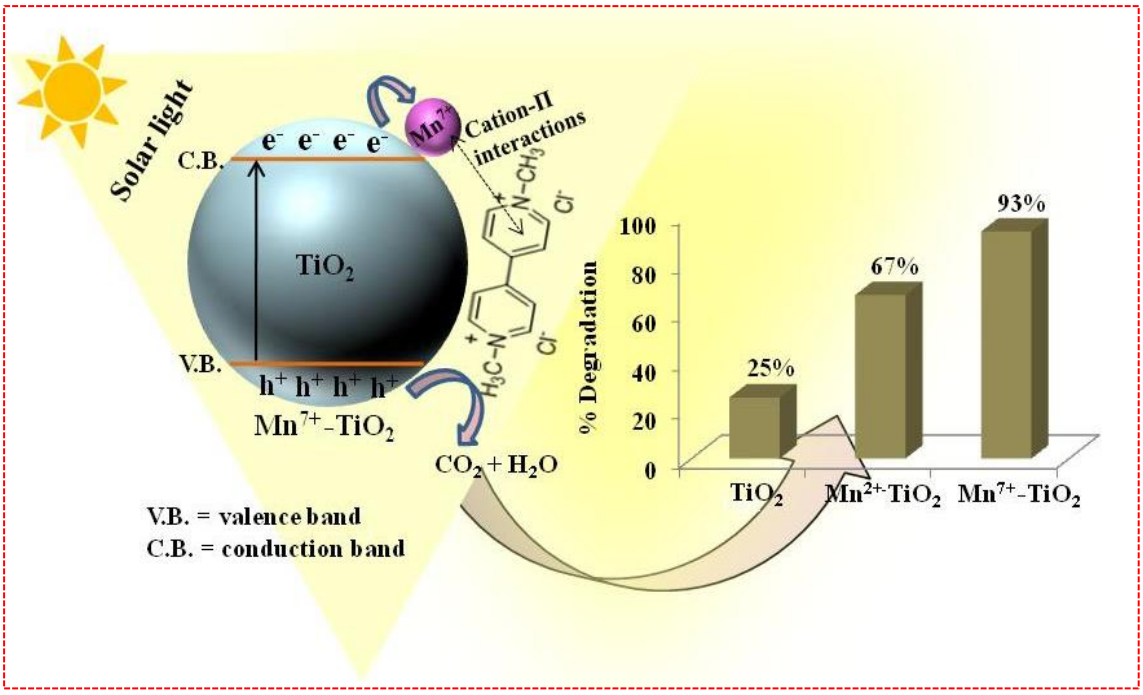

Summary:

This section is an extension of the previous section explaining the Mn^{7+} co-catalyst imparted enhanced co-catalytic oxidative efficiency to Mn^{n+}-TiO_2 nanocomposites for the degradation of toxic herbicide methyl viologen under solar irradiation. The optical spectra of these catalysts showed bathochromic shifts (from 355 to 572 nm) due to the presence of Mn^{2+} and Mn^{7+} ions. The adsorption-desorption studies using NH_3 gas revealed that Mn^{7+} ions generate enhanced Lewis acidity on the co-catalyst's surface compared to Mn^{2+} impregnations. The cation-Π interactions between the catalyst and substrate molecules have been witnessed to impart greater associations and so thus the photooxidative degradation process. The Mn^{2+} and Mn^{7+} impregnations displayed 2.6 and 3.7 times higher photoactivity than bare TiO_2 which has been correlated to different oxidation states and surface structural properties imparted by Mn^{n+} ions.

2.1. Introduction

Noble Metal-TiO_2 nanocomposites offer a great deal of research interest due to their improved band energetics, optoelectronic and photocatalytic properties for solar energy conversions [1-6]. It has been find out that metal-TiO_2 interfacial properties are strongly dependent on nature of metal, distribution of metal nanodeposits and preparation techniques e.g. photodeposition, doping and wet impregnation method etc [7]. Most of the preparation methods are associated with the reduction of metal ions into zero or lower valence state. However, in wet impregnation method, metals in their respective ionic state are loaded over support surface. These metal ions exhibit weak ionic or vander wall interactions with the semiconductor materials. This property of impregnation method can be better exploited to associate and photochemically process the charged/ionic substrate molecules which are otherwise difficult to remove. Under different preparation conditions, islands of metal/metal ion nanodeposits (1-100 nm) are either positioned on the TiO_2 surface or occupy the interstitial/substitutional sites. These metal deposits (0.1-2 wt%) act as co-catalysts by preventing the recombination rate of photogenerated charge carriers formed during the band gap excitation of TiO_2 by ultra voilet light [8]. Generally, the work function difference between metal and TiO_2 lead to establishment of a helmholtz double layer at metal-TiO_2 interface due to fermi level equilibration with simultaneous formation of schottky barrier [9]. When the depletion/accumulation layer is formed due to fermi level equilibration and becomes equal to the photon penetration, maximum separation of electron-hole pair take place leading to highest photocatalytic efficiency.

Literature reveals that Au, Pt and Ag metals photodeposited onto TiO_2 exhibit higher and selective oxidation of benzene via electron depleted Au@TiO_2 catalyst [10-12]. In this method, no permanent bond exists between metal and TiO_2, but an association comprising ohmic/non-ohmic contact occurs. In another work, Fe^{+3} has been found to substitute Ti^{+4} species due to similar size of both ions (Fe^{+3} = 0.064 nm and Ti^{+4} = 0.068 nm) possessing maximum photoactivity for iodide oxidation to iodine [13]. Interstitially modified titania nanostructures by Ag metal show appreciable degradation rates for rhodamine B due to alteration in oxygen vacancies [14]. Fe^{+3} modified TiO_2 has been considered to promote the defect formation in TiO_2 lattice leading to enhanced degradation of brilliant red X-3B [15]. It has also been observed that Au^{+}/Au^{+3} ion in TiO_2 lattice promotes the charge trapping efficiency and enhances the photocatalytic activity [16]. Effective and significant photocatalytic degradation of Eriochrome black T dye has been achieved via Pt^{+4} and Fe^{+3}

incorporated TiO_2 nanocatalysts [17]. Composites of Fe^{+3}, Co^{+2}, Ce^{+3}, Cr^{+3}, Mn^{+2}, Mg^{+2}, Ni^{+2} and Ag^{+} ions with TiO_2 exhibit different ionic radii, crystal structure and surface properties that greatly effect the degradation of environment pollutants [18]. The photooxidation of 2-chlorophenol using Mn-TiO_2 photocatalyst has been found to be dominated due to the electron accepting ability of Mn metal [19,20]. It has been examined that the cation work function [21], ionic radii and position of metal ions onto TiO_2 lattice describe its propensity for an effective photocatalytic process. When ions of different metals (Fe^{+3}, Cr^{+6}, Cu, Ag and Au etc.) are impregnated over TiO_2, there occurs a change in surface charge, co-catalyst size, oxidation state and other optical and photocatalytic properties [22-24]. Various reports show that depending upon the photocatalyst preparation technique, kind of metal ion, its ionic radius, the photocatalytic activity significantly varies.

Although there are reports on the improved photocatalytic performance by different impregnated metal ions/oxidation states, however, the effect of impregnation of a specific or single metal in its variable oxidation states on surface morphological and photophysical properties of TiO_2 are rarely reported. If same/particular metal in different oxidation states is impregnated, then oxidation state, ionic size, work function, electron affinity and net electronic charge on the surface of photocatalyst will also change. In this regard, this research study presents the effect of different oxidation states of Mn(II) and Mn(VII) (ionic radii; 0.081 and 0.060 nm, respectively) on the electrokinetic, surface structural, optoelectronic and adsorption properties. As there exist a significant difference of oxidation states in Mn(II) and Mn(VII), their impregnation may improve light sensivity and impart different kind of interactions with cationic or anionic substrate molecules. In this concern, the photocatalytic oxidation of model environment pollutants: cationic (fuchsin blue and methylene blue) and anionic (salicylic acid and salicylaldehyde) using these Mn^{+n}-TiO_2 nanocomposites has been investigated under visible light irradiation.

2.2. Experimental details

2.2.1. Materials

Manganese sulphate monohydrate ($MnSO_4.H_2O$), Potassium permanganate ($KMnO_4$), Hydrochloric acid (HCl, 35%) and Sodium hydroxide (NaOH, 96%) all were purchased from Lobachemie, India. Fuchsin blue (Pulver) from MERCK DARMSTADT, Germany, Methylene blue from S.D. fine chem limited, Salicylic acid from Lobachemie, India and Salicylaldehyde from spectrochem, India were used. All chemicals were used without any

further purification. Commercially available form of TiO_2 (P25; 70% Anatase + 30% Rutile phase) was received as gift from Degussa corporation, Germany. Distilled water (DI) was obtained from an ultrafiltration system (Milli-Q, Millipore) with measured conductivity of 35 mho cm^{-1} at 25° C.

2.2.2. Synthesis of Mn^{+n}-TiO_2 nanocomposites

The fabrication of Mn^{+n} loaded TiO_2 photocatalysts was achieved using wet impregnation method [25]. In this procedure, 100 mg of TiO_2 was dispersed in 10 mL of distilled (DI) water followed by the introduction of required amount (1 wt %) of metal salt solution (0.01 M; $MnSO_4$ for Mn(II) and $KMnO_4$ for Mn(VII) impregnation, respectively). The resulting solutions were continuously stirred for 48 h and then centrifuged (5000 rpm for 5 min) and washed with water and ethanol five times and dried at 100 °C.

2.2.3. Characterization techniques

The characterizations have been done as per the discussion in chapter 1 (section 1.5).

2.2.4. Adsorption study

Adsorption capability is the most important prerequisite to determine the effective photocatalytic degradation property of any catalyst. In this regard, the Mn(II)/(VII)-TiO_2 nanocatalysts were examined for their adsorption efficiencies with different type of substrate molecules under dark conditions. To compare the relative adsorption behaviour of different Mn^{+n}-TiO_2 co-catalysts, an appropriate amount of prepared catalysts (20 mg) was used for cationic dyes; fuchsin blue and methylene blue (0.02 mM, 5 mL each) and anionic substrates; salicylic acid and salicylaldehyde (0.4 mM, 5 mL each) for 1 h duration in the absence of light. The reaction samples were then centrifuged at 6000 rpm for 5 min and analysed by UV-visible spectrophotometer.

2.2.5. Photocatalytic activity

The photocatalytic activity of different Mn^{+n}-TiO_2 co-catalysts (20 mg) was carried out in a test tube containing 5 mL of the cationic dye molecules; fuchsin blue and methylene blue; (0.02 mM) and anionic molecules; salicylic acid and salicylaldehyde (0.4 mM) at room temperature for different time duration under visible light irradiation (50 mW/cm^2). The catalyst treated reaction samples were put under the photooxygenated conditions with

continuous stirrings and taken at regular time intervals, then separated by centrifugation (at 8000 rpm for 5 min.). The separated samples were examined by UV-visible spectrophotometer (λ_{max} = 546 and 663 nm for fuchsin blue and methylene blue, respectively). While for salicylic acid and salicylaldehyde, the spectra were studied at λ_{max}= 296 and 325 nm, respectively for further kinetic studies.

2.3. Results and discussions

2.3.1. Morphological and Surface structural properties

SEM and elemental mapping analysis revealed the uniform distribution of Mn nanoparticles over TiO_2 surface and more fine dispersion of Mn(VII)-TiO_2 NPs compared to Mn(II)-TiO_2 photocatalyst (Fig. 2.1). A good dispersion arises due to enhanced repulsions among highly charged molecules of Mn(VII)-TiO_2 than Mn(II)-TiO_2 nanocatalyst as reflected via zeta potential and surface charge measurements as discussed later. Further, the elemental detection analysis confirmed the appropriate deposition of Mn(II) (0.94 wt%) and Mn(VII) ions (0.57 wt%) onto TiO_2 surface.

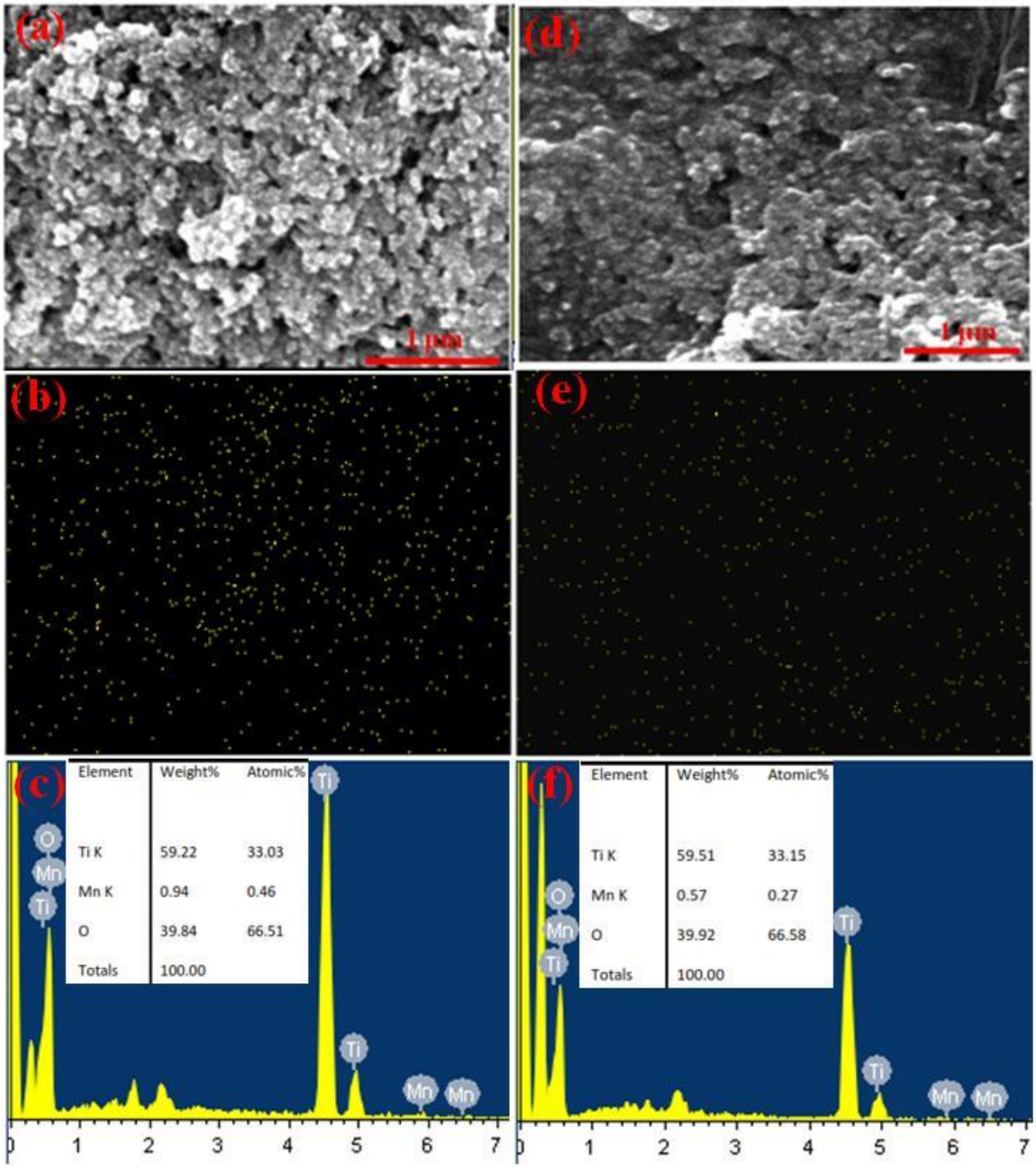

Figure 2.1. The SEM, elemental mapping images and corresponding EDS spectra of Mn(II)-TiO_2 (a, b, c) and Mn(VII)-TiO_2 (d, e, f) co-catalysts.

The XRD pattern of bare and Mn^{+n}-TiO_2 co-catalysts confirmed the presence of both anatase and rutile phase [26,27] showing that Mn loading restricts the phase conversion of rutile into anatase (Fig. 2.2). Enhanced peak intensities with slight peak shifts were observed after Mn^{+n} loading which depicts the interaction of Mn metal ions with the titanium photocatalyst. However, software analysis (Xpert high score) of Mn(II)-TiO_2 showed the presence of few diffraction peaks at 27.3° (310 plane) for MnO_2 (tetragonal crystal system, JCPDS card 053-0633), 29.1° (112) and 67.2° (106) for Mn_2TiO_4 (tetragonal crystal system, JCPDS card 01-073-0521) and 31.8° (120) corresponding to Mn_3O_4 (orthorhombic, JCPDS card 016-0350). Similar diffraction peaks for Mn_2TiO_4 phase in addition to 35.3° (211) related to Mn_3O_4 were observed for Mn(VII)-TiO_2 photocatalyst but are not detected in the XRD spectrum might be due to low content of loaded metal (< 5 %) [28,29].

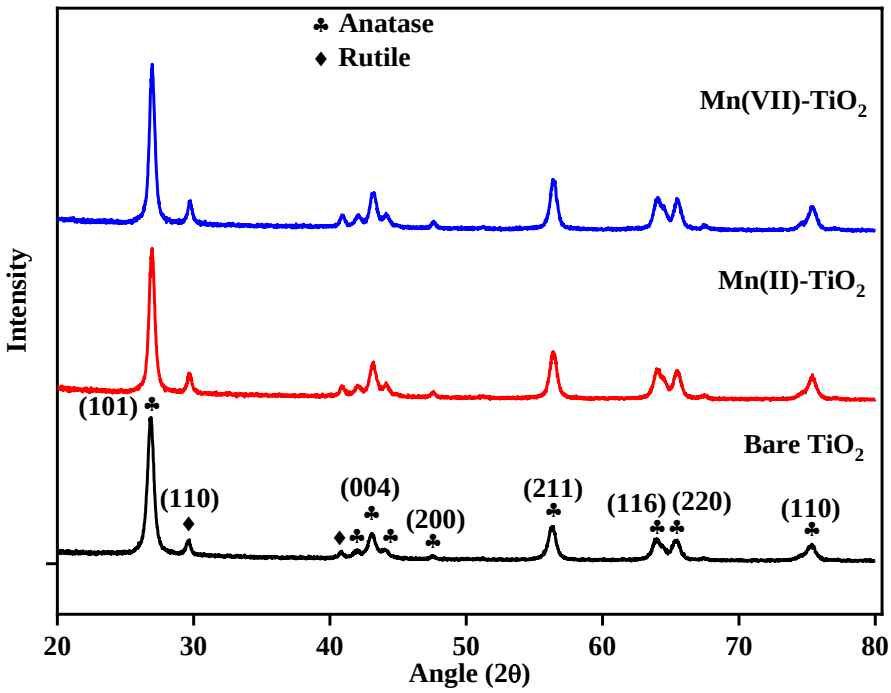

Figure 2.2. Crystallographic analysis of different bare and Mn^{+n}-TiO_2 nanocatalysts.

XRD results were further supported by HRTEM analysis which revealed the presence of lattice planes with interplanar distances 0.30, 0.28 and 0.32 nm corresponding to Mn_2TiO_4, Mn_3O_4 and TiO_2 (rutile phase), respectively in Mn(II)-TiO_2 catalyst (Fig. 2.3). As shown by SAED pattern, interplanar distances of Mn_2TiO_4 and Mn_3O_4 are attributed to 112 and 120 planes and for TiO_2 it is related to 110 plane. In case of Mn(VII)-TiO_2, lattice fringes with

interplanar distances of 0.25 and 0.32 nm were observed (Fig. 2.4). These interplanar distances correspond to Mn_3O_4 and TiO_2 (rutile) with planes 211 and 110, respectively. Structural morphology describes the impregnation of mixed shape (spherical, cubical and rectangular) islands of manganese nanodeposits on TiO_2 surface in Mn(II)-TiO_2 photocatalyst (Fig. 2.3a and 2.3b). In figure 2.3(a-b) and figure 2.4(a-b), location wise clear contrast can be seen between Mn^{+n} and TiO_2 nanoparticles. Further, these NPs have been distinguished on the basis of their different electron densities i.e. Mn (7.43 g/cm^3) > Ti (4.50 g/cm^3) also. In this respect, the darker NPs have been considered as Mn^{+n} while lighter one as TiO_2 photocatalyst. On the other hand, Mn(VII)-TiO_2 catalyst exhibited cubical, rectangular and hexagonal type of morphologies (Fig. 2.4a and 2.4b). As the size of Mn(VII) (0.060 nm) is smaller than Mn(II) ion (0.081 nm), due to stronger attractions between highly positive charged nucleus and valence electrons, the diameter of synthesized photocatalysts has been found in expected manner (~ 20-45 nm for Mn(VII)-TiO_2 and ~ 40-60 nm for Mn(II)-TiO_2).

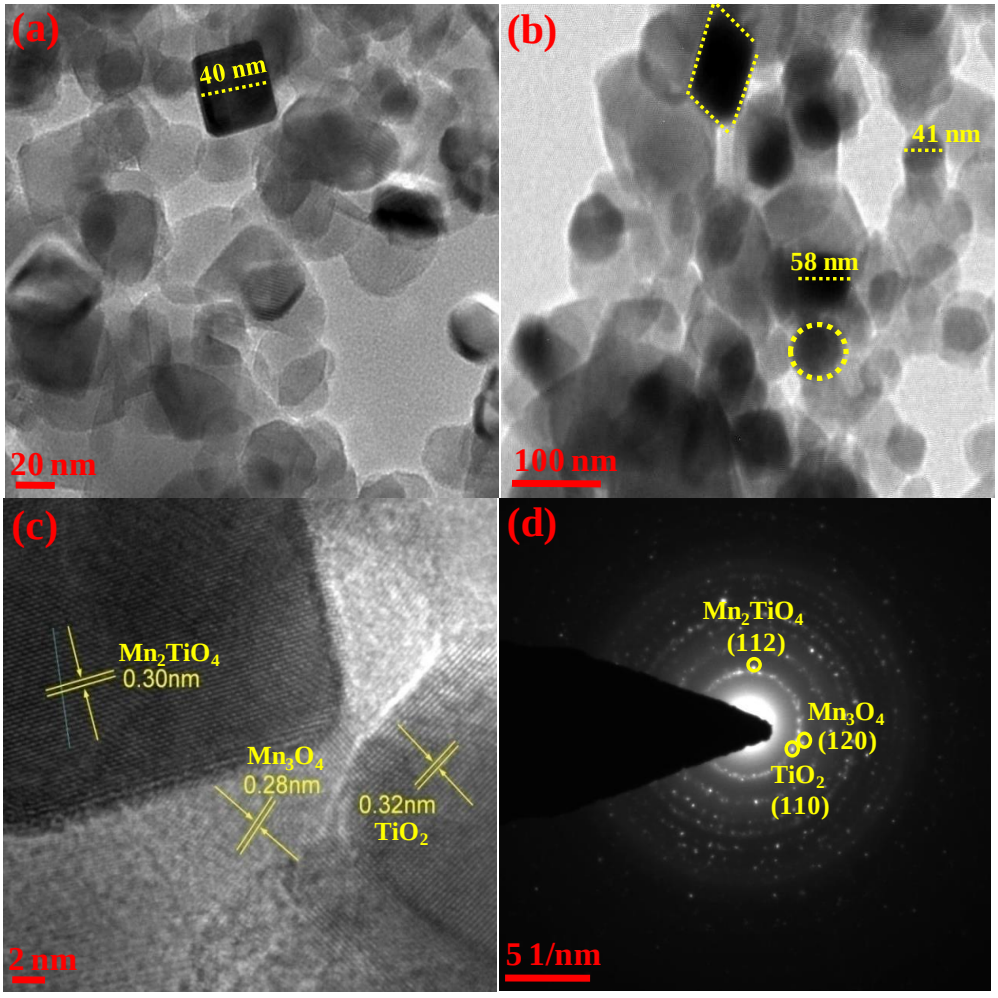

Figure 2.3. HRTEM representing the morphology (a and b), lattice fringes (c) and SAED pattern (d) of Mn(II)-TiO_2 co-catalyst.

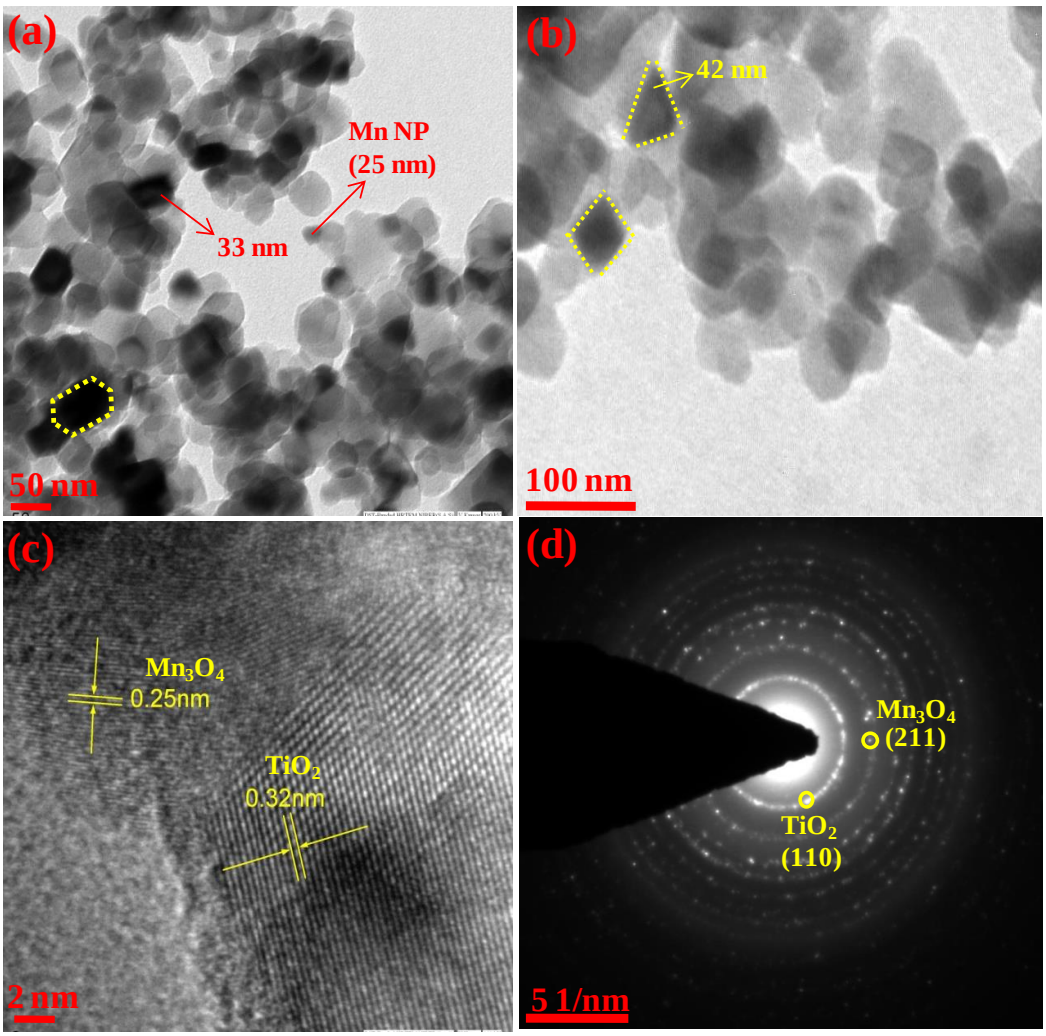

Figure 2.4. HRTEM analysis demonstrating the morphology (a and b), lattice fringes (c) and SAED pattern (d) of Mn(VII)-TiO_2 photocatalyst.

The valence states of Ti, O and Mn elements were verified using XPS analysis and for this the complete spectra for Ti2p, O1s and Mn2p is demonstrated by fig. 2.5. Two peaks at 639.1 and 640.3 eV (binding energy) were witnessed for $Mn2p_{3/2}$ state in Mn(II)-TiO_2 catalyst suggesting the formation of Mn^0 and Mn^{+2} (MnO) states. As expected, a Mn2p peak at 646 eV with a satellite peak at 648 eV was witnessed for Mn(VII)-TiO_2 co-catalyst which has been credited to Mn^{+7} oxidation state as evidenced by NIST database record and an earlier report as well (Mn^{+7} = 647 and 645.5 eV, respectively) [30]. Usually, a satellite peak is considered as an estimated guide for the positioning of main 2p peak. However, in case of Mn(II)-TiO_2 photocatalyst, two characteristic peaks at 458.5 eV and 464.3 eV were observed for two spin states of Ti ($Ti2p_{3/2}$ and $Ti2p_{1/2}$, respectively). While in Mn(VII)-TiO_2, a downfield shift of Ti peaks was observed. A similar kind of chemical shift was observed for O1s from 529.8 to 529.5 eV with the introduction of more prominent satellite peaks as the oxidation of Mn metal increased from II to VII. This chemical shift can be assigned to the electronic transfer from O to Ti^{+4} leading to the formation of Ti^{+3} species [31].

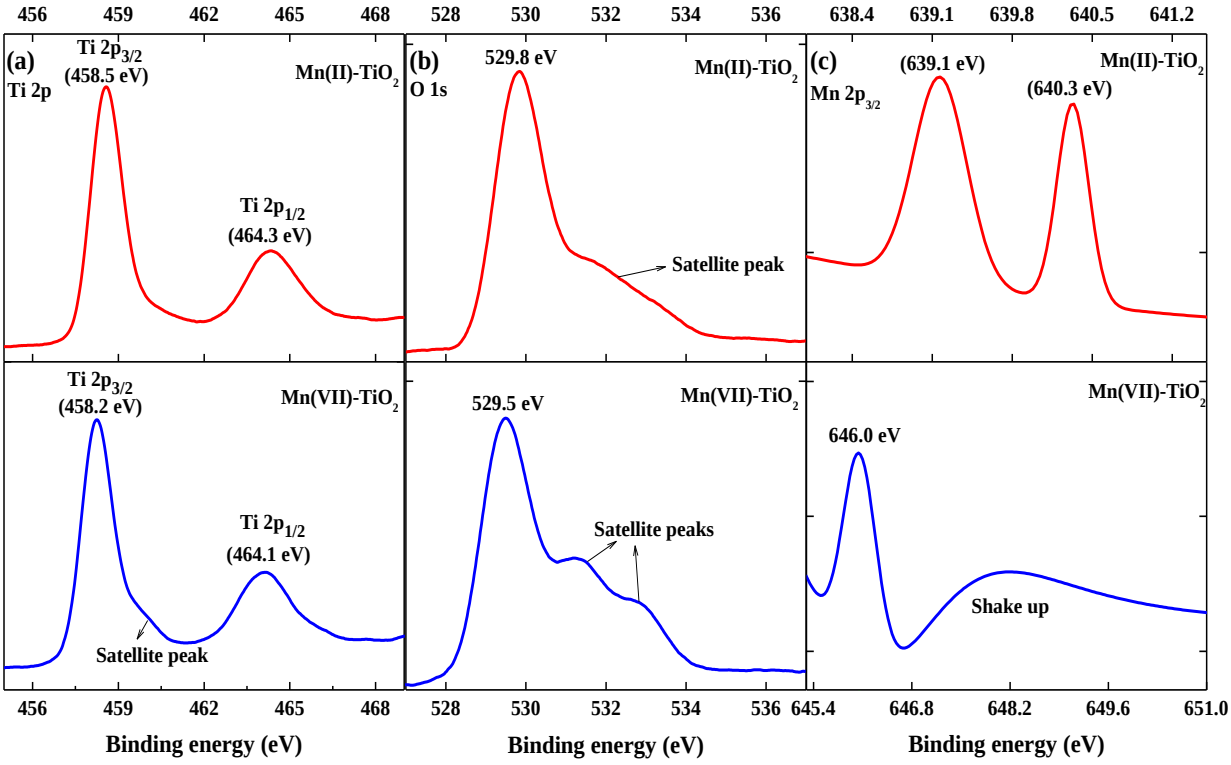

Figure 2.5. XPS analysis (a) Ti, (b) O and (c) Mn of Mn(II)-TiO_2 and Mn(VII)-TiO_2 photocatalysts.

2.3.2. Optical properties

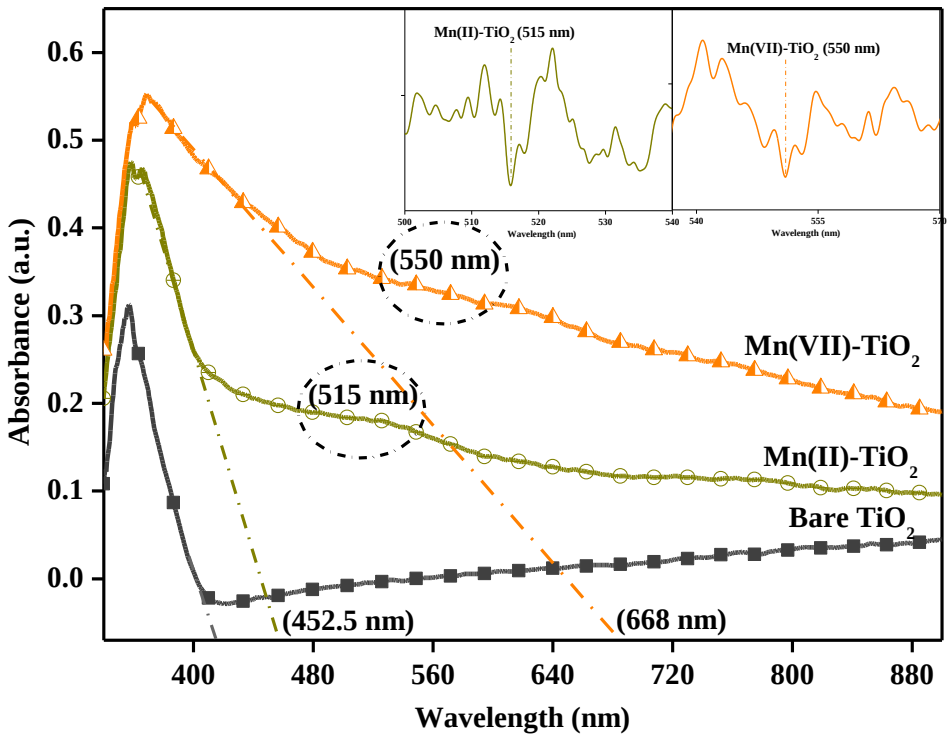

Figure 2.6. Diffuse reflectance spectra of bare and Mn^{+n}-TiO_2 photocatalysts with their corresponding single derivatives (inset).

The optical absorption edge of bare TiO_2 occurred at 405 nm due to transfer of electrons from valence band (VB) to conduction band (CB). The Mn loading in different oxidation states onto TiO_2 surface led to bathochromic shift of the absorption edge upto 700 nm (Fig. 2.6) due to the formation of new states into the mid band gap region of Mn^{+n}-TiO_2 nanocomposites [32]. It has been observed that as the oxidation state of loaded metal was increased, greater shift in TiO_2 absorption edge occurred (~ 452.5 nm for Mn(II)-TiO_2 and ~ 668 nm for Mn(VII)-TiO_2) which is due to more electron transfer between metal's d-electronic states and conduction band of TiO_2. The surface plasmonic resonances due to presence of Mn(II) and Mn(VII) ions were seen at ~ 515 and 550 nm, respectively due to $^6A_{1g} \rightarrow {}^4T_{1g}$ transitions [33]. However, quenching of these peaks was observed due to spin and parity forbidden transitions which was greater in Mn(VII) as compared to Mn(II) co-catalyst. Mn(VII)-TiO_2 photocatalyst also exhibited higher peak absorption intensity than Mn(II)-TiO_2 which can be ascribed to greater surface plasmons and higher visible light sensitivity [34]. The red shift enhancement (confirmed by single derivative function represented in fig. 2.6, inset) and higher spectral peak intensities showed the alteration in surface structural parameters of

Mn^{+n}-TiO_2 co-catalysts which was later confirmed by photoluminescence (PL), PZC and charge demand analysis also.

In order to determine the efficiency of prepared catalysts in terms of lifetime of charge carrier and recombination rate, PL was analysed by exciting the photocatalysts at wavelength of 340 nm (Fig. 2.7). Several peaks at 404, 422, 448, 460, 485 and 529 nm were obtained. The major bands at 422, 448 and 485 nm are attributed to free excitation emission of the band gap, defective sites present in the TiO_2 lattice [35] and charge transfer between Ti^{3+} to oxygen anion in TiO_6^{2-}, respectively [36]. The bands over 450-500 nm appeared due to recombination of electrons from higher to lower states but the bands above 500 nm are unknown [37]. Interestingly, Mn(II) co-catalyst showed considerable quenching of emission peak intensities as compared to Mn(VII) state. On this basis, it has been inferred that lower oxidation state of Mn metal i.e. Mn(II) on TiO_2 surface generates more defective sites and greater charge carrier trapping suppressing the recombination rate which might be responsible for its higher activity for some specific substrate molecules. The greater quenching by Mn(II)-TiO_2 catalyst can possibly assigned to the formation of Mn_2TiO_4 and free Mn(0) species as well which led to greater charge separation.

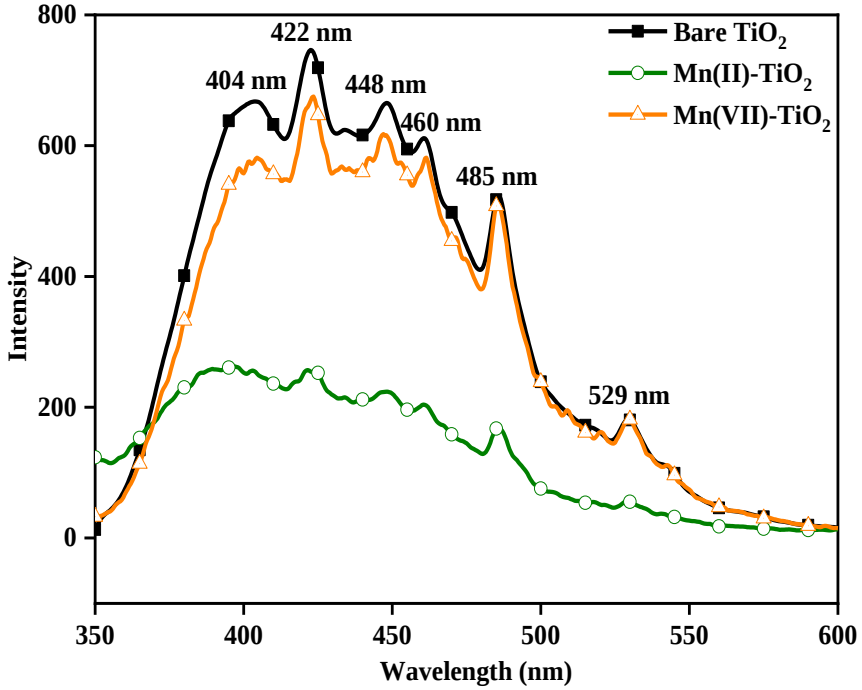

Figure 2.7. Photoluminescence spectra of different bare and Mn^{+n} loaded TiO_2 nanoparticles.

2.3.3. Electrokinetic properties

The hydrodynamic size analysis in fig. 2.8 showed that the Mn deposition increased the size of Mn^{+n}-TiO_2 co-catalysts compared to bare TiO_2 confirming that impregnation positioned the Mn^{+n} ions onto the surface of TiO_2. An expected increase in the size of Mn^{+n}-TiO_2 nanocatalysts was also observed based on the ionic size of Mn^{+n} cation (Mn(VII); 0.060 nm < Mn(II); 0.081 nm). Thus, the observed size of hydrated Mn(II)/(VII) co-catalysts is: 60, 113 and 225 nm for bare TiO_2, Mn(VII)-TiO_2 and Mn(II)-TiO_2, respectively.

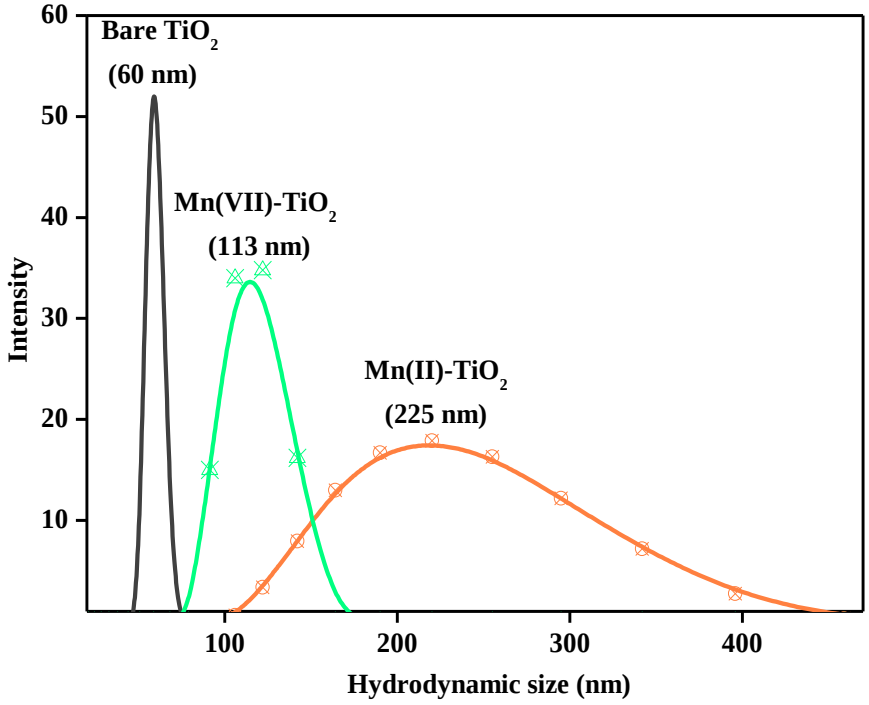

Figure 2.8. Comparative hydrodynamic size of various Mn^{+n}-TiO_2 and bare TiO_2 nanocatalysts.

To know the effect of different oxidation states of Mn^{+n}-TiO_2 co-catalysts various electrokinetic properties, PZC was evaluated (Fig. 2.9). Natural pH of dispersed catalysts was came out to be 8, 7.34 and 6.8 for bare TiO_2, Mn(II)-TiO_2 and Mn(VII)-TiO_2, respectively which discloses more acidity prevailing in the medium due to the presence of Mn^{+n} ions. It has been observed that zeta potential at natural pH becomes more negative (bare TiO_2 = -20.48, Mn(II)-TiO_2 = -27.7, Mn(VII)-TiO_2 = -33.4 mV) with increased oxidation state of Mn^{+n} ion. As surface charge of prepared photocatalyst got increased (towards positive), the number of counter ions in dispersed medium also increased resulting in enhanced zeta potential. Higher magnitude of zeta potential depicts greater inter ionic repulsions among the molecules of Mn(VII)-TiO_2 nanocatalyst so is the greater dispersion stability. Further, lower

PZC values of 3.28 and 3 were evaluated for Mn(II)-TiO_2 and Mn(VII)-TiO_2 catalyst, respectively compared to 6.58 for bare TiO_2.

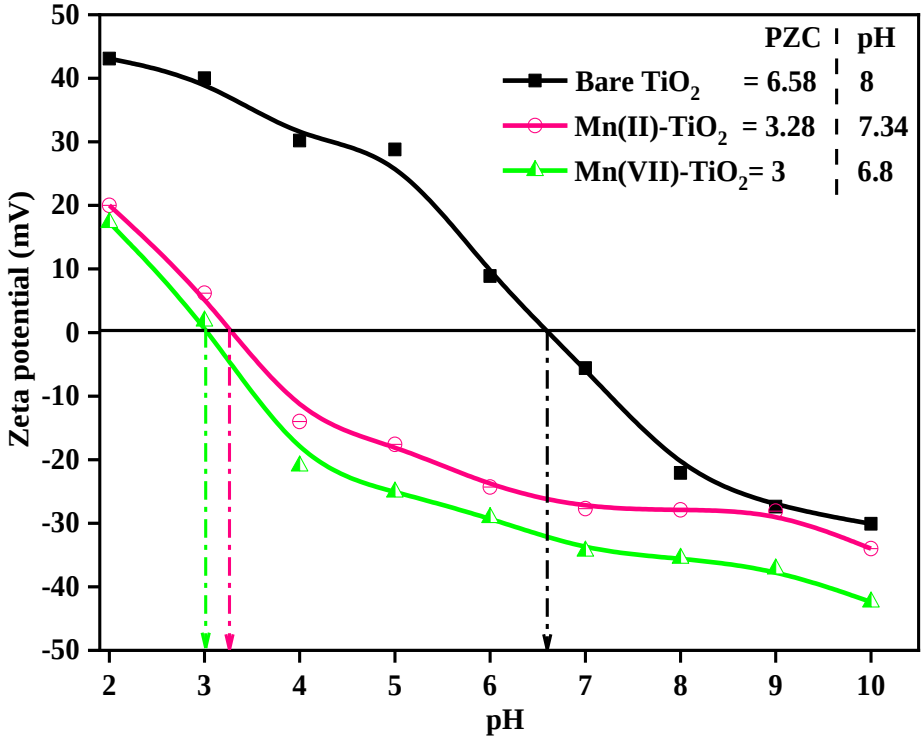

Figure 2.9. Evaluation of point of zero charge (PZC) of different photocatalysts by determining the zeta potential at different pH values.

The transport of counter ions due to fluid flow pressure gives rise to a net charge transport which is measured in terms of streaming potential. The observed values of streaming potential for synthesized catalysts are: -57, -102 and -224 mV for bare TiO_2, Mn(II)-TiO_2 and Mn(VII)-TiO_2, respectively. An increased flow of counter ions has been witnessed with increased charge density on deposited Mn^{+n} metal ion. On the basis of observed streaming potential, surface charge demand (μeq/g) was found in the following order: bare TiO_2 (1.12) < Mn(II)-TiO_2 (1.95) < Mn(VII)-TiO_2 (6.52). Table 2.1 summarizes all the electrokinetic parameters possessed by various Mn^{+n}-TiO_2 and bare TiO_2 nanocatalysts. Charge demand values indicate the variation in surface charge density exhibited by different co-catalysts due to presence of Mn^{+n} in different ionic/oxidation states.

Table 2.1. Streaming potential, surface charge demand and other surface parameters exhibited by bare and Mn^{+n} loaded TiO_2 nanocatalysts.

Sr. No.	Catalysts	Natural pH	Zeta potential (mV) at natural pH	PZC	Streaming potential (mV)	Charge Demand (µeq/g)
1.	Bare TiO_2	8	-20.48	6.58	-57	1.12
2.	Mn(II)-TiO_2	7.34	-27.7	3.28	-102	1.95
3.	Mn(VII)-TiO_2	6.8	-33.4	3	-224	6.52

2.3.4. Adsorption and photocatalytic degradation properties

Various Mn^{+n}-TiO_2 photocatalysts were found to exhibit different kind of interactions with differently charged substrate molecules (cationic and anionic) depending on their oxidation states and electrokinetic properties. Figures 2.10a and 2.10b demonstrate the adsorption of cationic and anionic molecules on the Mn^{+n}-TiO_2 co-catalyst surface. Out of the total substrates amount taken (cationic = 0.1 µmol and anionic = 2 µmol); the maximum amount of 0.049 µmol (cationic) and 0.71 and 0.55 µmol of salicylic acid and salicylaldehyde, respectively has been adsorbed by Mn(VII) and Mn(II) co-catalysts. More interestingly, the adsorption of cationic substrates has been witnessed in the following manner: Mn(VII)-TiO_2 > Mn(II)-TiO_2 > Bare TiO_2 which got reversed after Mn(II) and Mn(VII) ions impregnation for anionic substrates (Mn(II)-TiO_2 > Mn(VII)-TiO_2 > Bare TiO_2).

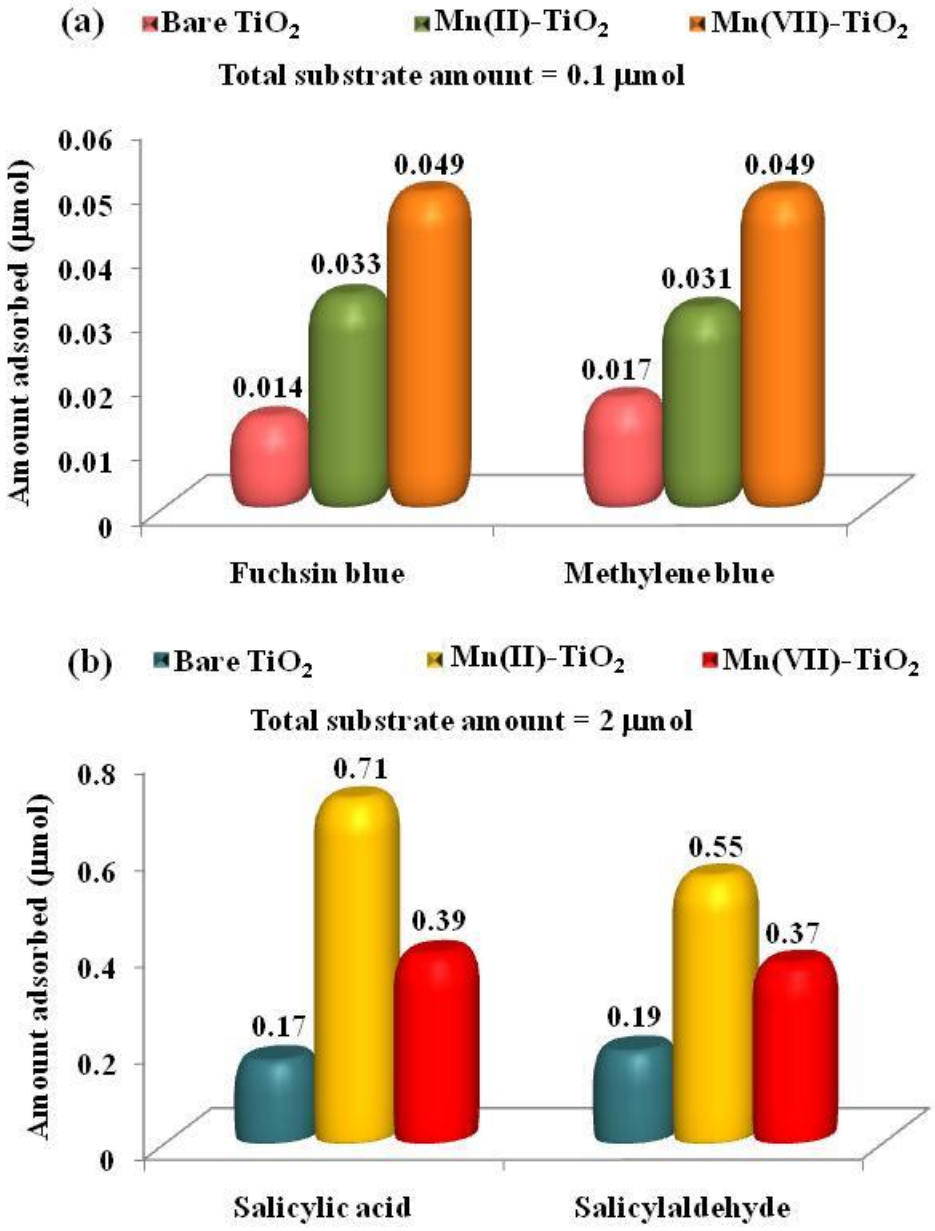

Figure 2.10. Adsorption efficiencies exhibited by different bare and Mn^{+n}-TiO_2 nanocatalysts for (a) cationic (fuchsin blue and methylene blue) and (b) anionic (salicylic acid and salicylaldehyde) substrate molecules.

This behaviour can be explained on the basis of observed streaming potential (Bare TiO_2 (-57 mV), Mn(II)-TiO_2 (-102) and Mn(VII)-TiO_2 (-224)) and surface charge demand (Bare TiO_2 (1.12), Mn(II)-TiO_2 (1.95) and Mn(VII)-TiO_2 (6.52 µeq/g)) of various nanocatalysts. Despite of having higher oxidation state of Mn^{+n} ion in Mn(VII)-TiO_2 photocatalyst, the adsorption of anionic substrates was found greater in Mn(II)-TiO_2 catalyst. This is due to more negative zeta and streaming potential values for Mn(VII) than Mn(II) impregnated TiO_2 catalysts which tend to repel the negatively charged (anionic) substrate molecules effectively. As a

result, the adsorption and photooxidation of anionic substrates was found greater by Mn(II)-TiO_2 catalyst due to lesser repulsions and greater catalyst-substrate associations. It has been inferred that adsorption behaviour depends not only on the direct surface charge of the prepared catalyst but on the zeta and streaming potential also. However, it has also been observed that the manganese loaded TiO_2 photocatalysts always show higher adsorption behaviour than bare TiO_2. Higher charge density imparted by impregnated metal ions bearing different oxidation states offer different interactions to differently charged substrate molecules.

The photocatalytic activity of synthesized Mn^{+n}-TiO_2 nanocatalysts occurred in accordance with the catalyst-substrate adsorption interactions. The maximum decrease in absorption peak intensities of cationic/anionic substrates due to complete oxidation after treatment with different Mn^{+n}-TiO_2 co-catalysts under visible irradiation have been shown in fig. 2.11. The complete photodegradation of cationic substrates was achieved within 120 min. (F.B.) and 25 min. (M.B.) while for anionic molecules, it occurred within 1 h duration for S.A. As salicylaldehyde is the reduced form of salicylic acid, its complete photooxidation will require more time as compared to salicylic acid which is reflected in their respective absorption peak intensities also. In a photocatalytic process, the impregnated metal ions are excited under visible light irradiation which transfer the excited electrons into the C.B. of TiO_2 for reduction purposes while the positive holes left behind within metal ions are utilised for various oxidative reactions [38]. It can be observed that inspite of having higher light harvest, the Mn(VII)-TiO_2 catalyst showed lower degradation for anionic substrates. It has been concluded that apart from catalyst properties, the nature of substrate molecules (cationic/anionic) also play a significant role. The Mn(VII)-TiO_2 catalyst showed enhanced attraction and degradation for cationic substrates due to its suitable zeta (-33.4 mV) and streaming potential (-224 mV) values. In a photocatalytic process, the substrate molecules are first adsorbed on the surface of catalyst through weak Vander wall or some ionic interactions and then are photochemically processed. Similarly, in the present situation, adsorption assisted photodegradation has been done which is much dependent upon the ionic interactions between catalyst-substrate molecules. Therefore, Mn(VII)-TiO_2 photocatalyst showed greater adsorption and photodegradation capacity for cationic substrates as a consequence of various electrokinetic phenomena. On the other hand, Mn(II)-TiO_2 showed higher attraction and degradation for anionic substrates only.

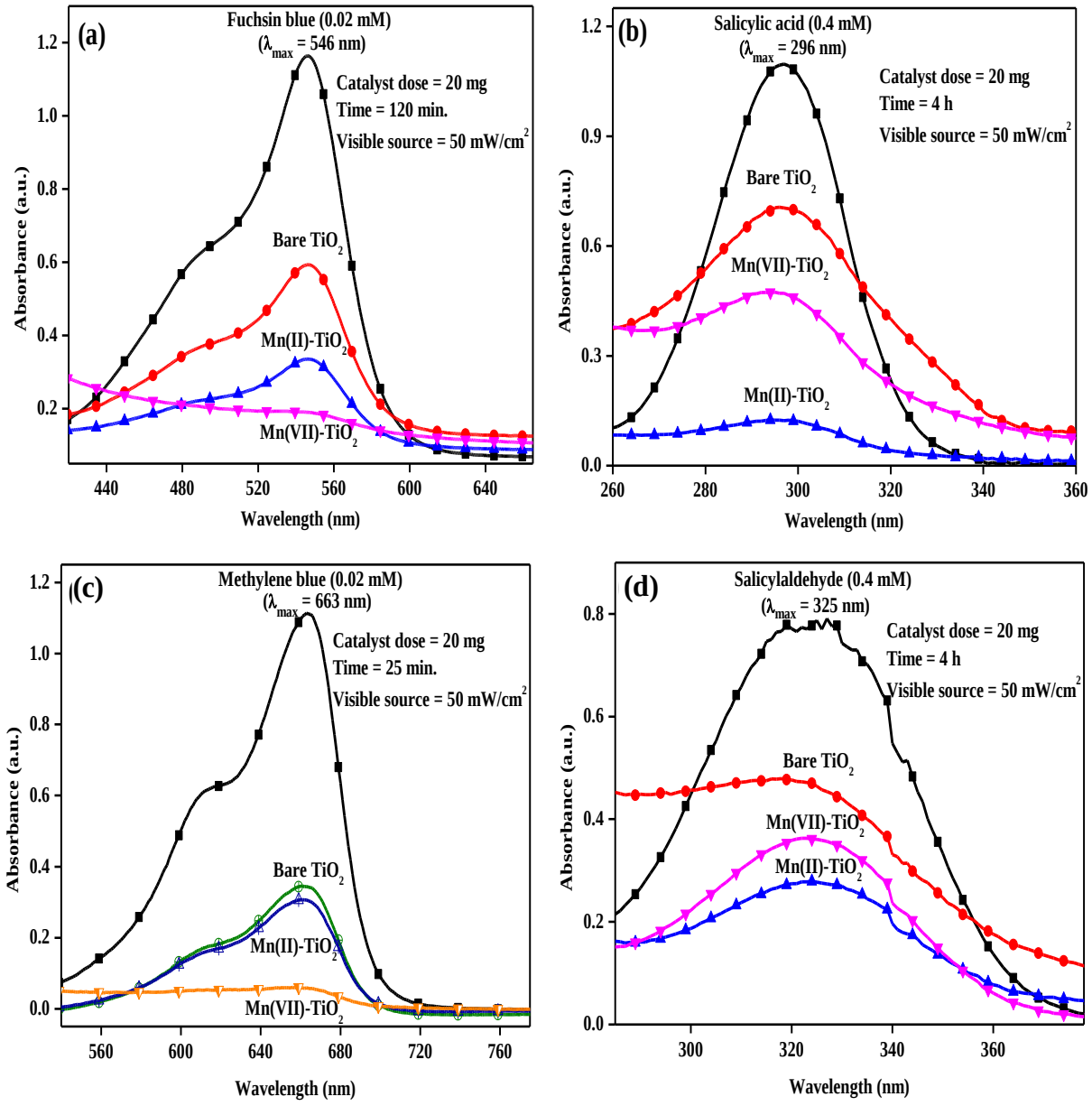

Figure 2.11. UV-visible spectra demonstrating degradation efficiencies of different photocatalysts for (a) cationic and (b) anionic substrate molecules.

The above obtained photodegradation results decipher that the type of surface charge on metal ionic species, photocatalyst adsorption behaviour, nature of substrate molecules and visible light sensitization cumulatively effect the photooxidative degradation efficiency of a particular photocatalyst. Further, the kinetic analysis in figure 2.12 revealed that each degradation process followed pseudo first order kinetics according to the equation:

$$kt = -2.303 \log \frac{C}{C_0}$$

where, k is the pseudo first order rate constant, t is time (min./h), C and C_0 are final and initial concentrations (conc.) of substrate molecules.

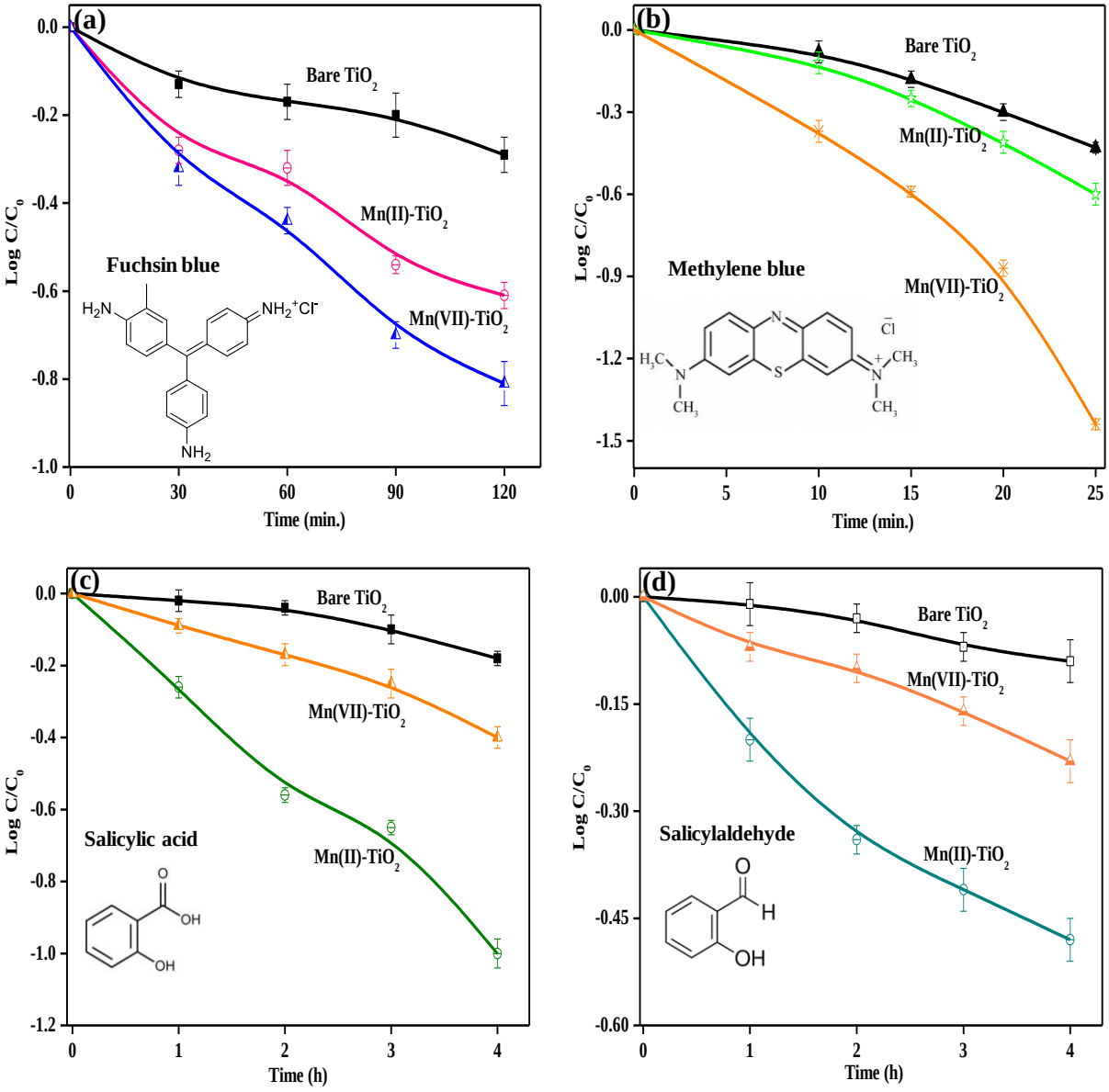

Figure 2.12. Degradation rates for cationic (fuchsin blue and methylene blue) (a, b) and anionic (salicylic acid and salicylaldehyde) (c, d) substrate molecules after treatment with different Mn^{+n}-TiO_2 co-catalysts under visible irradiation.

The time course plots reflect that the presence of Mn^{+n} in variable oxidation states on TiO_2 surface lead to significant enhancement in photocatalytic activity compared to bare TiO_2. This is due to the fact that impregnated metal act as an electron sink by capturing

photogenerated electrons thereby offering greater availability of highly oxidizable holes. Also, the additional surface charge provided by metal cations attract greater number of molecules to be degraded depending upon the nature of charge (cationic/anionic) on the adsorbed substrate. In this reference, the maximum photocatalytic degradation of cationic and anionic molecules has been shown by Mn(VII)-TiO_2 and Mn(II)-TiO_2, respectively.

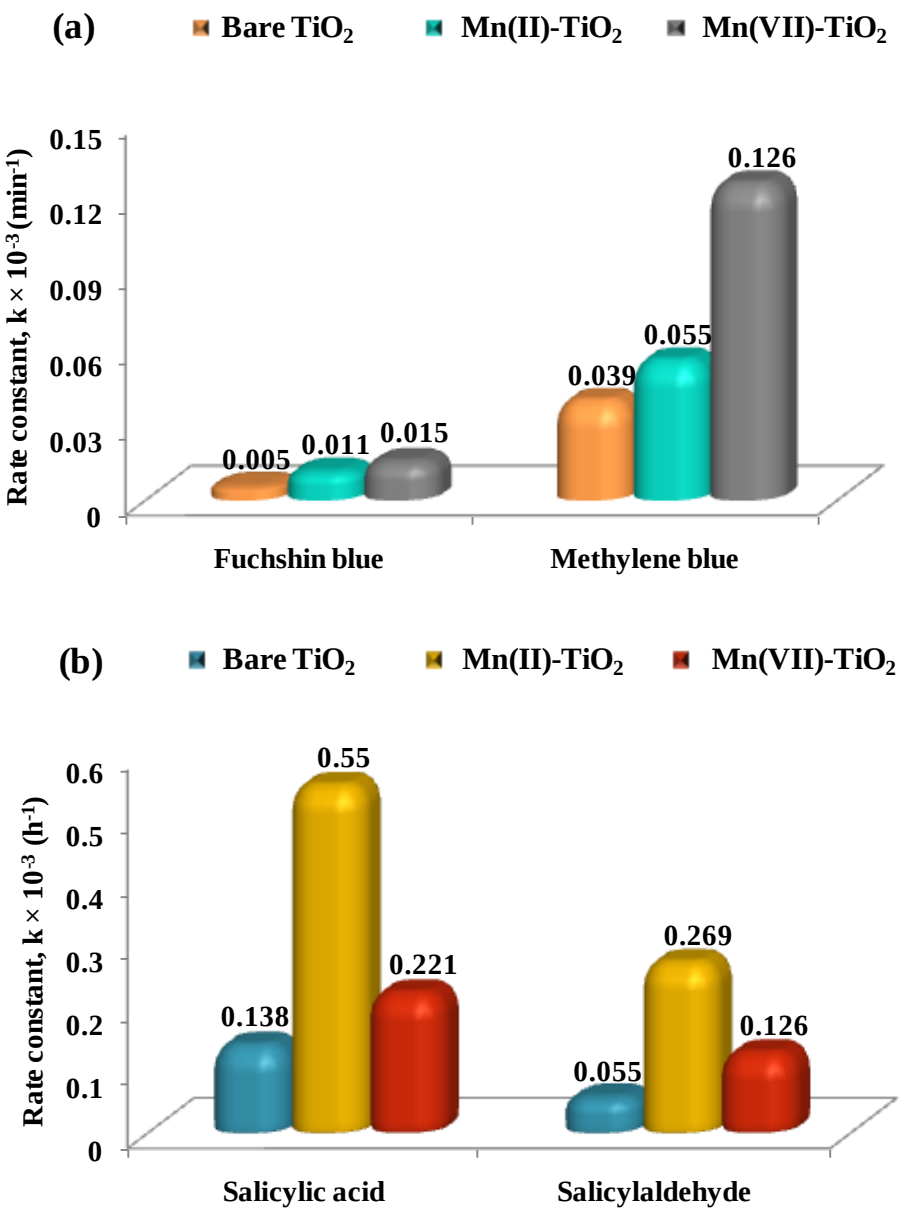

Figure 2.13. Rate constant, k values exhibited by bare and Mn^{+n}-TiO_2 nanocatalysts for the degradation of (a) cationic and (b) anionic substrate molecules.

The Mn(VII)-TiO_2 catalyst showed degradation rate constant, k values of 0.015 and 0.126 × 10^{-3} min^{-1} for F.B. and M.B., respectively. On the other hand, for S.A. and S.D. values of 0.55 and 0.269 × 10^{-3} h^{-1}, respectively by Mn(II)-TiO_2 have been evaluated (Fig. 2.13). The comparative degradation rates in terms of k values shown by various Mn^{+n}-TiO_2 co-catalysts have been demonstrated in figure 2.13. In brief, the adsorption and photocatalytic degradation properties are appreciably varied as a function of oxidation state, work function and surface structural peculiarities of M^{+n}-TiO_2 nanocomposites. Further, the greater charge demand possessed by various Mn^{+n}-TiO_2 photocatalysts due to different oxidation states of deposited Mn^{+n} metal lead to more attraction towards respectively charged substrate molecules in demand which would be beneficial in future for enhanced adsorptions and photocatalytic behaviour .

References

[1] Y. Ma, X. Wang, Y. Jia, X. Chen, H. Han, C. Li, Chem. Rev. 114 (2014) 9987-10043.

[2] L.G. Devi, R. Kavitha, Appl. Surf. Sci. 360 (2016) 601-622.

[3] M. Pelaez, N.T. Nolan, S.C. Pillai, M.K. Seery, P. Falaras, A.G. Kontos, P.S. Dunlop, J.W. Hamilton, J.A. Byrne, K. O'shea, M.H. Entezari, D.D. Dionysiou, Appl. Catal. B Environ. 125 (2012) 331-349.

[4] I. Ali, M. Suhail, Z.A. Alothman, A. Alwarthan, RSC Adv. 8 (2018) 30125-30147.

[5] R. Sedghi, H.R. Moazzami, S.S.H. Davarani, M.R. Nabid, A.R. Keshtkar, J. Alloy. Compd. 695 (2017) 1073-1079.

[6] M.A. Henderson, Surf. Sci. Rep. 66 (2011) 185-297.

[7] A. Zaleska, Recent Pat. Eng. 2 (2008) 157-164.

[8] S.G. Kumar, L.G. Devi, J. Phys. Chem. A 115 (2011) 13211-13241.

[9] Z. Zhang, J.T. Yates Jr, Chem. Rev. 112 (2012) 5520-5551.

[10] Z. Zheng, B. Huang, X. Qin, X. Zhang, Y. Dai, M.H. Whangbo, J. Mater. Chem. 21 (2011) 9079-9087.

[11] V. Nguyen, Q. Cai, C.A. Grimes, J. Colloid Interface Sci. 483 (2016) 287-294.

[12] Z.D. Mahmoudabadi, E. Eslami, M. Narimisa, J. Colloid Interface Sci. 529 (2018) 538-546.

[13] N. Gupta, B. Pal. J. Mol. Catal. A Chem. 371 (2013) 48-55.

[14] S.K.M. Saad, A.A. Umar, M.I.A. Umar, M. Tomitori, M.Y.A. Rahman, M.M. Salleh, M. Oyama, ACS Omega 3 (2018) 2579-2587.

[15] L. Yafeng, Y. Jiahui, Z. Yanhong, J. Mater. Appl. 7 (2018) 12-19.
[16] X.Z. Li, F.B. Li, Environ. Sci. Technol. 35 (2001) 2381- 2387.
[17] B. Pal, R. Kaur, I.S. Grover, J. Ind. Eng. Chem. 33 (2016) 178-184.
[18] H. Feng, L.E. Yu, M.H. Zhang, Mater. Res. Bull. 48 (2013) 672-681.
[19] D. Kim, Y. Im, K.M. Jeong, S.M. Park, M.H. Um, M. Kang, Bull. Korean Chem. Soc. 35 (2014) 2295-2298.
[20] M.Y. Rafiq, F. Iqbal, F. Aslam, M. Bilal, N. Munir, I. Sultana, F. Ashraf, F. Manzoor, N. Hassan, A. Razaq, J. Alloy. Compd. 729 (2017) 1072-1078.
[21] M.T. Greiner, L. Chai, M.G. Helander, W.M. Tang, Z.H. Lu, Adv. Funct. Mater. 22 (2012) 4557-4568.
[22] J. Choi, H. Park, M.R. Hoffmann, J. Phys. Chem. C 114 (2010) 783-792.
[23] N. Gupta, P. Bansal, B. Pal, J. Exp. Nanosci. 10 (2015) 148-160.
[24] B.R. Cuenya, Thin Solid Films 518 (2010) 3127-3150.
[25] R. Kaur, B. Pal, New J. Chem. 39 (2015) 5966-5976.
[26] M. Rehan, X. Lai, G.M. Kale, CrystEngComm 13 (2011) 3725-3732.
[27] P. Pongwan, B. Inceesungvorn, K. Wetchakun, S. Phanichphant, N. Wetchakun, Engineering Journal 16 (2012) 143-151.
[28] S. Zhu, S. Liang, Q. Gu, L. Xie, J. Wang, Z. Ding, P. Liu, Appl. Catal. B Environ. 119 (2012) 146-155.
[29] H. Zhu, Y. Wu, X. Zhao, H. Wan, L. Yang, J. Hong, Q. Yu, L. Dong, Y. Chen, C. Jian, J. Wei, P. Xu, J. Mol. Catal. A Chem. 243 (2006) 24-30.
[30] M.C. Biesinger, B.P. Payne, A.P. Grosvenor, L.W.M. Lau, A.R. Gerson, R.S.C. Smart, Appl. Surf. Sci. 257 (2011) 2717-2730.
[31] R.A. Rather, S. Singh, B. Pal, Appl. Catal. B Environ. 213 (2017) 9-17.
[32] S.M. Chang, W.S. Liu, Appl. Catal. B Environ. 156 (2014) 466-475.
[33] S. Paul, A. Choudhury, Int. J. Innov. Res. Dev. 1 (2012) 24-31.
[34] A. Tanaka, S. Sakaguchi, K. Hashimoto, H. Kominami, ACS Catal. 3 (2013) 79-85.
[35] S.F. Chen, J.P. Li, K. Qian, W.P. Xu, Y. Lu, W.X. Huang, S.H. Yu, Nano. Res. 3 (2010) 244-255.
[36] E. Liu, L. Kang, F. Wu, T. Sun, X. Hu, Y. Yang, H. Liu, J. Fan, Plasmonics 9 (2014) 61-70.
[37] M.O. Ansari, M.M. Khan, S.A. Ansari, J. Lee, M.H. Cho, RSC Adv. 4 (2014) 23713-23719.
[38] M. Janczarek, E. Kowalska, Catalysts 7 (2017) 317.

SECTION - 2B

Effective photooxidative degradation of methyl viologen using Mn^{2+}/Mn^{7+}-TiO_2 nanocomposites under solar irradiation

2.1. Introduction

Metal ion (M^{n+}) based TiO_2 nanocomposites are believed to have better adsorption and photocatalytic properties than other conventional M^0-TiO_2 nanocatalysts [1-4]. The co-catalytic effect of these M^{n+}-TiO_2 nanocatalysts is considered to be the result of different oxidation states [5,6], surface charge density, isoelectric point, band energetics [7], electrokinetic [8] and interfacial electron transfer phenomena [9-11]. For example, metal ions Cr^{3+}, Fe^{3+} and V^{5+} impregnated TiO_2 photocatalysts have been found to have efficient photoredox properties [12,13]. Besides above, the impregnation method employed for the synthesis of these nanocomposites is simple, effective and does not require the use of any harmful UV radiations as in photodeposition method. Doped or impregnated metal ions are either located over the support surface or tend to occupy the interstitial sites depending on the ionic radii of metal ions [14]. The higher charge built over the surface of titania due to presence of metal ions also provide enhanced adsorption efficiencies rather than neutral metal atoms. In this regard, Fe^{3+}, Fe^0, Cu, Ag, Au^0, Au^{3+}, Cr^{3+} and Cr^{6+} have also been compared for iodide oxidation to iodine [15]. Various factors such as the oxidation state, ionic radii, catalyst surface acidity and electron affinity have been considered to influence the photocatalytic activity to a great extent [16-18]. Further, it has been established that appropriate doping of Sn^{4+} ions onto TiO_2 induces lower electron-hole pair recombination rate thereby increasing the degradation efficiency [19].

As solid-liquid heterogeneous photocatalysis is an interfacial phenomenon and depends upon the adsorption capability of the solid catalyst. Therefore, the photocatalyst adsorption efficiency/affinity is an important prerequisite to study. In a study, Al^{3+} modified TiO_2 nanocatalysts are found to offer appreciable adsorption efficacy for different kinds of dye molecules viz; rhodamine B, malachite green and alizarin red, etc [20]. Fe^{3+} and Pt^{4+} impregnated TiO_2 nanostructures of different shapes have also been evaluated for their adsorption behavior and photocatalytic oxidation of EBT dye under UV irradiation [21]. It was observed that the extra positive charge provided by metal ions facilitates greater interionic catalyst-substrate association enhancing the photodegradation rates. Many studies

are suggesting the effect of different metal ions in 1+, 2+, 3+ and 4+ oxidation states on co-catalysis of TiO_2 [22]. These studies are unable to depict whether this activity is due to the presence of different types of metal ions or due to their different oxidation states. If the root cause of enhanced activity is different oxidation states, then it is somewhat difficult to compare its effect on photochemical, electrokinetic and photocatalytic parameters.

Many metals bear huge variation in oxidation states such as Mn, Cr, Fe, Os, Ru and Re, etc. Among these, the low-cost Mn metal due to its capability of introducing intra band gap states [23], visible light sensitivity [24] and the appreciable gap between two oxidation states i.e. Mn^{2+} and Mn^{7+} provokes to study their impact on various photophysical and electronic parameters of Mn^{n+}-TiO_2 nanocomposites. In our earlier report, we have obtained a significantly higher surface charge demand (μeq/g) for Mn^{n+}-TiO_2 nanocomposites compared to bare TiO_2 [25]. Furthermore, the reduction potential of Mn (-1.026 V) is also much higher than the C.B. of TiO_2 (-0.3 V) which makes it unsuitable to get photodeposited. Hence, an easy and facile impregnation method can be exploited to impregnate Mn^{2+} and Mn^{7+} ions over TiO_2 surface. If the catalyst surface is positively charged there can be different catalytic surface acidity/basicity which will interact differently with cationic, anionic and neutral substrate molecules. Also, the nature and type of substrate chosen is an important factor determining a photocatalytic process. Therefore, we wanted to investigate the impact of different oxidation states of Mn^{n+} ions in co-catalysis, surface structural properties and type of interactions that occur between Mn^{n+}-TiO_2 nanocomposites and ionic substrate molecules. In this need, Mn^{n+} ions have been impregnated in 2+ and 7+ oxidation states separately onto TiO_2 surface to examine their adsorption and photocatalytic degradation behavior for the oxidative degradation of Methyl viologen (M.V.)/paraquat under sunlight irradiation. This molecule is a big threat to human life as it is a toxic herbicide and takes part in redox cycling process of the human body and is much needed to be effectively separated and decomposed.

2.2. Experimental details

2.2.1. Chemicals and Reagents

Manganese (II) sulphate monohydrate ($MnSO_4$. H_2O; 98%) and potassium permanganate ($KMnO_4$; 99%) were purchased from Loba Chemie, India. The commercially available form of TiO_2; Degussa P25 (70% Anatase + 30% Rutile form) was received as a gift from Degussa Corporation, Germany. Methyl viologen dichloride hydrate (paraquat; 98%) from Sigma-

Aldrich was used. Distilled water (D. I.) from an ultrafiltration system (Milli-Q, Millipore) with a measured conductivity of 35 mho cm^{-1} at 25 ^{0}C was used.

2.2.2. Synthesis of Mn^{n+}-TiO_2 nanocomposites

The Mn^{n+} impregnated TiO_2 nanocomposites were synthesized in a similar way as mentioned in chapter 2 (section 2.2.2). Additionally, the varying amounts of metal salt solutions (0.01 M; Mn(II)SO_4 for Mn^{2+} and $KMnO_4$ for Mn^{7+} impregnation) were used to impregnate the 0.2-3 wt% of Mn^{n+} ions.

2.2.3. Catalyst characterization

All the characterizations were done using the techniques mentioned in chapter 1 (section 1.5).

2.2.4. Adsorption and photocatalytic activity

The adsorption behavior of different Mn^{n+}-TiO_2 nanocomposites was assessed by treating herbicide; Methyl viologen (5 mL; 20 ppm) with catalyst dose of 10-50 mg under continuous stirrings in dark for 12 h. The amount of adsorbate (M.V.) adsorbed at equilibrium was calculated using equation [26]:

$$q_e = \frac{(C_0 - C_e)V}{W}$$

where C_0 and C_e are the initial and equilibrium conc (μg/mL) of substrate, V is the volume (mL) of solution and W is the mass (mg) of photocatalysts used. Further, the adsorption followed photocatalytic degradation of M.V. was observed under sunlight irradiation (5.29 kWh/m^2) until the complete photooxidation was done. The reaction samples were then centrifuged, separated and analyzed by UV-Vis spectrophotometer (Shimadzu) at λ_{max} = 257 nm at regular time intervals.

2.3. Results and Discussion

2.3.1. Optical properties

During DRS analysis, initially, the dark spectra was recorded in the absence of light and then the spectra of TiO_2 was taken as a reference in the presence of light. The TiO_2 photocatalyst exhibited an absorption peak at 355 nm due to electron transfer from its valence band (V.B.) to the conduction band (C.B.) (fig. 2.1). This peak further showed bathochromic shifts in Mn^{n+} impregnated TiO_2 nanocomposites. In the case of Mn^{2+}-TiO_2 co-catalyst consisting d^5

system, a small quenched peak (due to spin and parity forbidden transitions) at ~ 515 nm was observed due to $^6A_{1g} \rightarrow {}^4T_{1g}$ transition [27] due to octahedral geometry of the co-catalyst. On the other hand, extended visible light absorptions shown by the Mn^{7+}-TiO_2 catalyst exhibiting a d^0 system have been attributed to L → M charge transfer transitions ($O^{2-} \rightarrow Mn^{7+}$).

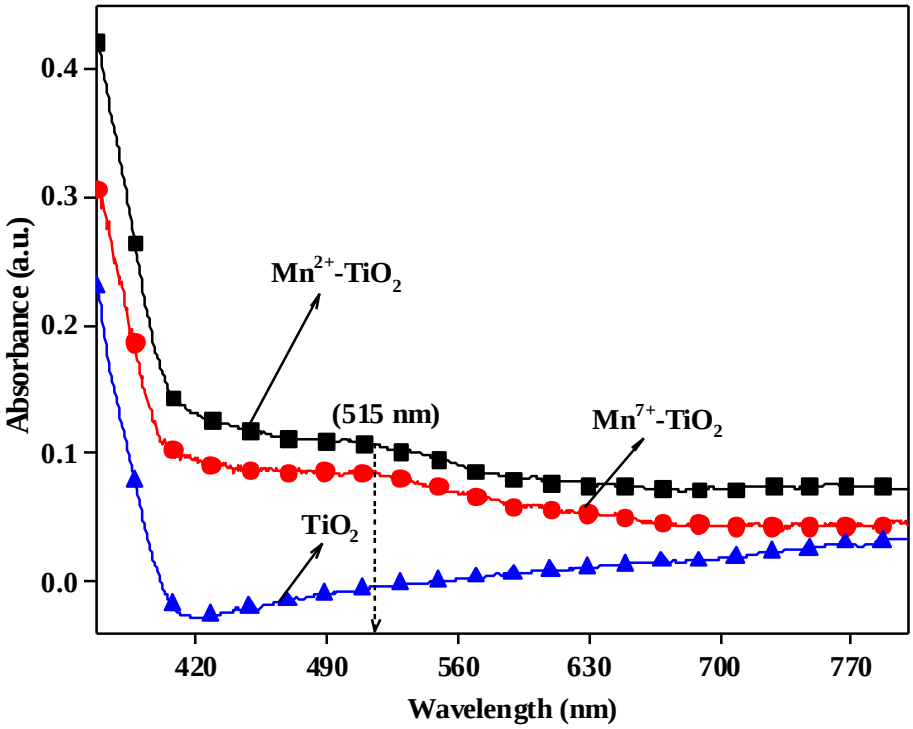

Figure 2.1. Diffuse reflectance spectra (DRS) of bare TiO_2 and Mn^{n+}-TiO_2 nanocomposites

It has also been observed that as the wt% of impregnated Mn^{n+} ions increased on the surface of TiO_2, the DRS absorption intensity also increased in a respective manner due to enhanced surface plasmons generated by Mn^{n+} ions (Mn^{2+} and Mn^{7+}) (fig. 2.2). Usually, the plasmon bands are considered to vary as a function of the co-catalyst size also. Therefore, continuous hyperchromic shifts with increased wt% of Mn^{n+} ions have been regarded as a consequence of regular growth of Mn^{n+} NPs as well.

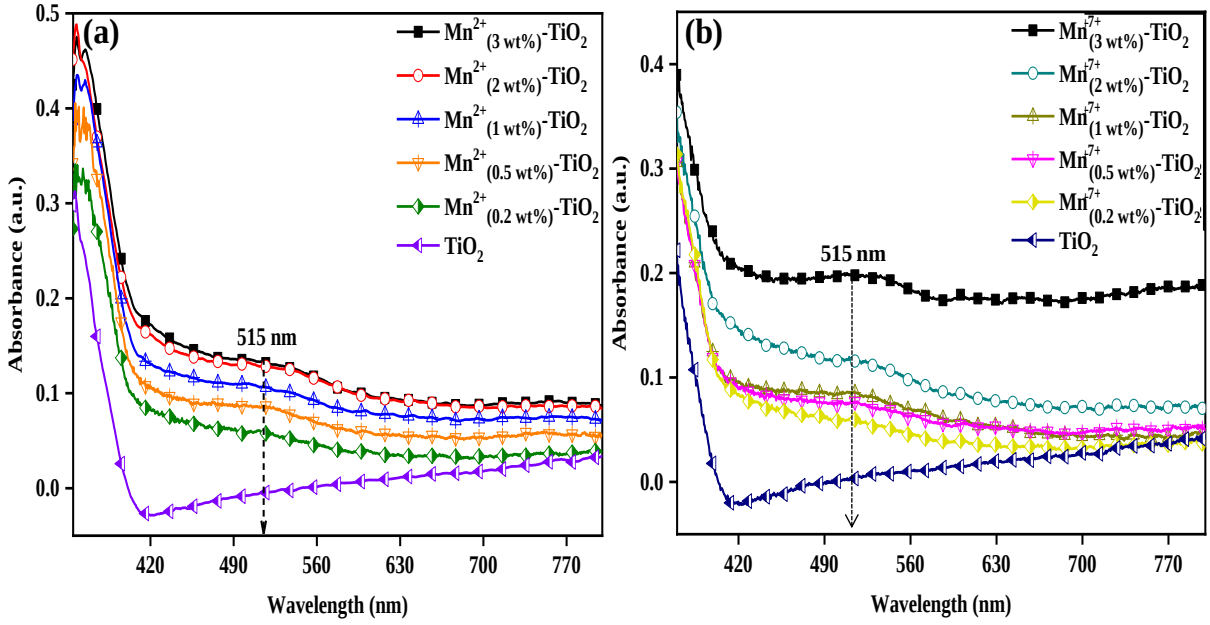

Figure 2.2. Diffuse reflectance spectra of different wt% of impregnated (a) Mn^{2+} and (b) Mn^{7+}-TiO_2 nanocatalysts

2.3.2. Surface structural and morphological properties

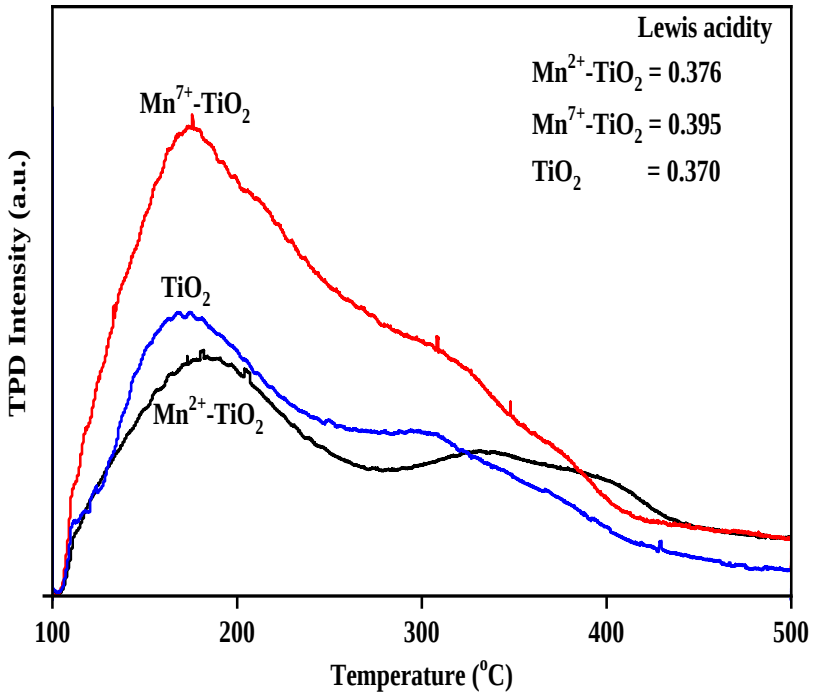

Figure 2.3. Temperature programmed desorption (TPD) of various Mn^{n+}-TiO_2 photocatalysts

TPD studies (fig. 2.3) using NH_3 gas to determine the surface acidity of various photocatalysts reveal an appreciable enhanced Lewis acidity prevailing on the Mn^{7+}-TiO_2 co-catalyst surface compared to bare and Mn^{2+} impregnated TiO_2. However, there was not much difference in peak area and height observed among Mn^{2+}-TiO_2 and bare TiO_2 photocatalyst at lower temperatures but an increased peak height was detected above 300 °C for Mn^{2+}-TiO_2 photocatalyst attributed to the migration of ammonia from sublattice sites to the catalyst surface [28]. It has also been established that Mn^{n+} ions offer enhanced NH_3 gas sensitivities to the TiO_2 surface in terms of selectivity and performance [29]. On the other hand, higher peak area and greater adsorption-desorption characteristics of Mn^{7+}-TiO_2 catalyst have been correlated to ease of combustion/redox capability of the co-catalyst. It has also been inferred that higher charge density per unit area possessed by Mn^{7+} ions impart a great deal of acidic character to TiO_2 surface compared to Mn^{2+} ions.

The HRTEM images of bare TiO_2 showed spherical morphological features having size ~ 20-40 nm (fig. 2.4a and 2.4b). On the other side, images for $Mn^{2+}_{(1\ wt\%)}$-TiO_2 (fig. 2.4c and 2.4d) and $Mn^{7+}_{(1\ wt\%)}$-TiO_2 (fig. 2.4e and 2.4f) nanocomposites disclosed mixed morphological characteristics. The dark colored islands of Mn metal oxides (MnO_x) deposited on the TiO_2 surface can be clearly seen due to higher electron density of Mn^{n+} than lighter Ti^{4+} species. As the Mn^{n+} cations cannot exist alone in the form of nanoparticles, therefore these have been considered to present in their corresponding metal oxides of different oxidation states. Based on our previous report, presence of Mn^{2+} species in the form of MnO/Mn_3O_4 and Mn^{7+} in the form of Mn_2O_7 NPs have been inferred. Further, it has been observed that most of the MnO_x NPs attained spherical shape while variable morphologies viz: cubical, triangular, rectangular and hexagonal have also been found out in both Mn^{n+}-TiO_2 nanocomposites.

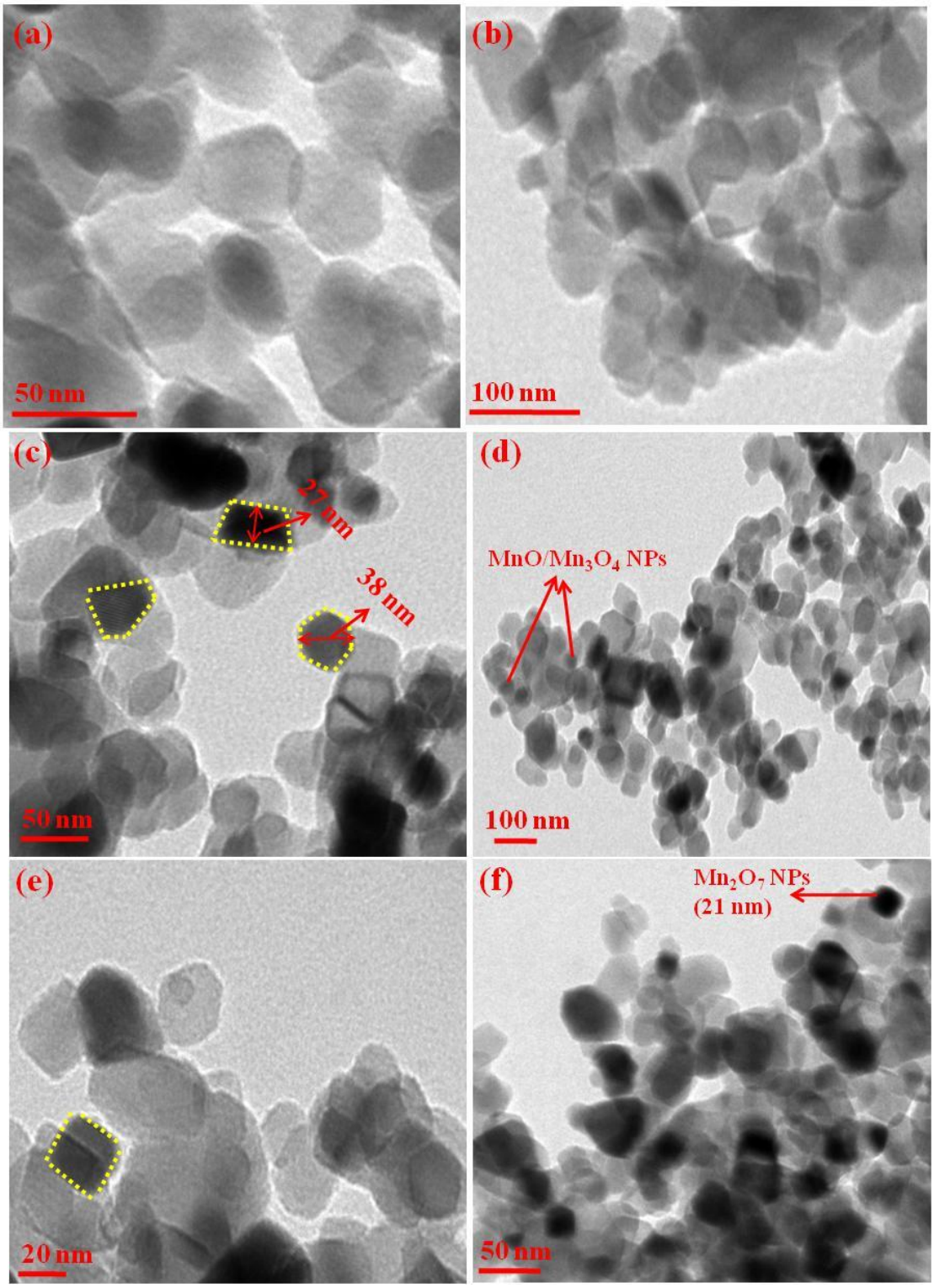

Figure 2.4. TEM images of bare TiO_2 (a, b), $Mn^{2+}_{(1\ wt\%)}$-TiO_2 (c, d) and $Mn^{7+}_{(1\ wt\%)}$-TiO_2 (e, f) nanocatalysts.

The size of impregnated Mn^{2+} and Mn^{7+} oxides/species have been measured in the range ~ 27-38 and ~ 20-35 nm, respectively which is not much differentiable yet different oxidation states and other dominating surface structural properties did affect the photo-oxidative process to a great extent. The EDS analysis showed the presence of Mn, Ti and O elements in Mn^{n+}-TiO_2 nanocatalysts. The K^+ ion present in the salt ($KMnO_4$) used to prepare the Mn^{7+}-TiO_2 catalyst was not detected (fig. 2.5). Since, K^+ act as a counter ion and is expected to get eliminated easily during the washing process. Therefore, its presence has not been revealed by EDS measurements. Based on the above observation, effect of only Mn^{7+} cations has been considered in the Mn^{7+}-TiO_2 catalyst.

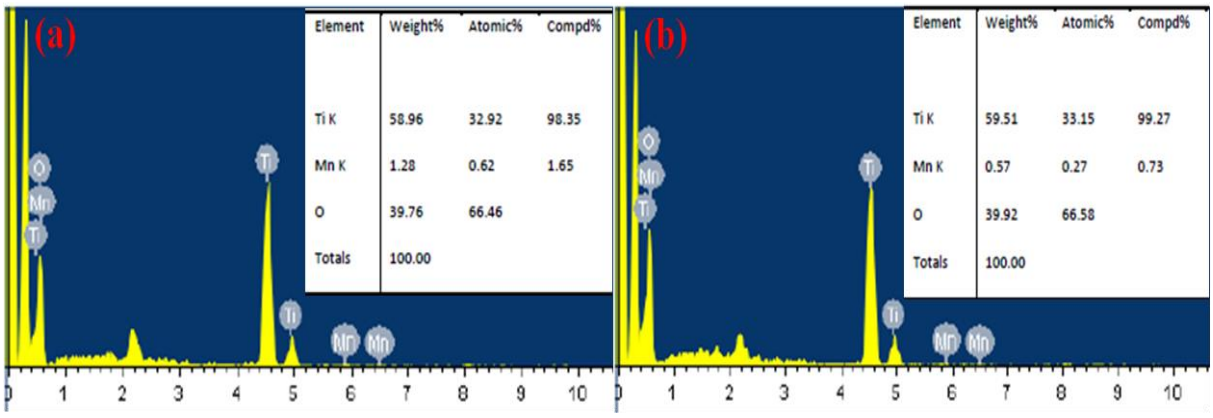

Figure 2.5. EDS analysis of (a) Mn^{2+} and (b) Mn^{7+} impregnated TiO_2 catalysts.

2.3.3. Crystallographic properties

Usually, P25 is considered to have two phases; anatase and rutile yet some studies report the presence of amorphous phase also. Based on these studies, the effect and content of these phases has been evaluated. For this, the pure anatase and rutile phases were extracted from P25 using H_2O_2-NH_3 mixture and aqueous HF solution, respectively [30-32]. Then, the XRD spectra of pure anatase, pure rutile, their 50 wt% mixture with NiO (internal standard) and P25 were analysed (fig. 2.6). The absolute content of anatase (72.5%), rutile (19.8%) and amorphous phase (7.7%) was then calculated by measuring the areas of high intensity peaks; 101 (anatase) and 110 (rutile) as shown in supporting information [33]. The detailed step by step calculations are discussed as below:

Calculations

The absolute crystallinity of anatase was calculated using the ratio between area of 101 peak of pure anatase and 200 peak of 50 wt% mixture of anatase with NiO as follows:

$$\frac{A\,(pure\ anatse),101}{A\,(mixture\ of\ NiO{+}anatse),200} = 0.62$$

Then, the anatase content of unknown (P25) was obtained as follows:

Absolute crystallinity of anatase = $\frac{1}{0.62} \times \frac{A\,(P25),101}{A\,(mixture\ of\ NiO{+}anatase),200} \times 100\%$

= 72.5%

The rutile content was estimated in a similar way:

$$\frac{A\,(pure\ rutile),110}{A(mixture\ of\ NiO + rutile),200} = 0.52$$

Absolute crystallinity of rutile = $\frac{1}{0.52} \times \frac{A\,(P25),110}{A\,(mixture\ of\ NiO{+}rutile),200} \times 100\%$

= 19.8%

Total amorphous content = 100 - (Anatase + Rutile)

= 100 - (72.5% + 19.8%)

= 100 - 92.3

= 7.7%

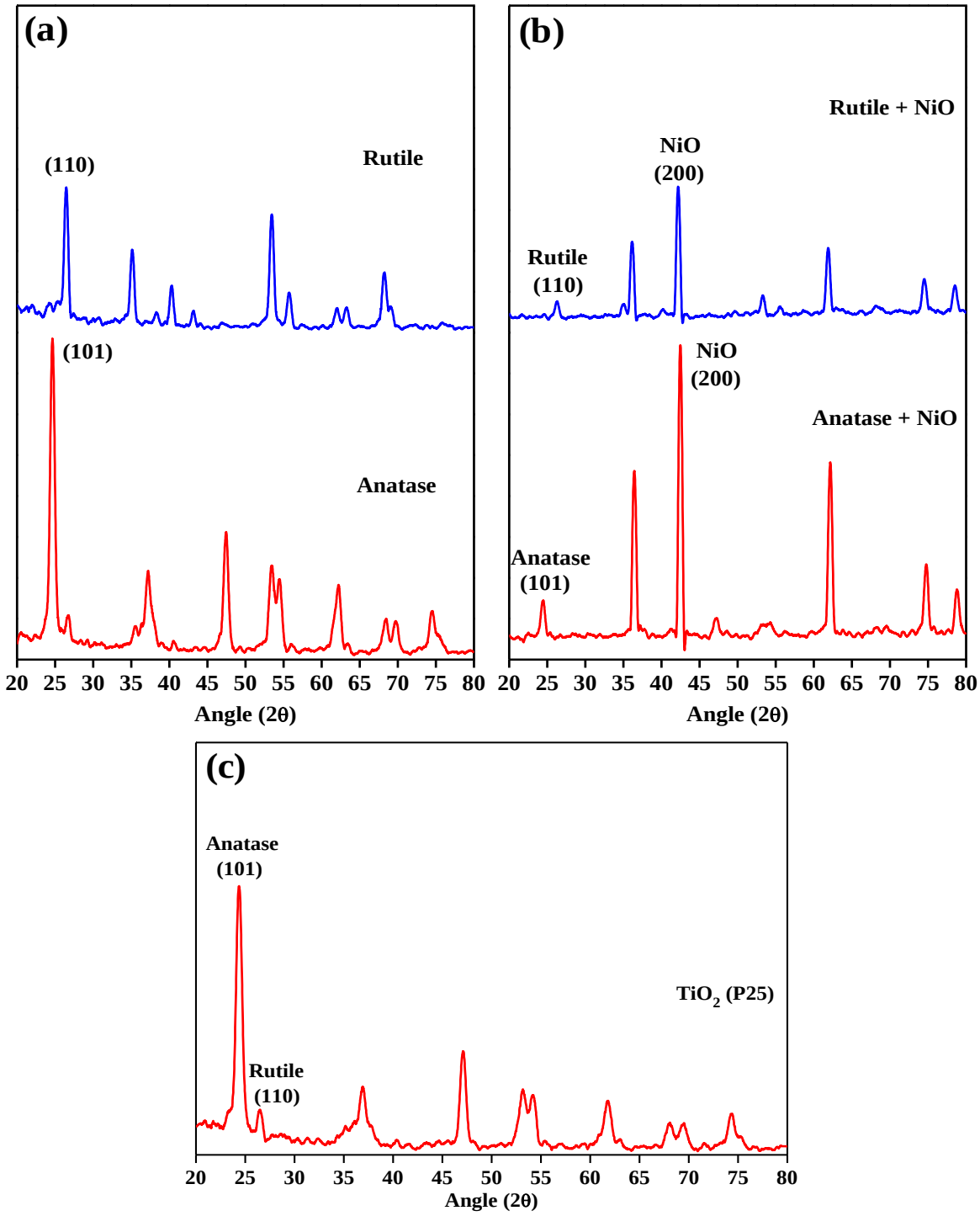

Figure 2.6. XRD spectra of (a) pure anatase and rutile, (b) anatase and rutile 50 wt% mixture with NiO and (c) P25.

To further study the presence of Mn^{n+} and crystallinity of different nanocatalysts, Raman analysis has been carried out (fig. 2.7). It is well known that TiO_2 exhibits a tetragonal crystal structure that belongs to the D_{4h}^{19} space group. There are six Raman active modes A_{1g}, $2B_{1g}$, $3E_g$ shown by anatase form of TiO_2. All these modes are observed at A_{1g} - 513 cm^{-1}, $2B_{1g}$ -

393, 513 cm^{-1} and 3Eg - 140, 193 and 635 cm^{-1} where peak at 513 cm^{-1} is the combination of two modes of vibration: $A_{1g} + B_{1g}$ [34].

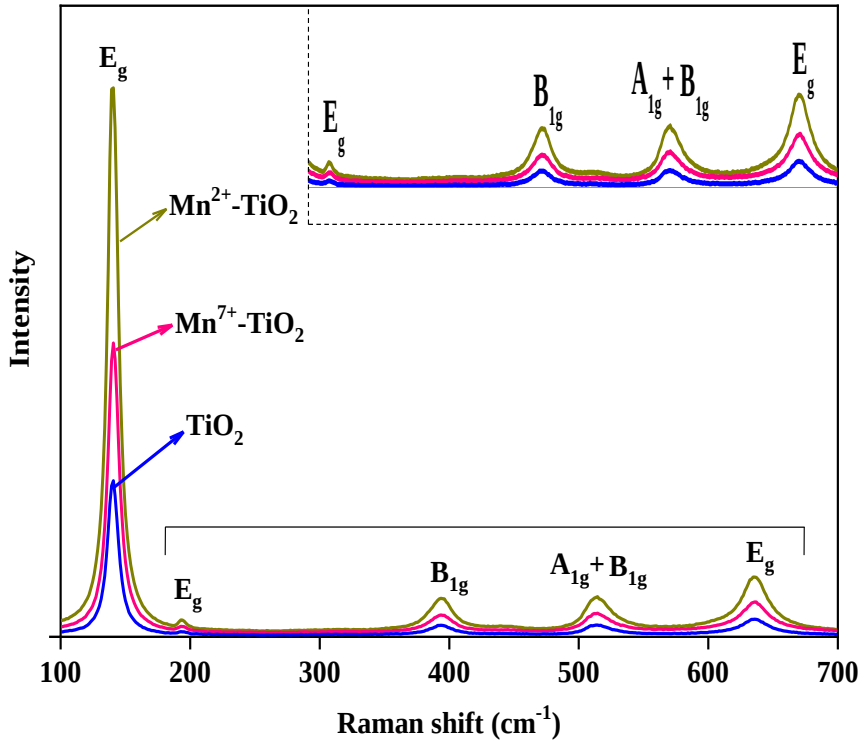

Figure 2.7. Raman spectra of bare and Mn^{n+} ions impregnated TiO_2 photocatalysts.

It has been analyzed that Mn^{n+} incorporation in the crystal lattice of TiO_2 leads to enhanced crystallinity than bare TiO_2. Further, one more interesting outcome has been noticed here that lower oxidation state of impregnated Mn^{n+} ion i.e. Mn^{2+} provided enhancement in crystal structure intensity compared to Mn^{7+} ion. Usually, enhanced Raman intensity is considered as a consequence of crystal distortion due to quantum confinement effect [35] which induces greater defects in the nanocrystalline system responsible for enhanced photocatalytic efficiencies.

SAXS analysis (fig. 2.8) has been done to know the overall shape and structural characteristics of different photocatalysts. There is a great difference found in the scattering pattern of only TiO_2 and Mn^{n+} incorporated TiO_2 co-catalysts. SAXS pattern of all catalysts showed scattering peak at scattering vector, q = 0.12 nm^{-1} characteristic of TiO_2 [36] that follows equation:

$$q = \frac{4\Pi}{\lambda} \sin(\frac{2\theta}{2})$$

where, q = scattering vector (nm^{-1}), 2q scattering angle (^{0}), λ = wavelength (nm) and d = Bragg spacing.

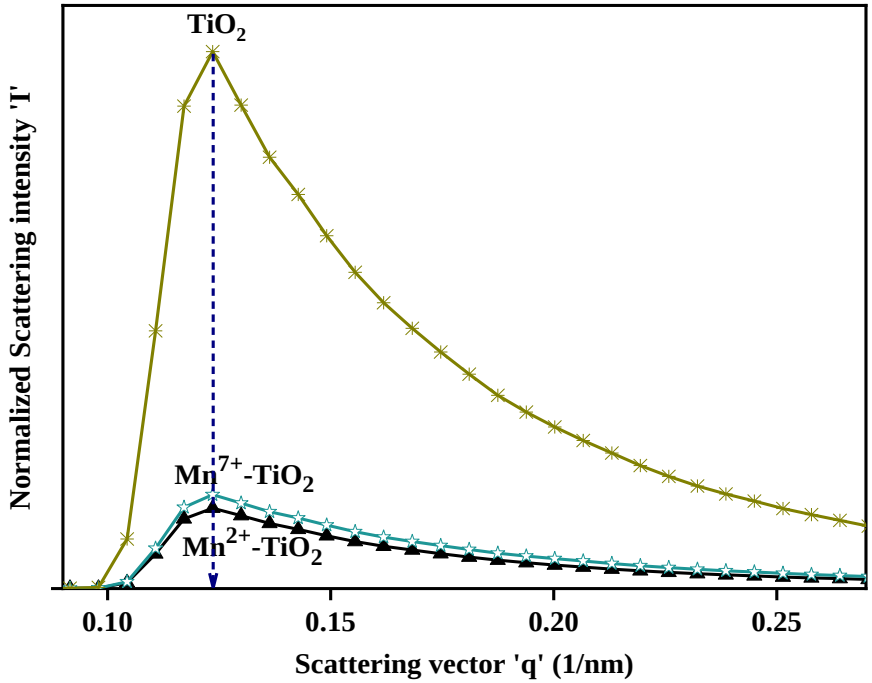

Figure 2.8. Small angle X-ray scattering (SAXS) behaviour of TiO_2 and Mn^{n+}-TiO_2 nanocomposites.

This peak suffered a hypochromic shift (decreased intensity) along with slighter broadening after the impregnation of Mn^{2+} and Mn^{7+} ions over TiO_2 surface without any usual peak shift. The scattering pattern is seen as an average of the form factor contribution (shape and intraparticle interferences) and structure factor (interaction with X-rays, interparticle distances and interferences). At small angles, sharp intensity as in bare TiO_2 depicts the attractive interactions between the particles as a consequence of aggregation. On the other hand, Mn^{2+}-TiO_2 and Mn^{7+}-TiO_2 co-catalysts showed decreased intensities due to the presence of repulsive interactions in their samples. Interestingly, a little higher peak intensity for Mn^{7+}-TiO_2 than Mn^{2+}-TiO_2 nanocatalyst can be due to greater interactions of highly positive oxidation state with the illuminated X-rays. It has been revealed that greater positive added over the surface of TiO_2 due to Mn^{n+} ions offer a great deal of photocatalyst stability due to the generation of repulsive interactions among nanoparticles.

The graph of pair distance distribution function (P(r)) and maximum average diameter of particles (D_{max}) is the indirect Fourier transform of intensity which determines the D_{max} and radii; r of the particles (fig. 2.9a).

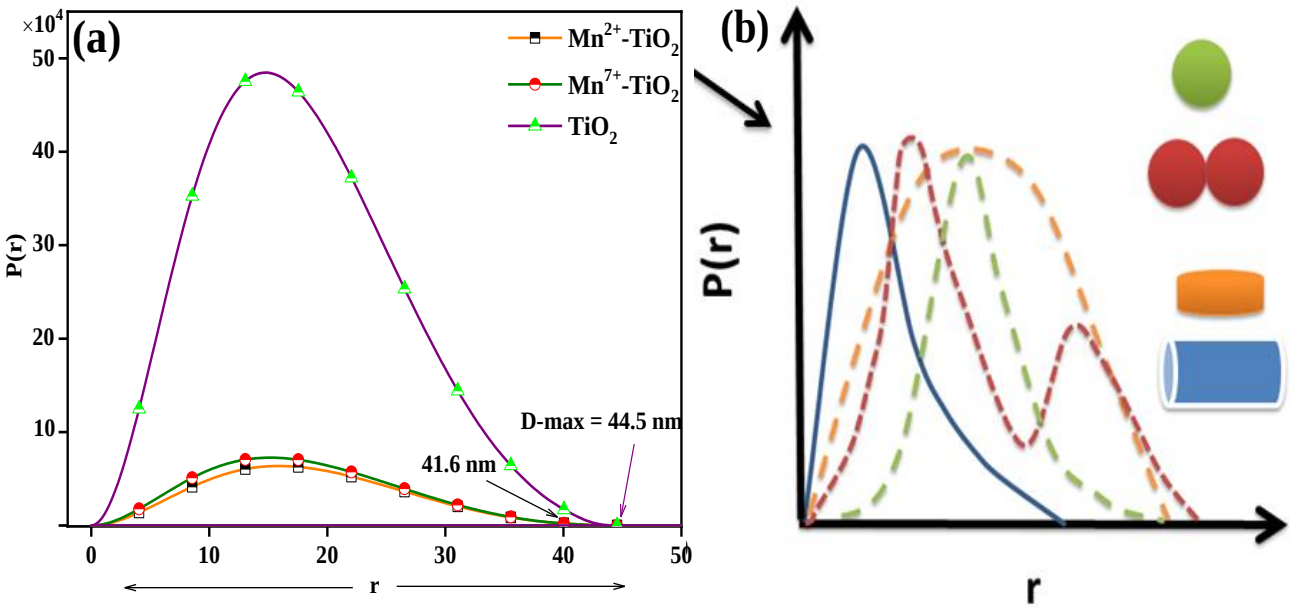

Figure 2.9. (a) Pair distance distribution function (P(r)) vs. D_{max} plot for different photocatalysts and (b) their reference pattern.

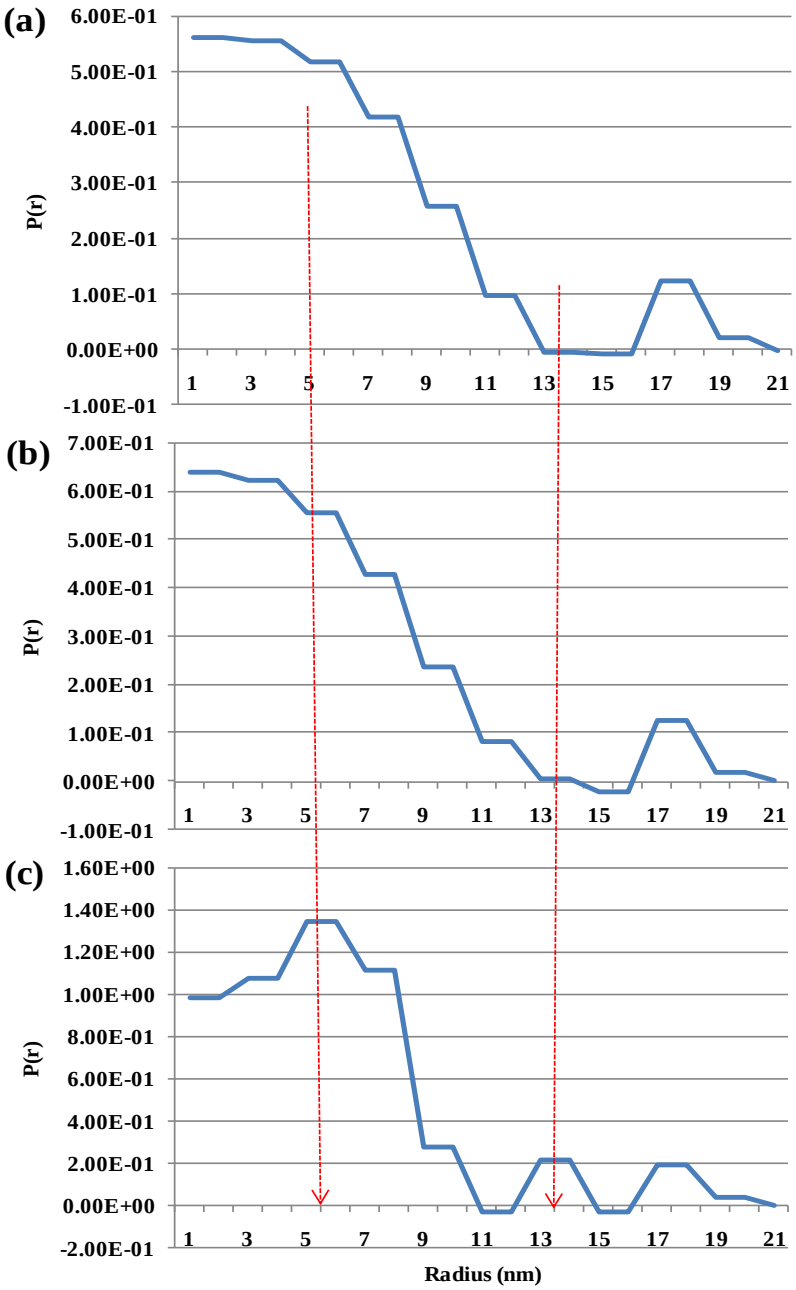

Figure 2.10. Electron density profile of (a) Mn^{2+}-TiO_2, (b) Mn^{7+}-TiO_2 and (c) bare TiO_2 photocatalysts.

The D_{max} value of 44.5 nm for bare TiO_2 and almost the same i.e. 41.6 nm for both Mn^{2+}/Mn^{7+}-TiO_2 co-catalysts was obtained. If we correlate the obtained P(r) plots with figure 2.9b, bare TiO_2 is considered to show the spherical and Mn^{2+} and Mn^{7+} impregnated co-catalysts showed both spherical or somewhat rectangular shaped characteristics due to little peak broadening. As can be clearly seen that rod-shaped nanocatalysts push the P(r) plot intensity towards lower D_{max} values while in the case of two joined spherical forms, a doublet will be obtained. Further, different radii range of nanocatalysts shown by electron density

profiles (EDP) comply with the diameter obtained (fig. 2.10). It was observed that two peaks at 5 and 13 nm in EDP of TiO_2 got completely disappeared with simultaneous generation of small peaks ranging between ~ 7-12 nm upon Mn^{2+} and Mn^{7+} impregnation. SAXS is caused by the difference in electron densities within and around the nanosize grains depicted in electron density profiles, hence different surface structural parameters derived are in accordance with the HRTEM analysis and P(r) plots.

To check the interparticle interferences and behavior of the scattering species, Guinier and Kratky plots had been drawn (fig. 2.11). The Mn^{2+}-TiO_2 and Mn^{7+}-TiO_2 photocatalysts exhibited a downturn (Frowning Guinier) while bare TiO_2 showed an upturn (Smiling Guinier) in Guinier plot. A smiling Guinier is referred as the aggregation property of nanoparticles which was detected by the SAXS pattern also. This type of behavior confirms that the presence of Mn^{n+} ions provides enhanced stability to the photocatalyst system which is further improved by an increase in the oxidation state of metal. In Kratky plots, all the nanocatalysts showed the scattering behavior of unfolded protein species [37]. However, it can be seen that the curve of Mn^{7+}-TiO_2 catalyst is much steeper than Mn^{2+}-TiO_2 and bare TiO_2 catalysts. This observation shows that the nanoparticles of Mn^{7+}-TiO_2 are more scattered/expanded and in a disordered state in the liquid medium. Based on the above findings, it has been inferred that the oxidation state of the impregnated metal ion plays a significant role which deciphers the surface structural, electrokinetic and morphological properties of the photocatalysts which further influence the adsorption and photocatalytic efficiencies.

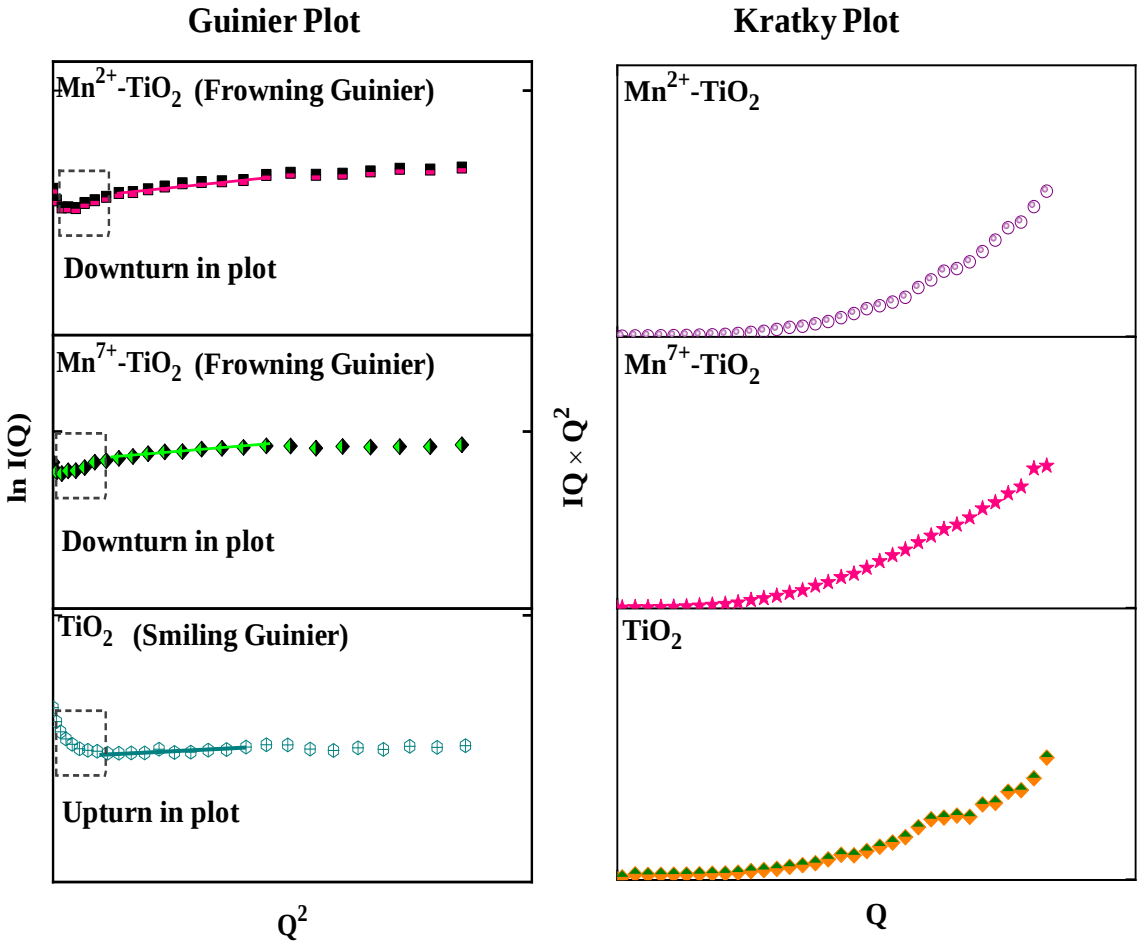

Figure 2.11. Guinier and kratky plots for different bare and Mn^{n+} impregnated TiO_2 co-catalysts.

2.3.4. Adsorption behaviour

The adsorption isotherms for various Mn^{n+}-TiO_2 co-catalysts were studied to evaluate their affinity towards the substrate (M.V.) to be degraded. The Langmuir isotherm (fig. 2.12) represents the formation of a monolayer on the surface of adsorbent (catalyst) and follows the following equation [38,39]:

$$q_e = \frac{q_{max} K_L C_e}{1 + K_L C_e}$$

where q_e is the conc of absorbate at equilibrium on the surface of catalyst (µg/mg), q_{max} is the maximum adsorption capacity of the adsorbent up to complete monolayer coverage (µg/mg), C_e is the concentration of adsorbate at equilibrium (mg/mL) and K_L is the Langmuir constant (mL/mg). The linear form of equation can be shown as:

$$\frac{1}{q_e} = \frac{1}{q_{max} K_L C_e} + \frac{1}{q_{max}}$$

The intercept and slope obtained from the linear graph between $1/q_e$ vs. $1/C_e$ were used to calculate the equilibrium constants (q_{max} and K_L) and have been mentioned in Table 2.1. The measured q_{max} and K_L values indicate a significant adsorption capacity of Mn^{7+}-TiO_2 compared to Mn^{2+}-TiO_2 and bare TiO_2 nanocatalyst. On the other hand, Freundlich isotherm describes multilayer adsorption on the surface of the catalyst following equation:

$$q_e = K_f C_e^{\frac{1}{n}}$$

or logarithmic form of equation can be represented as:

$$\ln q_e = \ln K_f + \frac{1}{n} \ln C_e$$

where q_e is the conc of adsorbate (μg/mg) on catalyst surface at equilibrium, C_e is the conc of adsorbate at equilibrium (mg/mL), K_f is the Freundlich constant (μg/mg)$(mL/mg)^{1/n}$ and 1/n is the heterogeneity factor. The linear graph was obtained between ln q_e vs. ln C_e as shown in figure 2.12b . The K_f and exponent 1/n values have been calculated from the intercept and slope of the graph, respectively (Table 2.1). The 1/n values between 0 to 1 and n > 1 denote favorable adsorption behavior. Thus, isotherm graphs and results obtained depict that the adsorption equilibria data best fit for the Freundlich isotherm and suggest a uniform and multilayer type of adsorption. The greater interionic interactions possessed by Mn^{7+}-TiO_2 co-catalyst for cationic Methyl viologen are contrary to expected cation-cation repulsions. This type of adsorption behavior has been credited to cation-Π interactions between Mn^{7+} cation and Π electron cloud of M.V [40]. It has been established that this type of interactions stabilize the charge redistribution which accelerates the reaction rates by controlling the photochemical transformations. It was also considered that higher oxidation state induces greater polarity on the co-catalyst surface causing enhanced catalyst-substrate associations.

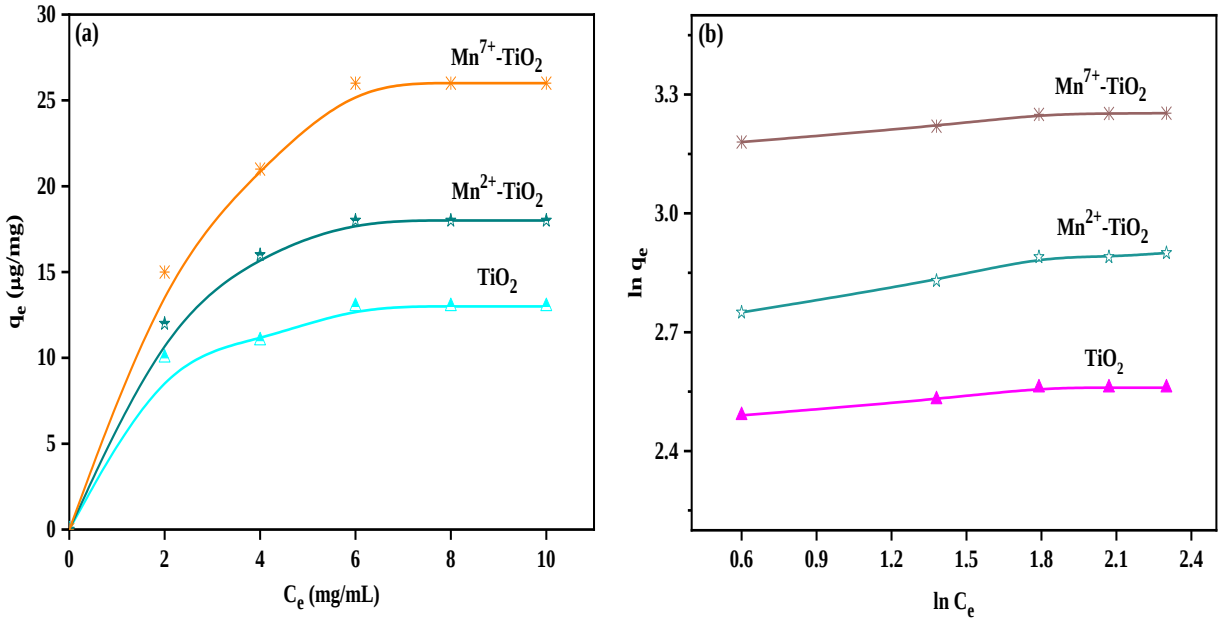

Figure 2.12. The langmuir (a) and freundlich (b) adsorption isotherm fit by bare TiO_2 and Mn^{n+}-TiO_2 nanocomposites for methyl viologen.

Table 2.1. Langmuir and freundlich adsorption parameters obtained for different Mn^{n+} impregnated and bare TiO_2 photocatalysts.

Sr. No.	Catalysts	Langmuir isotherm			Freundlich isotherm		
		q_{max} (µg/mg)	$K_L \times 10^{-1}$ (mL/mg)	R^2	1/n	K_f (µg/mg)	R^2
1.	TiO_2 (P25)	4.571	2.37	0.55	0.044	11.74	0.90
2.	Mn^{2+}-TiO_2	5.809	2.70	0.60	0.092	14.85	0.93
3.	Mn^{7+}-TiO_2	7	3.42	0.70	0.046	23.44	0.92

2.3.5. Photocatalytic activity

The photocatalytic activity of bare and Mn^{n+} impregnated TiO_2 nanocomposites in terms of photooxidative degradation of carcinogenic pollutant Methyl viologen was evaluated under safer and natural solar irradiation. Firstly, the loading wt% (0.2, 0.5, 1, 2 and 3) of Mn^{n+} ions in Mn^{2+}/Mn^{7+}-TiO_2 nanocatalysts (Mn^{2+} and Mn^{7+}) was optimized for better outcomes. Figure 2.13a and 2.13b represent that initially, as the wt% of Mn^{n+} deposition was increased from 0.2 to 1%, the degradation rate continued to become faster and afterward decreased up to 3 wt% under solar intensity of 52.5 mW/cm^2. Up to 1 wt% loading, the enhanced activity is attributed to more growth and deposition of Mn NPs which generate greater surface plasmon resonance (SPR) effect. Further loading lead to layer by layer coverage of entire support surface which tends to widen up the bandgap as illustrated by Burstein-Moss effect [41]. At high wt%, the formation of a complete layer of Mn^{n+} over the TiO_2 surface leads to decreased photonic absorption or light penetration which hinders Mn^{n+}-TiO_2 photoactivity.

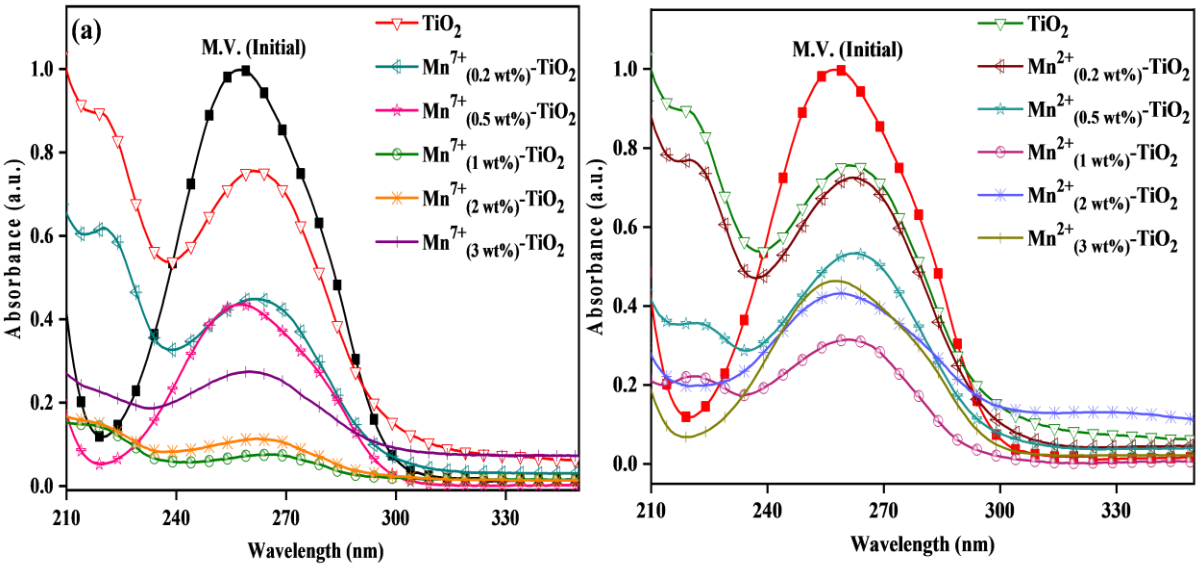

Figure 2.13. Optimization of Mn^{2+} and Mn^{7+} ions wt% over TiO_2 for the photodegradation of M.V. under solar light irradiation.

The effect of calcination temperature (400, 500 and 600°C) of Mn^{n+}-TiO_2 nanocomposites was also determined. Figure 2.14a and 2.14b describe the photoactivity of Mn^{2+}/Mn^{7+}-TiO_2 nanocatalysts prepared at different calcination temperatures at a sunlight intensity of 53.0 mW/cm^2. In this concern, the maximum activity of both catalysts (Mn^{2+}-TiO_2 and Mn^{7+}-TiO_2) was detected at 500°C with 67 and 93% degradation efficiency which lessened further at 600°C but was still higher than 400°C as represented in fig. 2.14c. The higher photocatalytic activity by 1 wt% Mn^{n+} loading calcined at a temperature of 500°C was

credited to the cumulative effect of many factors such as optimized surface plasmons, appropriate pore volume, islands of mixed morphologies of Mn^{n+} over TiO_2 and highly charged Mn^{n+} ion-induced polarity onto co-catalyst surface.

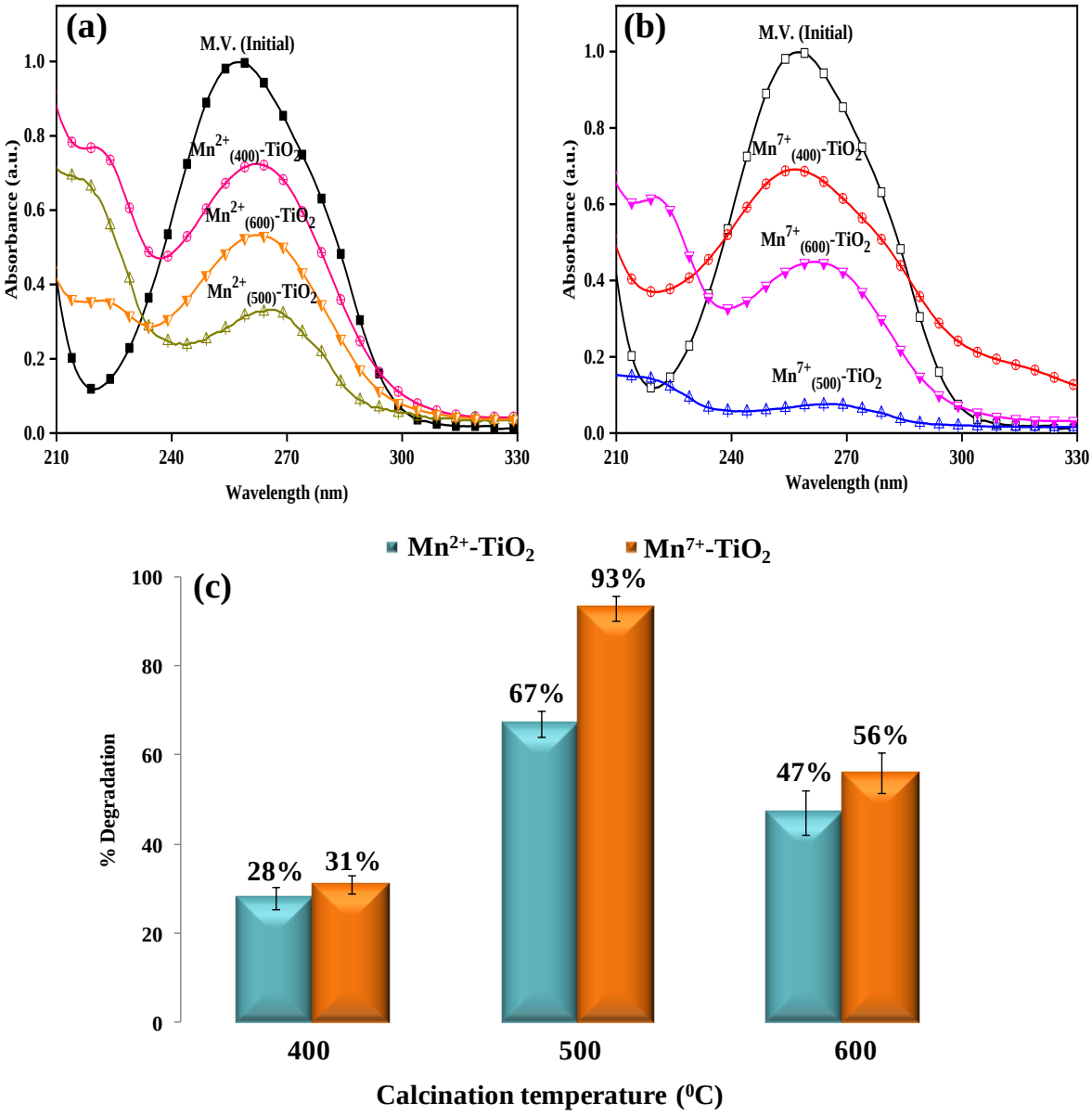

Figure 2.14. Optimization of calcination temperature of (a) Mn^{2+}-TiO_2 and (b) Mn^{7+}-TiO_2 nanocatalysts and (c) corresponding % degradation under solar irradiation.

The final photodegradation of M.V. was measured for 5 h duration under solar irradiation (53.6 mW/cm^2) between 11 a.m to 4 p.m. As demonstrated by figure 2.15a, it was observed that the Mn^{n+} incorporated TiO_2 co-catalysts showed higher activity than bare TiO_2 photocatalyst which further enhanced upon increase in oxidation state of Mn^{n+} ion from 2 to 7. The photooxidative degradation efficacy of Mn^{7+}-TiO_2 was estimated to be 93% which is much appreciable compared to 67 and 25% by Mn^{2+}-TiO_2 and bare TiO_2 photocatalyst,

respectively. This observation has been correlated to enhanced catalyst-substrate interionic interactions and adsorption capacity offered by the particles of Mn^{7+}-TiO_2 nanocatalyst for herbicide; M.V. molecules.

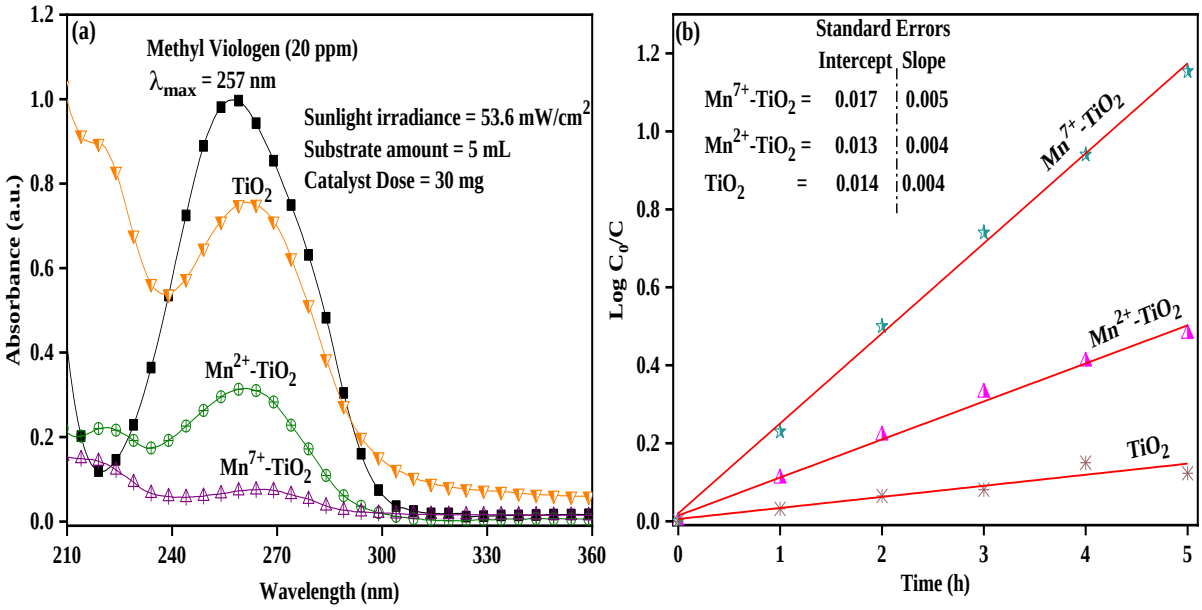

Figure 2.15. (a) Co-catalytic degradation of M.V. using Mn^{n+}-TiO_2 and bare TiO_2 nanocatalysts for 5 h under sunlight irradiation and (b) reaction kinetics study.

Further, the time course and reaction kinetics were studied using the equation:

$$k = \frac{2.303}{t} \log \frac{C_0}{C}$$

The linear form of this equation can be represented as:

$$\log \frac{C_0}{C} = \frac{kt}{2.303}$$

where k is the reaction rate constant (h^{-1}), t is the time (h), C_0 and C are initial and final concentrations of substrate molecules. The graph between $\log C_0/C$ vs. time was a straight line passing from the origin (fig. 2.15b) and is considered to follow pseudo first-order kinetics because of the heterogeneous nature of photocatalysts and very low conc. of substrate involved. The rate constant, k values determined from the slope and correlation coefficients (R^2) have been mentioned in Table 2.2 and have been found to be in good agreement with the observed photodegradation process.

Table 2.2. The pseudo first order reaction parameters shown by different nanocatalysts for the photodegradation of M.V.

Sr. No.	Catalysts	Absorbance after photoactivity	Slope (k/2.303)	$k \times 10^{-2}$ (h^{-1})	R^2
1.	TiO_2 (P25)	0.75	0.024	5.527	0.95
2.	Mn^{2+}-TiO_2	0.33	0.095	21.879	0.98
3.	Mn^{7+}-TiO_2	0.07	0.229	52.739	0.99

In this photocatalytic process, Mn^{7+} ions have been proven to impart greater co-catalytic effect due to enhanced co-catalyst surface electron affinity resulting in stronger catalyst-substrate associations. Also, the Mn^{n+} ions help to sensitize visible light more efficiently as the oxidation state increases. Under solar irradiation, these charged ionic species underwent continuous electronic oscillations. The excited electrons generated are then transferred to the C.B. of TiO_2 and get utilized for reduction process depending on the reaction conditions [42]. Here, in the Mn^{7+}-TiO_2 catalyst, the electron transfer phenomena occurs from O^{2-} to Mn^{7+} species, therefore reduction is considered to take place at Mn^{7+} co-catalyst surface (scheme 2.1).

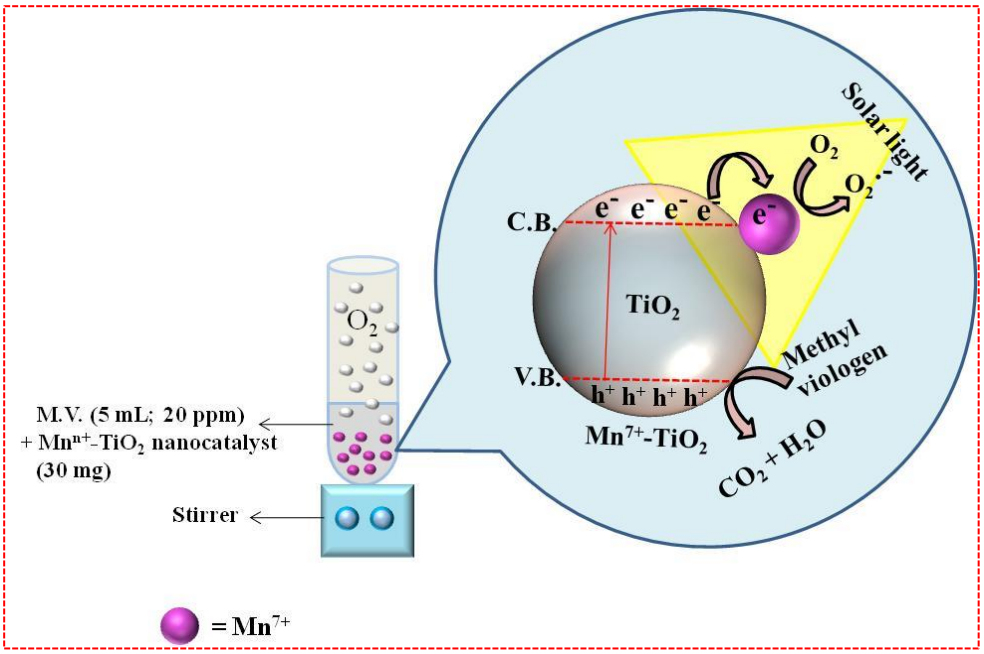

Scheme 2.1. Mn^{n+} induced co-catalysis route followed by Mn^{n+}-TiO_2 nanocomposites for the degradation of methyl viologen under solar irradiation.

Due to stronger electron affinity of Mn^{7+} ions, the e^--h^+ pair recombination rate in the TiO_2 is appreciably decreased. The Mn^{7+} ions in the Mn^{7+}-TiO_2 catalyst surface bring the substrate molecules closer which are then photochemically oxidised by holes present on the TiO_2 surface. Thus, it has been concluded that apart from other factors such as crystal structure, optical spectra and different nature of metals; the oxidation state, nature of substrate and catalyst-substrate associations are also important parameters affecting a photocatalytic process.

References

[1] S. Higashimoto, R. Shirai, Y. Osano, M. Azuma, H. Ohue, Y. Sakata, H. Kobayashi, J. Catal. 311 (2014) 137-143.

[2] W. Ge, Y. Chen, L. Wang, R. Zhang, Univers. J. Chem. 3 (2015) 104-111.

[3] H. Kyung, J. Lee, W. Choi, Environ. Sci. Technol. 39 (2005) 2376-2382.

[4] N. Smirnova, V. Vorobets, O. Linnik, E. Manuilov, G. Kolbasov, A. Eremenko, Surf. Interface Anal. 42 (2010) 1205-1208.

[5] V. Polliotto, S. Livraghi, A. Krukowska, M.V. Dozzi, A. Zaleska-Medynska, E. Selli, E. Giamello, ACS Appl. Mater. Interfaces 10 (2018) 27745-27756.

[6] X.Z. Li, F.B. Li, Environ. Sci. Technol. 35 (2001) 2381-2387.

[7] Z. Zhang, J.T. Yates, Jr, Chem. Rev. 112 (2012) 5520-5551.

[8] M.-K. Jeon, M.-K. Yeo, H.-J. Choi, J. Kim, S.-J. Choung, J.-B. Kim, D. Jeong, M. Kang, J. Ind. Eng. Chem. 13 (2007) 827-834.

[9] S.K. Cushing, J. Li, J. Bright, B.T. Yost, P. Zheng, A.D. Bristow, N. Wu, J. Phys. Chem. C 119 (2015) 16239-16244.

[10] L.G. Devi, R. Kavitha, Appl. Surf. Sci. 360 (2016) 601-622.

[11] L. Michalas, A. Khiat, S. Stathopoulos, T. Prodromakis, J. Phys. D Appl. Phys. 51.42 (2018) 425101.

[12] L. Wang, T. Egerton, J. Mater. Sci. Res. 1 (2012) 19.

[13] S. Ahadi, N.S. Moalej, S. Sheibani, Solid State Sci. 96 (2019) 105975.

[14] J. V. Hernandez, S. Coste, A.G. Murillo, F.C. Romo, A. Kassiba, J. Alloys Compd. 710 (2017) 355-363.

[15] N. Gupta, B. Pal, J. Mol. Catal. A Chem. 371 (2013) 48-55.

[16] A. Manikandan, J.J. Vijaya, L.J. Kennedy, Physica E: Low-Dimensional Systems and Nanostructures 49 (2013) 117-123.

[17] A.M. Jacintha, A. Manikandan, K. Chinnaraj, S.A. Antony, P. Neeraja, J. Nanosci. Nanotechno. 15 (2015) 9732-9740.
[18] E. Hema, A. Manikandan, P. Karthika, M. Durka, S.A. Antony, B.R. Venkatraman, J. Nanosci. Nanotechno. 16 (2016) 7325-7336.
[19] Z. Xiufeng, L. Juan, L. Lianghai, W. Zuoshan, J. Nanomater. 2011 (2011) 47.
[20] D. Zhao, C. Chen, Y. Wang, W. Ma, J. Zhao, T. Rajh, L. Zang, Environ. Sci. Technol. 42 (2008) 308-314.
[21] B. Pal, R. Kaur, I.S. Grover, J. Ind. Eng. Chem. 33 (2016) 178-184.
[22] J. Choi, H. Park, M.R. Hoffmann, J. Phys. Chem. C 114 (2010) 783-792.
[23] S.-M. Chang, W.-S. Liu, Appl. Catal. B-Environ. 156-157 (2014) 466-475.
[24] P. Nuhant, M.S. Oderinde, J. Genovino, A. Juneau, Y. Gagne, C. Allais, G.M. Chinigo, C. Choi, N.W. Sach, L. Bernier, Y.M. Fobian, M.W. Bundesmann, B. Khunte, M. Frenette, O.O. Fadeyi, Angew. Chem. Int. Ed. 56 (2017) 15309-15313.
[25] S. Bhardwaj, B. Pal, J. Alloy Compd. 816 (2020) 152639.
[26] S. Bhardwaj, B. Pal, Adv. Powder Technol. 29 (2018) 2119-2128.
[27] S. Paul, A. Choudhury, Int. J. Innov. Res. Dev. 1 (2012) 24-31.
[28] P. Doggali, Y. Teraoka, P. Mungse, I.K. Shah, S. Rayalu, N. Labhsetwar, J. Mol. Catal. A-Chem. 358 (2012) 23-30.
[29] Z.P. Tshabalala, K. Shingange, F.R. Cummings, O.M. Ntwaeaborwa, G.H. Mhlongo, D.E. Motaung, J. Colloid Interface Sci. 504 (2017) 371-386.
[30] B. Ohtani, Y. Azuma, D. Li, T. Ihara, R. Abe, Trans. Mater. Res. Soc. Japan 32[2] (2007) 401-404.
[31] T. Ohno, K. Sarukawa, M. Matsumura, J. Phys. Chem. B 105 (2001) 2417-2420.
[32] B. Ohtani, O.O. Prieto-Mahaney, D. Li, R. Abe, J. Photochem. Photobiol. A: Chem. 216 (2010) 179-182.
[33] M. Bellardita, A.D. Paola, B. Megna, L. Palmisano, J. Photochem. Photobiol. A: Chem. 367 (2018) 312-320.
[34] K. Gopinath, S. Kumaraguru, K. Bhakyaraj, S. Thirumal, A. Arumugam, Superlattice Microst. 92 (2016) 100-110.
[35] P.R. Ettireddy, N. Ettireddy, S. Mamedov, P. Boolchand, P.G. Smirniotis, Appl. Catal. B-Environ. 76 (2007) 123-134.
[36] B. Liu, M. Louis, L. Jin, G. Li, J. He, Chem. Eur. J. 24 (2018) 9651-9657.
[37] A.G. Kikhney, D.I. Svergun, FEBS Lett. 589 (2015) 2570-2577.

[38] A.O. Dada, A.P. Olalekan, A.M. Olatunya, O. Dada, IOSR J. Appl. Chem. 3 (2012) 38-45.

[39] B.H. Hameed, A.A. Ahmad, N. Aziz, Chem. Eng. J. 133 (2007) 195-203.

[40] C.R. Kennedy, S. Lin, E.N. Jacobsen, Angew. Chem. Int. Ed. Engl. 55 (2016) 12596-12624.

[41] S. Munir, S.M. Shah, H. Hussain, R.A. Khan, Mater. Des. 92 (2016) 64-72.

[42] M. Janczarek, E. Kowalska, Catalysts 7 (2017) 317.

Chapter 3

Improved charge carrier dynamics and catalyst substrate associations as a consequence of different oxidation states of Cr^{n+}-TiO_2 nanocomposites

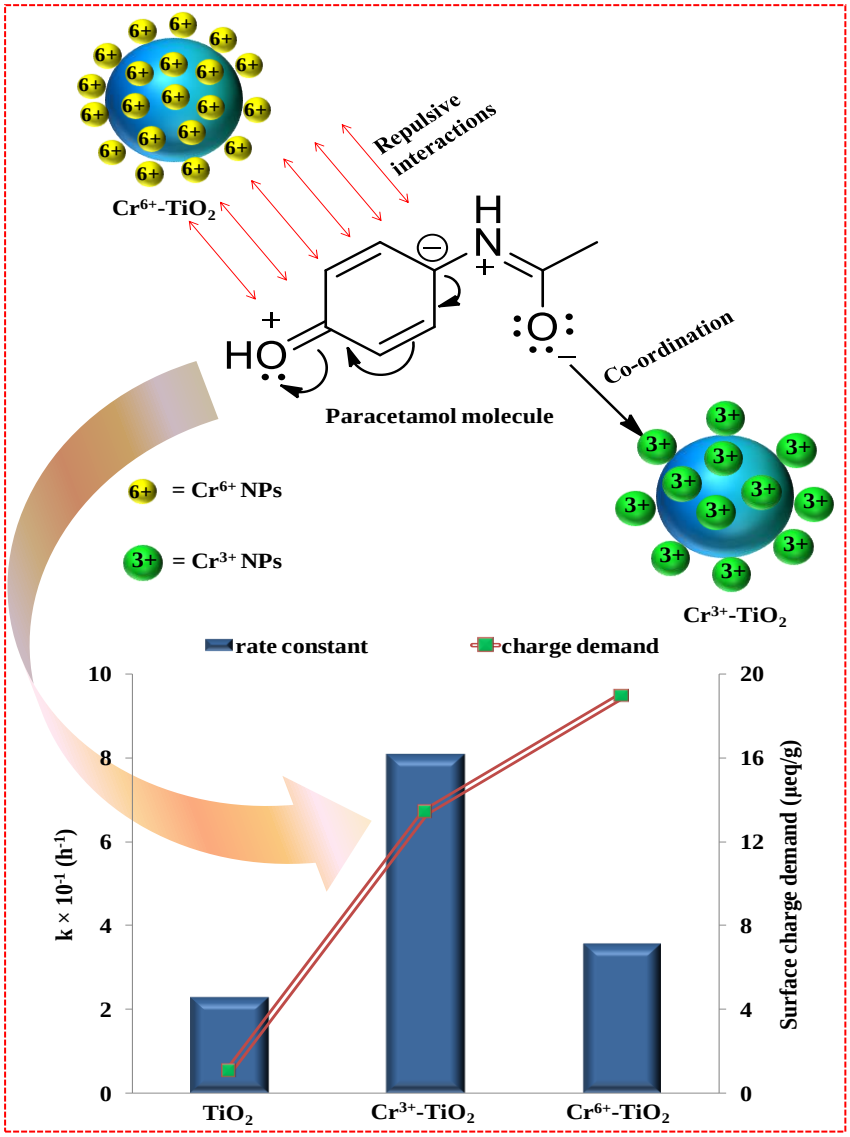

Summary

This chapter summarizes the interaction assisted photocatalytic degradation of paracetamol and aspirin molecules using different Cr^{n+}-TiO_2 nanocomposites under solar irradiation. For aspirin, Cr^{6+}-TiO_2 with rate constant, k = 18.815 × 10^{-3} min^{-1} while for paracetamol, Cr^{3+}-TiO_2 catalyst with k = 8.052 × 10^{-1} h^{-1} showed maximum activity. The Cr^{n+} loadings on the surface of TiO_2 catalyst have also been found to provide improved optical responses and enhanced charge carrier dynamics too.

3.1. Introduction

There has been a great research going on since the last few decades concerning the synthesis of promising photocatalysts which can be exploited in the direction of energy and environment fields. In this concern, semiconductor materials such as TiO_2, Bi_2O_3 and SiO_2 etc. have been studied a lot [1-5]. Among these, TiO_2 is considered to be the best candidate due to its safer use, photoactivity and easy modifiable nature. It has been modified using different means by varying the shape, size and incorporating metals/non-metals on its surface [6-8]. Various plasmonic metals such as Cu, Ag and Au are proven efficient to further improve the e^--h^+ recombination rates and photo response of the TiO_2 nanocatalyst towards visible regions [9,10]. These metals are usually photo deposited in reduced forms onto the surface of TiO_2 due to their suitable redox potential values (Cu = 0.337, Ag = 0.799 and Au = 1 eV). On the other hand, their oxidised forms are also shown to have greater photocatalytic activities due to change in the work function of the cation oxidation states. For example, Ag(I)/TiO_2 has been found to show much higher photocatalytic activity for the oxidation of methyl blue than Ag(0)/TiO_2 catalyst due to the formation of active sites on catalyst surface [11]. The Au^{3+}-TiO_2 photocatalysts are considered to act as electron and hole trappers as compared to the Au^{1+}-TiO_2 catalysts showing better activities for waste water treatment purposes [12]. The doping of Fe creates oxygen vacancies and enhance the generation of more hydroxyl radicals over TiO_2 surface [13]. Therefore, Fe^{3+} ions impregnated TiO_2 catalysts have been found to show appreciable degradations for carbendazim and propiconazole under solar irradiation [14]. The interaction and sensing property of TiO_2 with the metal ions i.e. Pb^{2+}, Zn^{2+} and Cu^{2+} has been applied for the removal of waste water pollutants as well [15]. In another work, Cd^{2+}, Ba^{2+}, Cu^{2+}, Sn^{2+}, Pd^{2+}, NH_4^+, Na^+, K^+, Fe^{2+}, Mn^{2+} and Fe^{3+} ions have been detected for selective and preferential adsorption with the Bi_2S_3-TiO_2 nanoparticles [16]. Among these, Fe^{3+} ions are found to get selectively adsorbed mainly due to the TiO_2 photocatalyst.

Further, chromium doped nanocomposites have been established to play an important role for the removal of waste water malachite green dye [17]. The Cr/TiO_2 microspheres have been revealed to appreciably lower the activation energy for the photooxidation of chlorobenzene [18]. These catalysts possessed higher oxidation states of chromium (Cr^{5+} and Cr^{6+}) and imparted highest oxidizing abilities. The effective photooxidation of iodide to iodine by different metal ions impregnated TiO_2 catalysts has been correlated to different oxidation states and ionic radii of metal ions [19]. Different nature, work function, lewis acidity and

charge/volume ratios of metal ions depict the photocatalysis behaviour. If oxidation state of loaded metal will be higher, there will be greater electron affinity, surface charge density, lower ionic radii which could penetrate the crystal lattice of the support and thus higher adsorption and oxidation will result. Based on this, our previous work demonstrated that Mn metal ions (Mn^{2+} and Mn^{7+}) interact with cationic/anionic substrate molecules based on their PZC, electrokinetic and charge demand parameters [20]. Another study suggests that the reaction rates tend to grow continuously with increased valence state of chromium species [21]. The substrate adsorbs on the surface acidic sites provided by the high oxidation state of chromium which further act as active centres for the CH_2Cl_2 decomposition [22]. It is noteworthy that high oxidation state plays an important role in the growing reaction rates [23].

In this concern, the present work aims at studying the influence of different oxidation states of chromium (Cr^{3+}/Cr^{6+}) on the optical, electrokinetic, charge carrier and photocatalytic properties of Cr^{n+}-TiO_2 nanocomposites. These catalysts have been prepared using a simple wet impregnation technique and further investigated for the degradation of aspirin and paracetamol drugs under natural solar irradiation. The water pollution originating from the pharmaceutical industries leads to an overdose (aspirin > 150 mg/kg and paracetamol > 75 mg/kg) of these drugs amongst humans and animals posing serious life threatening results. In order to eradicate the harmful side effects such as tinnitus, vomiting, double vision and hepatic-toxicity caused by the drug poisoning, we have photo degraded these drugs in the commercially available forms in the market using the prepared catalysts under natural solar light irradiation.

3.2. Experimental details

3.2.1. Chemicals and reagents

Commercially available form of TiO_2 (P25; 70% Anatase + 30% Rutile phase) was received as a gift from Degussa corporation, Germany. Chromium nitrate ($Cr(NO_3)_3 .9H_2O$; 98 %) and potassium dichromate ($K_2Cr_2O_7$; 99.5 %) both were purchased from Loba Chemie, India. Further, the aspirin (Ecosprin; 75 mg by USV PVT Limited) and paracetamol (Crocin; 500 mg by GSK Consumer Healthcare India) were used as drugs available in the market. Distilled water (DI) was obtained from an ultrafiltration system (Milli-Q, Millipore) with measured conductivity of 35 mho cm^{-1} at 25 °C.

3.2.2. Synthesis of Cr^{n+}-TiO_2 nanocomposites

The synthesis of Cr^{n+}-TiO_2 nanocomposites was achieved by wet impregnation method [24]. For this, 100 mg of the TiO_2 (P25) catalyst was dispersed in 10 mL of distilled water. Then, the required amount (1 wt%) of chromium salt solutions (0.01 M; $Cr(NO_3)_3$. $9H_2O$ for Cr^{3+} and $K_2Cr_2O_7$ for Cr^{6+} impregnation) were introduced drop wise into the TiO_2 solution. The above solutions were continuously stirred for 48 h and centrifuged (5000 rpm; 5 min). The prepared catalysts were washed repeatedly five times with water and ethanol and then dried at 100 °C.

3.2.3. Characterization techniques

The various characterizations were performed by techniques as mentioned in chapter 1 (section 1.5).

3.2.4. Adsorption and photocatalytic activity

The aspirin (ASP) and paracetamol (PCM) solutions (20 ppm; 5 mL each) were treated with 20 mg of the synthesized catalysts separately in different test tubes with continuous stirrings. These solutions were kept for a duration of 8 h under dark conditions to achieve the adsorption-desorption equilibria. Then, the catalysts were separated by centrifugation and the spectra of the respective solutions were recorded in UV-visible spectrophotometer at λ_{max} of 226 and 244 nm for aspirin and paracetamol, respectively. Further, the photocatalytic activity was determined in a similar way as that of the adsorption but keeping the reaction test tubes in the oxygenated atmosphere under solar irradiation.

3.3. Results and Discussion

3.3.1. Optical properties

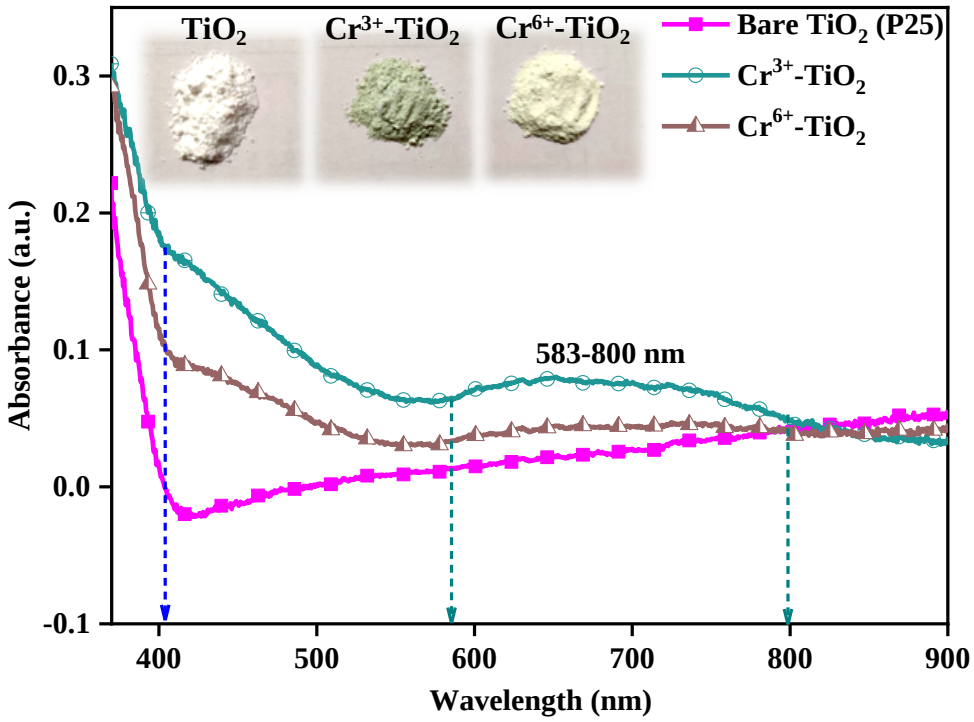

Figure 3.1. DRS spectra of various bare and Cr^{n+}-TiO_2 nanocatalysts.

Figure 3.1 represents the DRS spectra of different photocatalysts where TiO_2 absorption band below 400 nm (UV region) happens due to electron transfer from its valence band (V.B.) to the conduction band (C.B.). Further, loading of metal ions (Cr^{n+}) provided a hyperchromic shift to this band with simultaneous generation of bathochromic shifts covering the entire visible region up to 800 nm. The presence of Cr^{n+} ions yielded two absorption bands at 400-500 nm and 583-800 nm in Cr^{n+}-TiO_2 nanocomposites. The band at former visible region (400-500 nm) is ascribed to charge transfer movement from $Cr^{3+} \rightarrow Ti^{4+}$ species or $^4A_{2g} \rightarrow {}^4T_{1g}$ (d-d) transitions while the latter band at 580-800 nm has been credited to $^4A_{2g} \rightarrow {}^4T_{2g}$ transitions [25]. It has been observed that the absorption peak intensities are more pronounced in Cr^{3+} than Cr^{6+} oxidation state. This observation is believed to occur due to the presence of some parity forbidden transitions in d^0 system of Cr^{6+} ion compared to d^3 system of Cr^{3+} ion. Still, the incorporation of Cr^{6+} ions imparted some visible light harvest to the Cr^{6+}-TiO_2 nanocatalyst system due to LMCT charge transfer transitions ($O^{2-} \rightarrow Cr^{6+}$). It infers that impregnation of a particular element i.e. Cr^{n+} here in different oxidation states (Cr^{3+}/Cr^{6+}) appreciably effect the visible light sensitivity of prepared photocatalysts in different manner. Further, changes in the photocatalyst colour from white → green → yellow

confirms the impregnation of corresponding metal ions i.e. Cr^{3+} and Cr^{6+}, respectively (Fig. 3.1; inset).

In order to determine the fate of charge carrier recombination and defective sites on the catalyst's surface, the photoluminescence (PL) analysis was carried out (Fig. 3.2a). For this, all the catalysts were excited at an excitation wavelength of 340 nm to measure their emission spectra/bands. Various emission peaks at 399, 422, 448, 460 and 486 nm were detected. These peaks are assigned to emission of the excited band gap states (422 nm), defective sites due to presence of oxygen vacancies (448 and 460 nm) [26] and charge transfer between Ti^{3+} and oxygen anion in TiO_6^{2-} species (486 nm), respectively. The bands between 450-500 nm are mainly due to the recombination of photoexcited charge carriers.

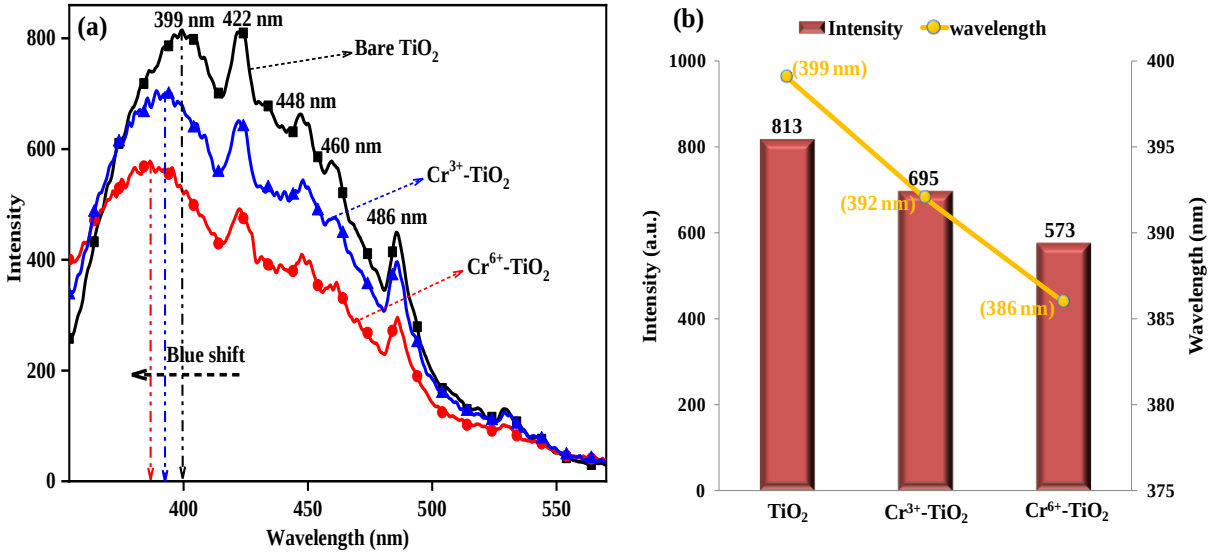

Figure 3.2. (a) Photoluminescence and (b) corresponding variations in peak intensities shown by different catalysts.

The complete PL spectra of bare TiO_2 and Cr^{n+}-TiO_2 catalysts reveal that impregnation of Cr^{n+} ions over TiO_2 led to the hypochromic as well as hypsochromic (blue shift) shifts of the emission peak intensities. A successive increment in the blue shift of emission spectra is witnessed due to variable and higher oxidation state of Cr^{3+}/Cr^{6+} ions which act as quencher and further lower the charge carrier relaxation rate. In this respect, variations in the PL peak (399 nm) intensities and their corresponding wavelength changes have been represented in figure 3.2b. Further, it has also been observed that Cr^{6+}-TiO_2 nanocomposites suffered greater quenching than bare or Cr^{3+}-TiO_2 photocatalysts. The above results are indicative of the fact that metal loading with higher oxidation state generates lesser recombination of e^--h^+ pair due to more generation of oxygen defective sites and alteration in the crystal structure of Cr^{n+}-TiO_2 nanocomposites [27,28].

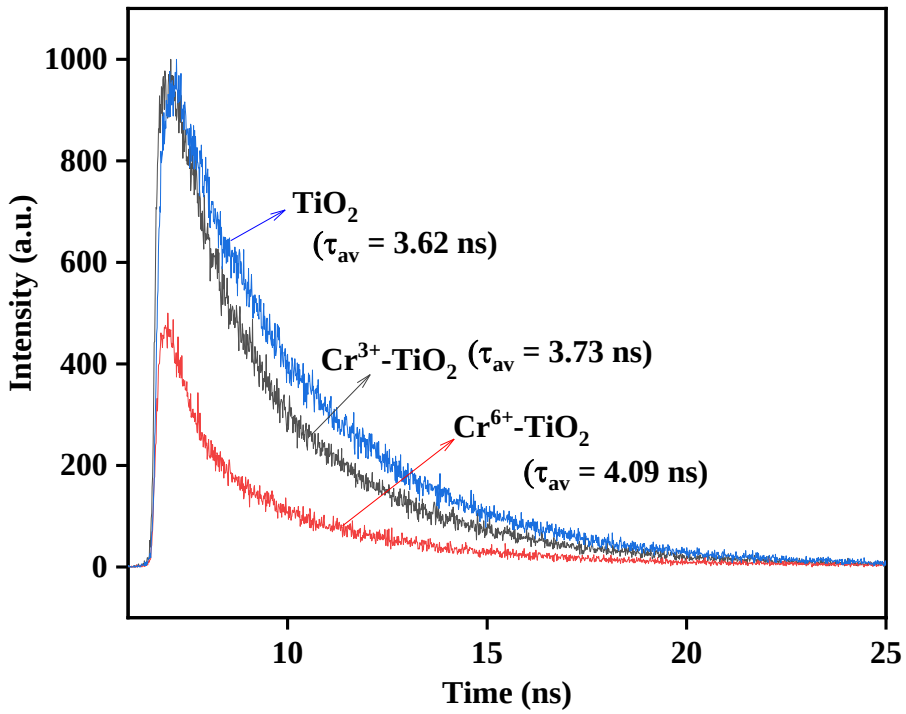

Figure 3.3. Time resolved decay spectra of bare and Cr^{n+} impregnated TiO_2 nanocatalysts.

The PL studies were further evidenced by the charge carrier relaxation dynamics of bare TiO_2 and Cr^{n+}-TiO_2 nanocomposites (Fig. 3.3). For the purpose, samples were exposed to an excitation wavelength of 340 nm and spectra were fitted using the bi-exponential decay function to obtain the intensity weighted average lifetimes. The average lifetimes (τ_{av}) and results obtained for different nanocatalysts have been calculated using the following equation and are listed in table 3.1.

$$\tau_{av} = \frac{\Sigma a_i \times \tau_i^2}{\Sigma a_i \times \tau_i}$$

where τ_1 and τ_2 are the fast and slow decay components, respectively while a_1 and a_2 are their respective emission amplitudes.

Table 3.1. Different parameters associated with the time resolve decay analysis of various photocatalysts.

Sr. No.	Catalysts	τ_{av} (ns)	a (pre-exponential constant)	χ^2	D.W. (Durbin-Watson)
1.	TiO_2	3.62	0.074	1.004	1.707
2.	Cr^{3+}-TiO_2	3.73	0.048	0.922	1.855
3.	Cr^{6+}-TiO_2	4.09	0.030	0.968	1.833

It has been observed that metal loading lowered the recombination rate to a significant extent. Many reports consider the charge carrier relaxation time to vary as a function of nanoparticle size, shape and type of metal used. But here, we report the changes observed as a consequence of variable oxidation states of the impregnated Cr^{n+} metal ions. The average lifetime of 3.62 ns was observed for bare TiO_2 which extended to 3.73 ns after Cr^{3+} loading and further up to 4.09 ns for Cr^{6+}-TiO_2 nanocomposites. It seems clear that the incorporation of a particular metal (Cr^{n+}) in its different ionic/oxidation states yield different outcomes. The above results make a clear indication that oxidation state does affect the charge carriers toward better diffusion and photocatalytic process [29]. The higher oxidation state is expected to create effective metal-TiO_2 heterojunction which suppresses the recombination rate enabling a longer carrier survival to participate in the oxidation-reduction reactions.

3.3.2. Surface structural/morphological properties

To determine the surface structural and elemental characteristics of the nanocatalysts, the SEM-EDS studies were done (Fig. 3.4). The elemental spectra revealed the presence of Ti, O and Cr elements in different Cr^{n+}-TiO_2 nanocomposites. However, no specific morphology was detected in the SEM images due to low resolution of the instrument.

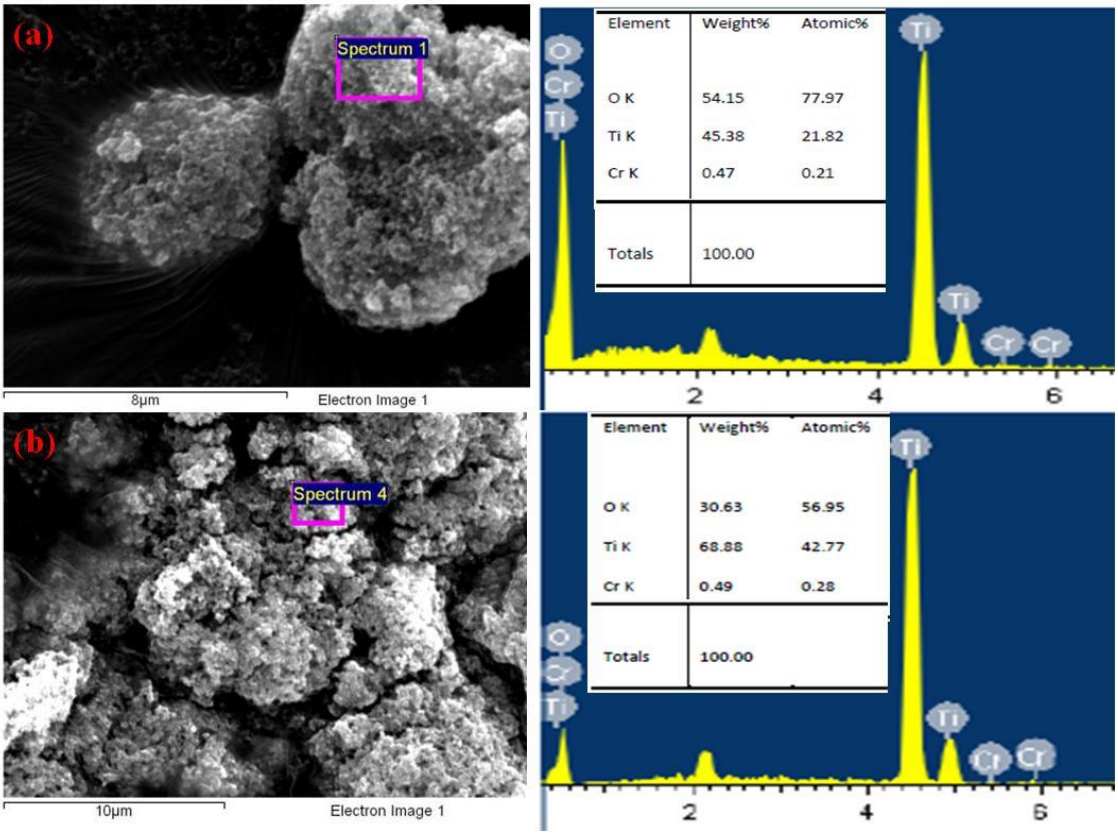

Figure 3.4. SEM and corresponding EDS pattern of (a) Cr^{3+}-TiO_2 and (b) Cr^{6+}-TiO_2 nanocomposites.

Therefore, in order to further confirm the morphological features, the HRTEM analysis was carried out. Figure 3.5 represents the morphology and size distribution of Cr^{3+}-TiO_2 nanocatalysts. The mixed nanocomposites of chromium and titanium were observed consisting of dark and light coloured NPs. The dark coloured NPs have been credited to the presence of Cr^{3+} species while the lighter ones have been assigned to the TiO_2 photocatalyst on the basis of their different electron densities (Cr; 7.19 g/cm^3 > Ti; 4.50 g/cm^3) (Fig. 3.5a-3.5c). The size of Cr^{3+} ionic species loaded at various locations varied from 9 nm to ~ 16-22 nm with spherical and rectangular morphologies. Further, the lattice fringes with inter planar distances of 0.18 and 0.30 nm have been assigned to the 200 and 220 planes of anatase TiO_2 and chromium, respectively while the inset represents the fast fourier transform (FFT) of the catalyst. The selected area electron diffraction (SAED) pattern evident the presence of 101 plane (d = 0.35 nm) of anatase phase of TiO_2 in addition to the above mentioned planes (Fig. 3.5e). On the other hand, the size distribution analysis obtained from HRTEM images showed that the average/mean particle size existed at 16.9 ± 1.0 nm for maximum number of NPs. It has been observed that maximum particle frequency remained below the size factor of ~ 25 nm for Cr^{3+}-TiO_2 nanocomposites.

Further, as per the structural features of the Cr^{6+}-TiO_2 nanocatalysts are concerned, figure 3.6a-3.6c explains the presence of mixed nanocomposites of Cr^{6+} ionic species with the TiO_2 NPs. The nanocatalysts size ranging 9 ~ 19 nm were associated with the rectangular and somewhat spherical kind of morphologies. The lattice fringes and SAED pattern both confirmed the presence of 101 (TiO_2; anatase), 110 (TiO_2; rutile) and 220 plane of chromium element (Fig. 3.6d and 3.6e). The very clear fringes pattern and associated FFT depict a well ordered arrangement of the atoms/elements possessed by the Cr^{6+}-TiO_2 nanocomposites. The average size as demonstrated by the figure 3.6f showed that maximum number of particles exhibited the size of 8.6 ± 0.4 nm which is almost half of what was possessed by the Cr^{3+}-TiO_2 nanocomposites. A careful examination of the catalyst images revealed not much variations in the sizes of the nanocomposites as a function of varying the oxidation state of the impregnated metal (Cr^{n+}; n = 3 or 6). However, after applying the size distribution function, it was detected that the maximum frequency of the NPs in Cr^{6+}-TiO_2 catalysts lie at or below 8.6 nm while in case of Cr^{3+}-TiO_2 catalyst, it remained at 16.9 nm. Therefore, it can be deduced that highly charged metal ionic species offered some new interfacial behaviour between the Cr^{n+} ionic specie and TiO_2 photocatalyst which led to reduced size of the nanocomposites.

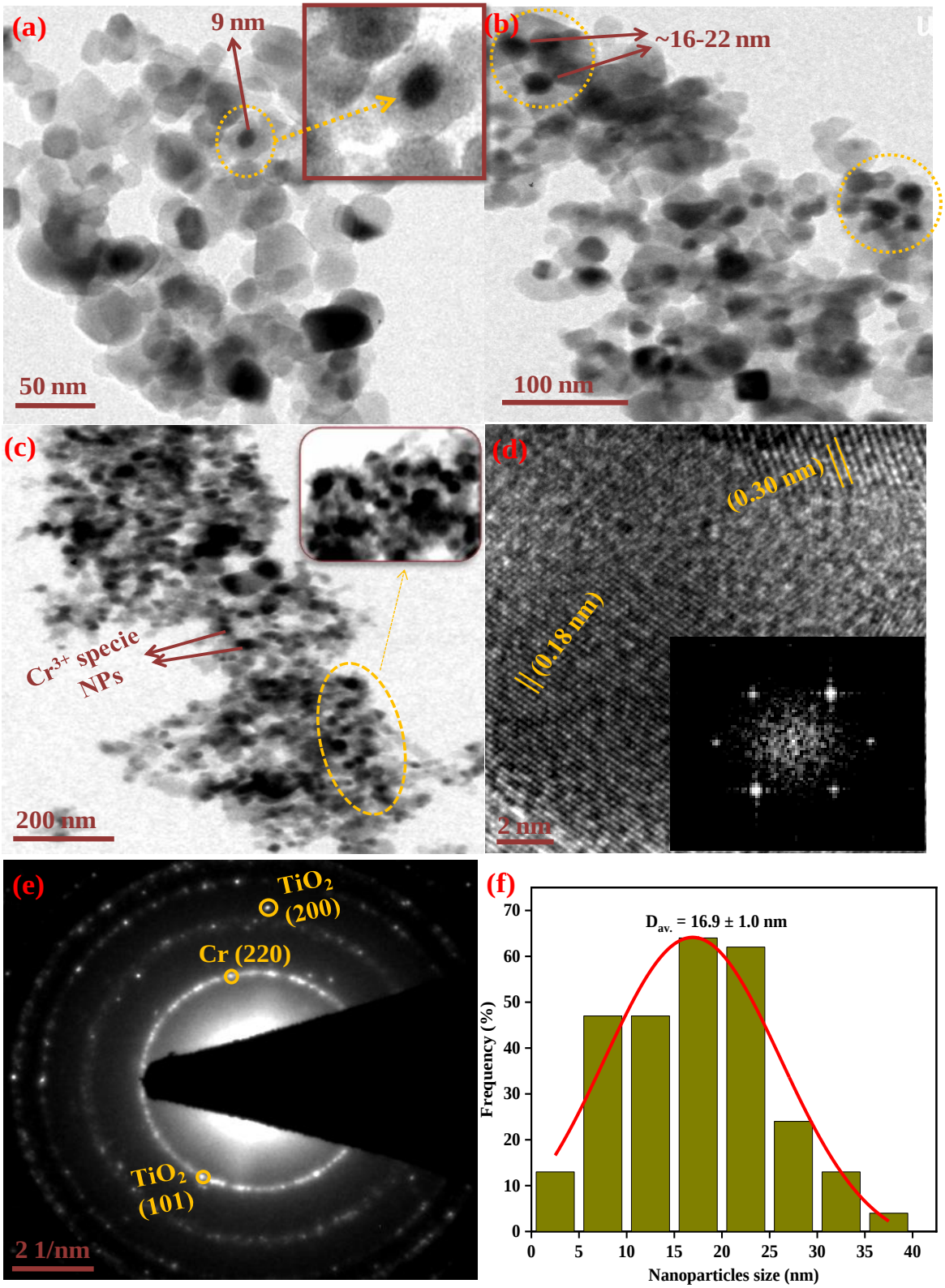

Figure 3.5. (a-c) Morphological, (d) fringes, (e) SAED pattern and (f) average particle size analysis of Cr^{3+}-TiO_2 nanocomposites.

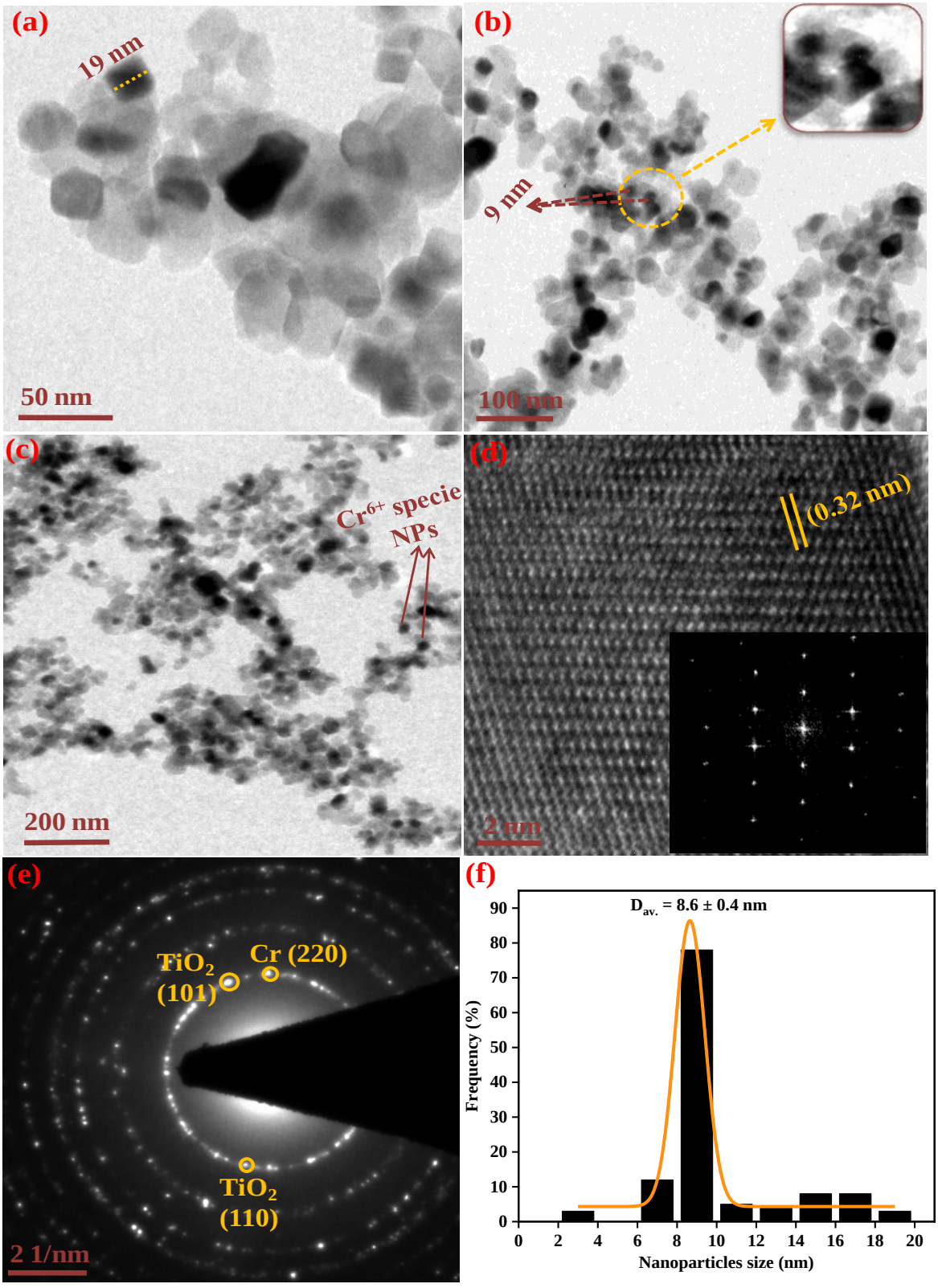

Figure 3.6. (a-c) different morphologies, (d) lattice fringes, (e) SAED pattern and (f) average particle size of Cr^{6+}-TiO_2 nanocatalysts.

3.3.3. Surface and electrokinetic properties

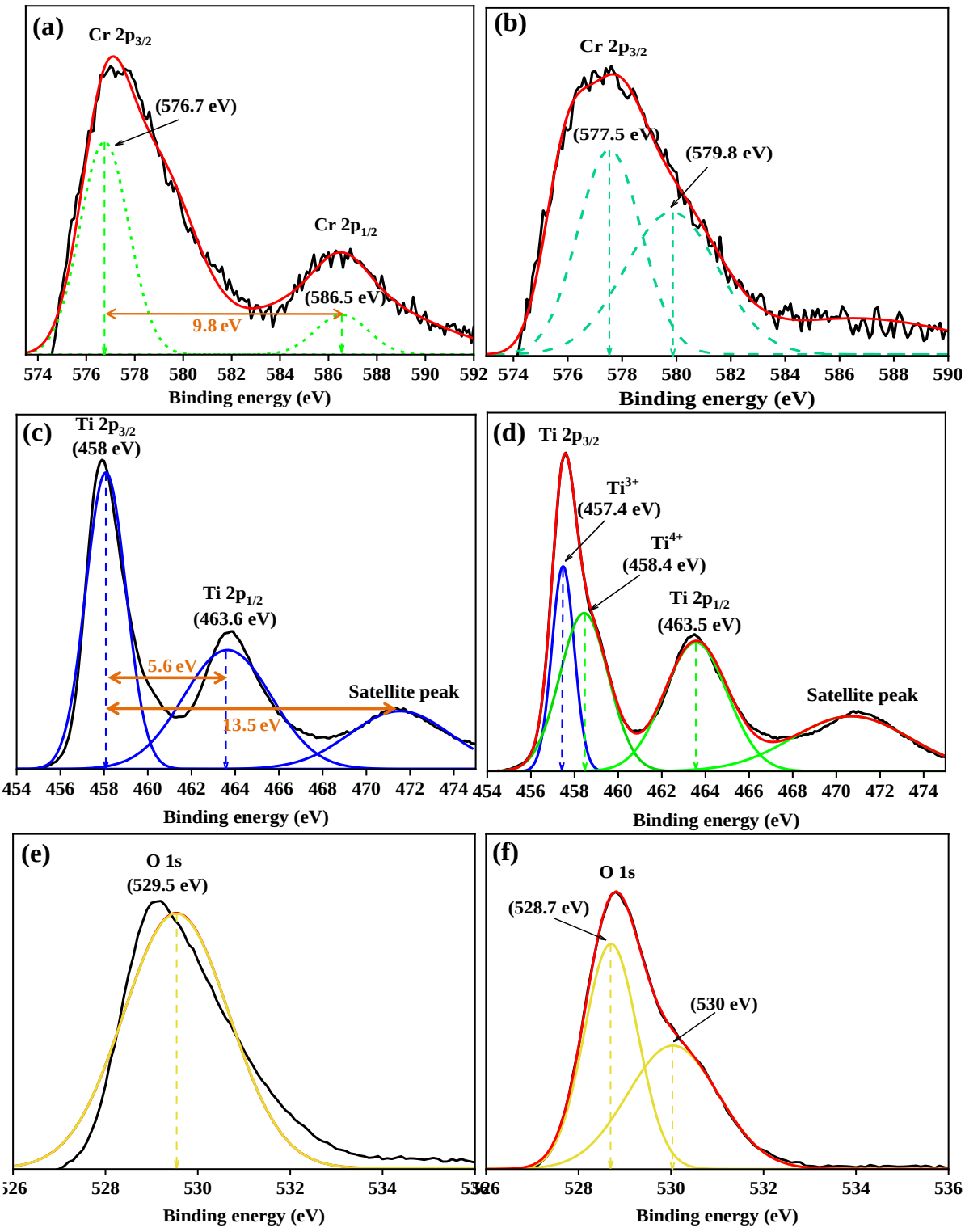

Figure 3.7. XPS analysis (a, c and e) of Cr, Ti and O elements in Cr^{3+}-TiO_2 and (b, d and f) in Cr^{6+}-TiO_2 nanocomposites, respectively.

The valence state of various elements in the prepared catalysts were examined using XPS analysis (Fig. 3.7). The Cr2p, Ti2p and O1s peaks of the Cr^{3+}-TiO_2 catalyst have been

represented in figure 3.7a, 3.7c and 3.7e, respectively. Two peaks for the two spin states of chromium i.e. $Cr2p_{3/2}$ and $Cr2p_{1/2}$ were witnessed at 576.7 and 586.5 eV, respectively [30]. These peaks occurred with a spin-orbit splitting factor of ~ 9.8 eV which is a characteristic feature of Cr^{3+} state. The titanium also showed two peaks at 458 and 463.6 eV for its two spin states ($Ti2p_{3/2}$ and $Ti2p_{1/2}$) with a small satellite peak at 471.5 eV. It has been observed that the energy difference of spin-orbit splitting between the two peaks of titanium existed at 5.6 eV while it occurred at 13.5 eV between the $Ti2p_{3/2}$ state and the satellite shake over. These energetics decipher the presence of titania in the form of Ti^{4+} as TiO_2 (13.3 eV) [31]. The smaller deviations from the actual splitting values are as expected due to different chemical environments, new heterojunction and Schottky barrier formation. The O1s peak for the same catalyst was detected at 529.5 eV which has been assigned to the O^{2-} species. Further, coming to the determination of oxidation states in the Cr^{6+}-TiO_2 catalyst, figure 3.7b, 3.7d and 3.7f represents the Cr2p, Ti2p and O1s spectra, respectively. It can be seen that chromium showed only one peak for the $Cr2p_{3/2}$ spin state encompassing two overlapped peaks at 577.5 eV and a smaller one at 579.8 eV. This peak at 579.8 eV and absence of $Cr2p_{1/2}$ spin state confirms the presence of Cr^{6+} oxidation state [32]. However, a small shoulder peak at 577.5 eV has been credited to the reduced form of chromium i.e. Cr^{5+}/Cr^{4+} states [33]. The titanium element showed peaks at 457.4, 463.5 and 470.6 eV for $Ti2p_{3/2}$, $Ti2p_{1/2}$ and satellite peak, respectively. The initial spin state comprises of an additional peak at 458.4 eV for Ti^{4+} species while earlier one at 457.4 eV has been detected for the Ti^{3+} oxidation state. Further, O1s peak existed at 528.7 eV with asymmetric tail at higher energy value of 530.0 eV. The position of oxygen peaks proclaimed the existence of some hydroxide or hydride ionic species also [34].

Table 3.2. The electrokinetic and hydrodynamic parameters of different nanocatalysts.

Sr. No.	Catalysts	Zeta potential (mV)	Streaming potential at 0.1% solution (mV)	Charge demand (μeq/g)	Hydrodynamic size (nm)
1.	TiO_2	-14.5	-57	1.12	220
2.	Cr^{3+}-TiO_2	-16.2	-222	13.4	425
3.	Cr^{6+}-TiO_2	-25.1	-295	18.9	343

The electrokinetic properties of different catalysts have been measured in terms of zeta, streaming potential and surface charge demand analysis. The zeta potential (mV) values for various nanocatalysts were obtained in the following manner: -14.5 (bare TiO_2) < -16.2 (Cr^{3+}-TiO_2) < -25.1 (Cr^{6+}-TiO_2). The increased oxidation state led to greater attraction of counter ions which induced higher magnitudes of zeta potential. These results suggest a significant stability possessed by the highly charged catalysts due to greater inter-ionic repulsions amongst them. Further, the flow of these counter ions was determined using streaming potential and charge demand studies. The streaming potential values were found to be consistent with the zeta potential measurements. The greater counter ion fluid flow pressure was possessed after Cr^{6+} loading (-295 mV) compared to Cr^{3+} (-222 mV) and bare TiO_2 (-57 mV) photocatalyst. Based on the streaming potential analysis, the surface charge demand (μeq/g) was also assessed as: 1.12 for bare TiO_2 which increases up to 13.4 after Cr^{3+} impregnation and further reaches to a maximum of 18.9 when Cr^{6+} was incorporated. The electrokinetic parameters of all the catalysts have been summarized in table 3.2. It has been concluded that higher oxidation state tends to impart greater charge demand as a consequence of greater attractions which is very useful for effective catalyst-substrate associations to bring them in closer vicinity of each other.

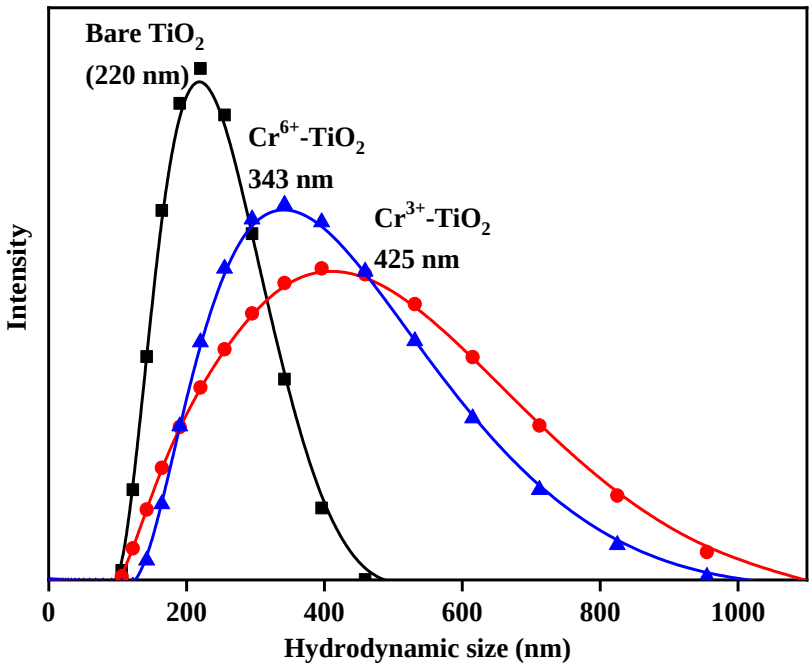

Figure 3.8. The DLS spectra of different bare and Cr^{n+} incorporated TiO_2 nanocatalysts.

Further, the hydrodynamic size of TiO_2 (220 nm) was found to get increased in Cr^{6+}-TiO_2 (343 nm) and Cr^{3+}-TiO_2 nanocomposites (425 nm) (Fig. 3.8). The increased size upon Cr^{n+} loading is attributed to the deposition of metal NPs over TiO_2 surface while different sizes shown by Cr^{3+}/Cr^{6+}-TiO_2 nanocatalysts are expected on the basis of variable ionic radii of Cr^{3+} (0.075 nm) and Cr^{6+} ions (0.058 nm).

3.3.4. Adsorption and photocatalytic properties

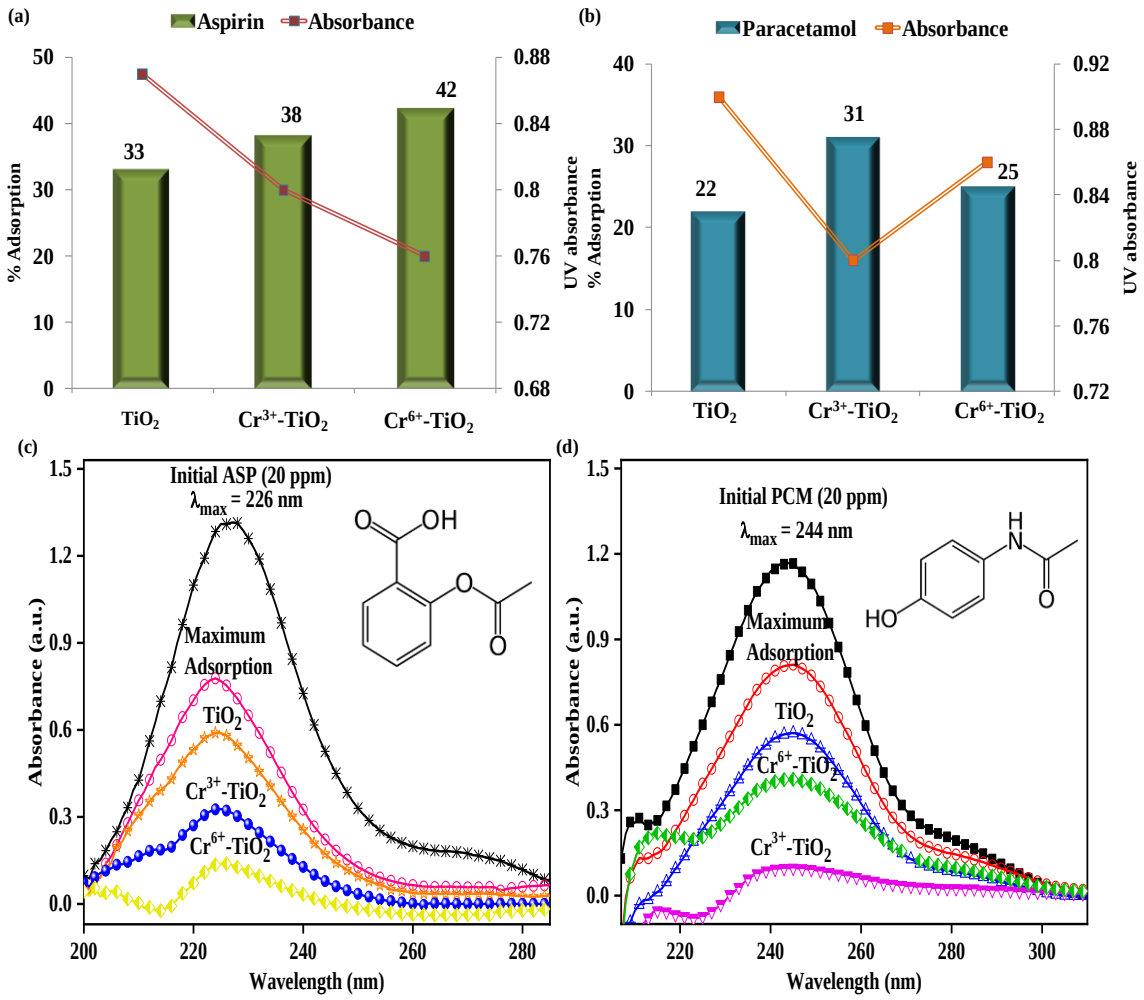

Figure 3.9. The adsorption (a) of aspirin and (b) paracetamol drugs onto different catalysts and (c and d) their respective degradations under solar irradiation.

The adsorption and photocatalytic degradation of aspirin and paracetamol drugs have led to some useful and interesting conclusions (Fig. 3.9). The adsorption tendency of different catalysts showed different kind of affinities depending on the structural aspects of the drug (substrate) molecules. For both the drugs, the Cr^{n+}-TiO_2 nanocomposites showed higher affinities as compared to bare TiO_2 photocatalyst. However, as far as the impact of different oxidation states is concerned, a reversed order has been detected by the Cr^{3+}/Cr^{6+}-TiO_2

catalysts. The highest adsorption capacity for ASP has been shown by Cr^{6+}-TiO_2 (42 %) while for PCM, it has been shown by Cr^{3+}-TiO_2 catalyst (31 %). The comparative adsorption capacities of various catalysts and corresponding decrease in UV peak intensities of ASP and PCM have been represented in figure 3.9a and 3.9b. Further, the photocatalytic degradation of ASP and PCM by different nanocatalysts followed the order similar to that of the adsorption as demonstrated in figure 3.9c and 3.9d. The maximum decrease in UV peak intensity of ASP by Cr^{6+} and PCM by Cr^{3+} impregnations revealed the existence of different kind of catalyst-substrate associations. Since, ASP and PCM bear different functional groups therefore, these are expected to offer different linkaging sites to the Cr^{n+}-TiO_2 nanocomposites. These photocatalytic reactions were performed for durations of 2 h for ASP and 3 h for PCM under natural solar irradiation. All the reactions were repeated for three consecutive days under solar intensities of 52.0, 52.5 and 52.6 mW/cm^2, respectively. The reaction parameters were found to follow the pseudo first order kinetics as per the following equation:

$$k = \frac{2.303}{t} \log \frac{C_0}{C_t}$$

where, k is the pseudo first order rate constant, t is the reaction time (min/h) and C_0 and C_t are the initial and final concentrations of the substrates (ASP and PCM). The observed reaction kinetics at different time intervals and related rate constants for the photodegradation of ASP and PCM have been shown in figure 3.10a and 3.10b, respectively. The rate constant, k (min^{-1}/h^{-1}) was calculated from the values of slopes (k/2.303) obtained from the respective graphs. The pseudo first order reaction kinetics are assumed due to two major factors. First, because the nanocatalysts are heterogeneous in nature and easily separable at the end of the reaction without getting consumed in it. Second, the concentrations of substrates used are in ppm (parts per million) which are very small compared to the solvent used.

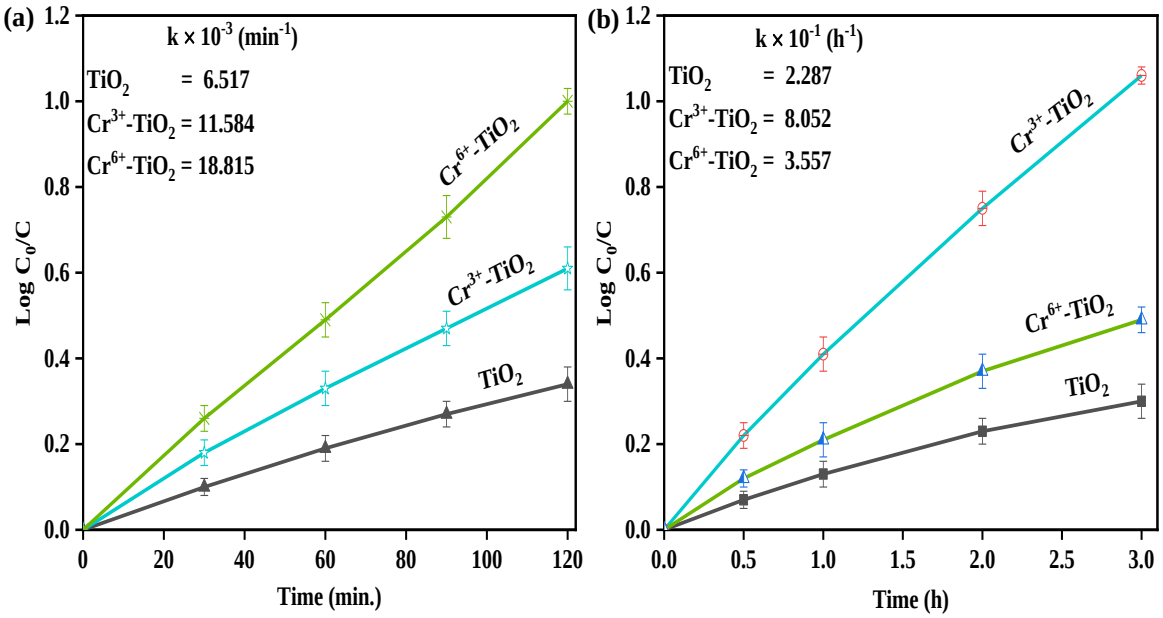

Figure 3.10. The observed reaction kinetics (a) of aspirin and (b) paracetamol using different nanocomposites at various time intervals under solar irradiation.

The different photodegradation performances of Cr^{3+} and Cr^{6+} ions loaded TiO_2 nanocomposites have been attributed to variable nature of the drug molecules. As in the ASP molecule, there are two functional group regions (carboxylic and ester) present. These groups tend to pull the electron density of the benzene ring towards themselves thereby making the oxygen atoms more negatively charged. The ortho effect makes the carboxylic group of the ASP molecule more acidic offering negatively charged oxygen atom for further co-ordination (Scheme 3.1). This negatively charged oxygen of the carboxylic group and the carbonyl oxygen of the ester group can co-ordinate with the catalyst surface through Cr^{6+} species and act as chelating ligands for the Cr^{6+}-TiO_2 nanocatalyst. This binding can thus increase the electrophilicity of the respective carbonyl carbons thereby making them more prone to attack by the nucleophiles and speed up the photodegradation process. These interactions are also correlated to the highly negative streaming and zeta potential values of the Cr^{6+}-TiO_2 composites. Many reports claim that the photodegradation process of ASP is usually slow due its tendency of complex formation with the water molecules. It has been evident from the present work that incorporation of highly charged metal ionic species can weaken the solvation energies to bring the photocatalytic success.

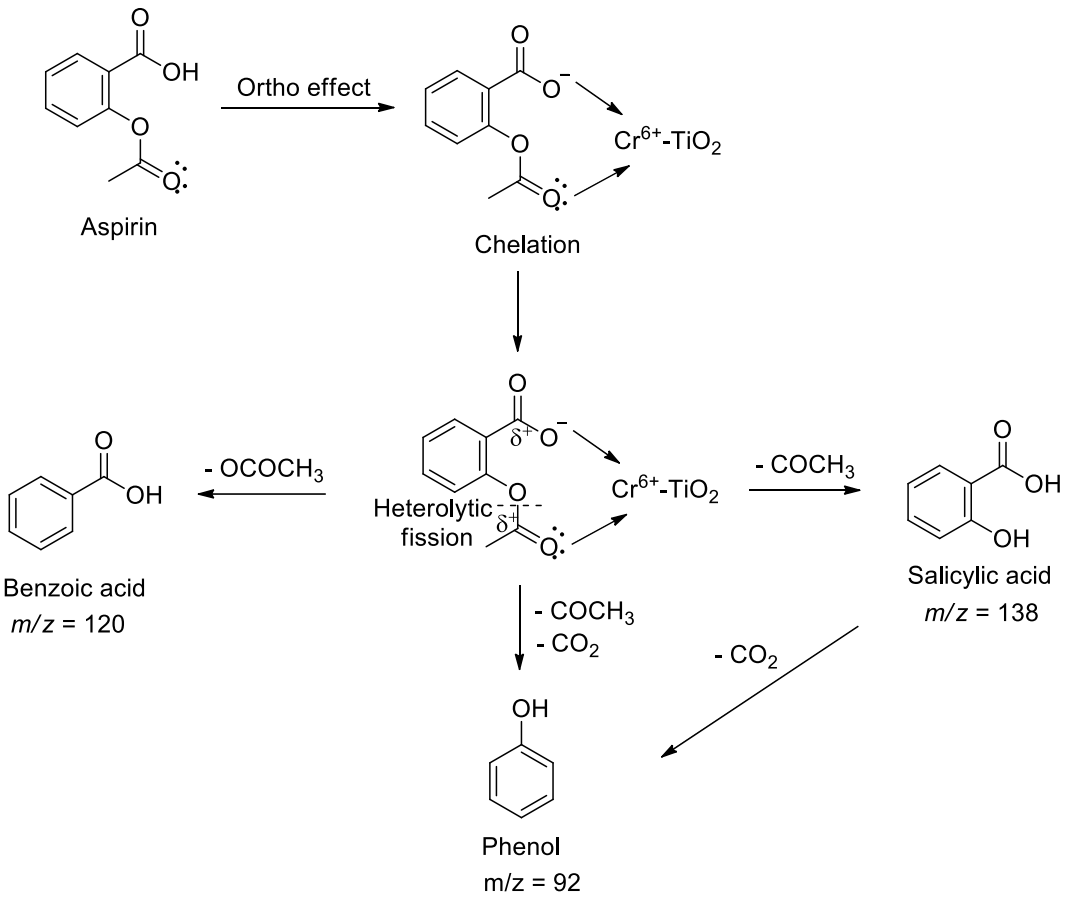

Scheme 3.1. The proposed mechanistic details regarding the interaction of aspirin and Cr^{6+}-TiO_2 nanocomposites and further degradation process.

To establish the degradation mechanism shown, the Gas Chromatography mass spectrometry (GCMS) of the degradation intermediates of aspirin was done as represented below:

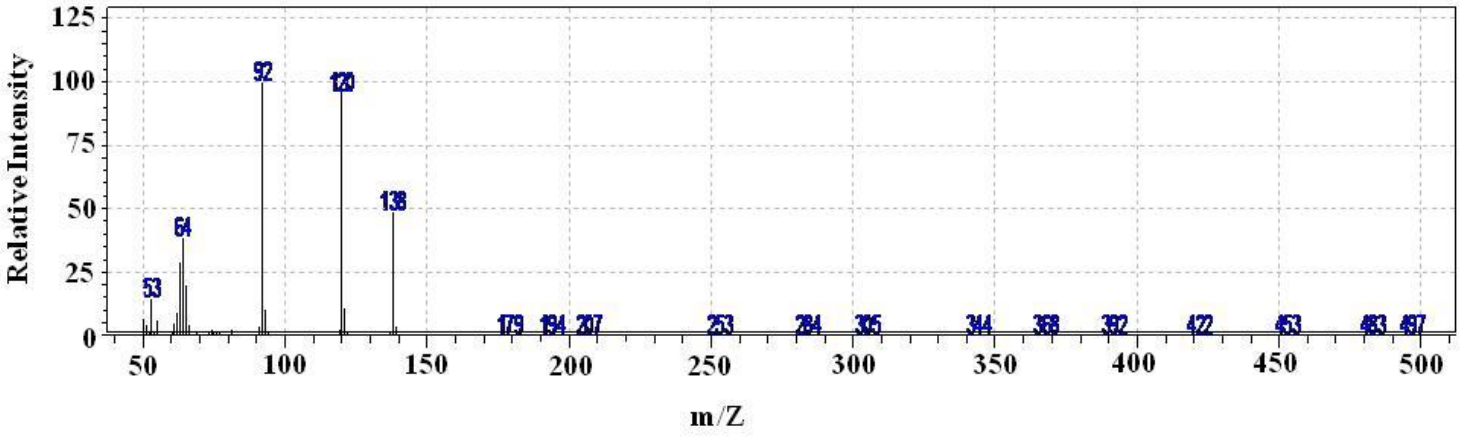

Figure 3.11. GCMS spectrum showing intermediate products obtained during the photodegradation of aspirin.

There exist a very negligible intensity of peak at m/z value of 179 for aspirin showing its degradation into further lower products. The species at 138 m/z and 120 m/z have assigned as salicylic acid and benzoic acid, respectively. Further, 92 m/z value has been credited to phenol/oxalic acid and other lower fragments have been considered to be formed from the hydroxylation of above obtained intermediates such as acetic acid, acetone or formic acid etc. There are other expected intermediates also which have not been detected in the spectrum might be due to their lower stability.

For PCM substrate, previous reports suggest that TiO_2 possess a preferential activity however, we have observed higher activity by both Cr^{6+} and Cr^{3+} impregnated TiO_2 catalysts. This observation has concluded us that higher degradations have not happened due to the presence of TiO_2 alone but Cr^{n+} ionic species also. The higher oxidation state cationic (Cr^{6+}) species were expected to impart greater photocatalytic behaviour for PCM also. But, Cr^{3+} has been found to exhibit higher degradations which can be explained on the basis of electron donating nature of the functional groups. There are two functional groups present; amide and hydroxyl oriented at para positions to each other (Scheme 3.2). The lone pair of electrons on both these groups can participate in conjugation with the benzene ring bearing slightly positive charge on their surface (structure I-III). This positive charge is highest in resonance structure III which can be responsible for lower interaction and activity by the Cr^{6+}-TiO_2 catalyst because of greater positive-positive charge repulsions than in Cr^{3+}-TiO_2 nanocatalyst.

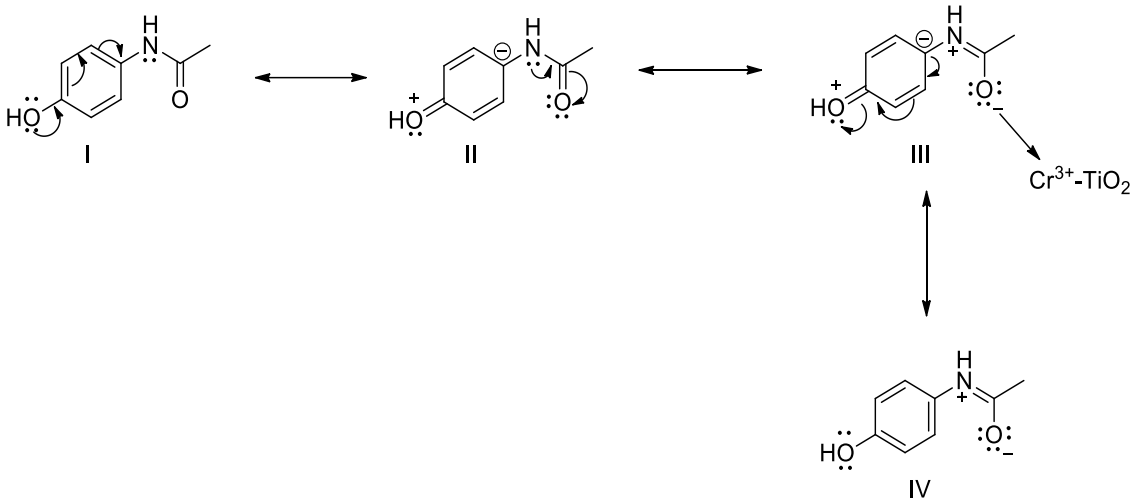

Scheme 3.2. Various resonance structures (I-IV) of paracetamol explaining the interaction with Cr^{3+}-TiO_2 nanocatalysts while repulsive behaviour with Cr^{6+}-TiO_2 nanocomposites (structure III).

References

[1] A. Zaleska, Recent Pat. Eng. 2 (2008) 157-164.

[2] M.I. Litter, Appl. Catal. B: Environ. 23 (1999) 89-114.

[3] S. Anandan, G.J. Lee, P.K. Chen, C. Fan, J.J. Wu, Ind. Eng. Chem. Res. 49 (2010) 9729-9737.

[4] N.L. Reddy, G.K. Reddy, K.M. Basha, P.K. Mounika, M.V. Shankar, Mater. Today: Proceedings 3 (2016) 1351-1358.

[5] H. Hassani, N. Nazarpour, G. Pourtaghi, Iran. J. Health Saf. Environ. 6 (3) (2018) 1281-1288.

[6] X. Zhao, W. Jin, J. Cai, J. Ye, Z. Li, Y. Ma, J. Xie, L. Qi, Adv. Funct. Mater. 21 (2011) 3554-3563.

[7] D.L. Liao, B.Q. Liao, J. Photochem. Photobiol. A: Chem. 187 (2007) 363-369.

[8] N. Kaur, S. Kaur, V. Singh, Desalination Water Treat. 57 (20) (2016) 9237-9246.

[9] J. Xiao, Y. Xie, H. Cao, F. Nawaz, S. Zhang, Y. Wang, J. Photochem. Photobiol. A: Chem. 315 (2016) 59-66.

[10] R. Zanella, E. Avella, R.M.R. Zamora, F.C. Barraza, J.C. Duran-Alvarez, Environ. Technol. 39 (18) (2018) 2353-2364.

[11] H. Zhang, G. Wang, D. Chen, X. Lv, J. Li, Chem. Mater. 20 (2008) 6543-6549.

[12] X.Z. Li, F.B. Li, Environ. Sci. Technol. 35 (2001) 2381-2387.

[13] Q. Wu, Q. Zheng, R. van de Krol, J. Phys. Chem. C 116 (2012) 7219-7226.

[14] T. Kaur, A. Sraw, A.P. Toor, R.K. Wanchoo, Sol. Energy 125 (2016) 65-76.

[15] J. Chen, M. Yu, C. Wang, J. Feng, W. Yan, Langmuir 34 (2018) 10187-10196.

[16] A. Syal, D. Sud, Sens. Actuators B: Chem. 266 (2018) 1-8.

[17] D.M. de Santiago Colin, L.A. Martinez-Chavez, A. Cuan, E.A. Elizalde-Pena, J.A. Rivera, C. Guzman, L. Escobar-Alarcon, K. Esquivel, J. Photochem. Photobiol. A: Chem. 364 (2018) 250-261.

[18] Y. Jiao, X. Chen, F. He, S. Liu, Chem. Eng. J. 372 (2019) 107-117.

[19] N. Gupta, B. Pal, J. Mol. Catal. A: Chem. 371 (2013) 48-55.

[20] S. Bhardwaj, B. Pal, J. Alloys Compd. 816 (2020) 152639.

[21] M. Kang, C.H. Lee, Appl. Catal. A: Gen. 266 (2004) 163-172.

[22] R. Ma, P. Hu, L. Jin, Y. Wang, J. Lu, M. Luo, Catal. Today, 175 (2011) 598-602.

[23] S.C. Petrosius, R.S. Drago, J. Chem. Soc., Chem. Commun. 4 (1992) 344-345.

[24] B. Pal, R. Kaur, I.S. Grover, J. Ind. Eng. Chem. 33 (2016) 178-184.

[25] Y.H. Peng, G.F. Huang, W.Q. Huang, Adv. Powder Technol. 23 (2012) 8-12.
[26] S.F. Chen, J.P. Li, K. Qian, W.P. Xu, Y. Lu, W.X. Huang, S.H. Yu, Nano. res. 3 (2010) 244-255.
[27] B. Choudhury, A. Choudhury, Mater. Chem. Phys. 132 (2012) 1112-1118.
[28] B.E.B. Al-Jumaili, Z.A. Talib, J.L.Y., S.B. Paiman, N.M. Ahmed, A.H.J. Al-Jumaily, A. Ramizy, S.A. Abdulateef, I.B. Muh'd, M.E.E. Mofdal, AIP Conf. Proc. 1733 (2016) 020019.
[29] C. Xue, S. Hu, Q. Chang, Y. Li, N. Li, C. Li, J. Yang, Mater. Res. Express 6 (7) (2019) 075014.
[30] T. Yan-Qing, Y. Meng, H. Yong-Mei, J. Phys. D 46 (1) (2013) 015303.
[31] I. Iatsunskyi, M. Kempinski, G. Nowaczyk, M. Jancelewicz, M. Pavlenko, K. Zaleski, S. Jurga, Appl. Surf. Sci. 347 (2015) 777-783.
[32] F.M. Capece, V. Di Castro, C. Furlani, G. Mattogno, C. Fragale, M. Gargano, M. Rossi, J. Electron Spectros. Relat. Phenomena 27 (2) (1982) 119-128.
[33] B. Liu, Y. Fang, M. Terano, J. Mol. Catal. A: Chem. 219 (2004) 165-173.
[34] X.Q. Li, J. Cao, W.X. Zhang, Ind. Eng. Chem. Res. 47 (2008) 2131-2139.

Conclusions and future aspects

Chapter 1

This chapter covers the various aspects in which metal/metal ions (M/M^{+n}) act as co-catalysts by influencing the catalytic and photocatalytic applications. The importance of oxidation states of these metals for the semiconductor materials and the effects of different preparation methods on these states have been discussed. The role and impact of oxidation states of M^{+n} co-catalysts on the catalyst's surface charge, electrokinetic and adsorption assisted photocatalysis has been disclosed. It has been concluded from various literature studied that different oxidation states of metal ions and further their different nature provide new and more efficient surface active sites and reaction pathways. Further, the characterization techniques employed such as diffuse reflectance spectroscopy, X-ray photoelectron spectroscopy, Transmission electron microscopy and surface charge analysis etc. have also been mentioned in detail in this chapter. The photocatalytic activity procedure adopted has also been presented schematically.

Chapter 2

Section 2A

This work described how the oxidation state, ionic size and nature of crystal structure of Mn^{+2} and Mn^{+7} co-catalysts impregnated onto TiO_2 affect the band energetics, electrokinetic, optical, surface adsorption and photocatalytic properties of Mn^{+n}-TiO_2 nanocomposites. Due to difference in net electronic surface charge build over Mn^{+2}-TiO_2 and Mn^{+7}-TiO_2 hybrid catalysts, the interaction and adsorption of cationic and anionic substrates significantly altered that governed the resulting photodegradation activity of fuchsin blue, methylene blue, salicylic acid and salicylaldehyde under visible light irradiation. It was observed that Mn(VII)-TiO_2 catalyst exhibit higher adsorption capacity (0.049 μmol) and photodegradation rates (0.015×10^{-3} and 0.126×10^{-3} min^{-1}) for cationic fuchsin blue and methylene blue dye, respectively, than Mn(II)-TiO_2 nanocatalyst under visible light irradiation.

It has been inferred that as highest oxidation state of any metal e.g. Mn^{+7} will not further oxidize, its loading will provide the fabrication of much stable photocatalysts with enhanced visible light sensitivity than the conventional metal co-catalysts. Thus, present finding reveal that various physicochemical properties of TiO_2 could be tuned by loading different metals

e.g. M = Cr, W, Os, Fe and Ru etc. having variable oxidation states and ionic size. Such M^{+n}-TiO_2 catalytic systems may be utilised for the selective and effective photodegradation of other harmful environment pollutants of different ionic nature under sunlight irradiation as well.

Section 2B

The present work emphasized the importance of surface structural properties and oxidation states for efficient co-catalysis imparted by Mn^{n+} ions. The adsorption-desorption studies using NH_3 gas revealed that Mn^{7+} ions generate enhanced Lewis acidity compared to Mn^{2+} impregnations. The best fit for Freundlich adsorption isotherm (K_f = 23.44 μg/mg) was possessed by Mn^{7+}-TiO_2 than Mn^{2+}-TiO_2 and TiO_2 photocatalysts confirming its higher substrate affinity and photodegradation efficiency. The Mn^{2+} and Mn^{7+} impregnations displayed 2.6 and 3.7 times higher photoactivity than bare TiO_2 which has been correlated to different oxidation states and surface structural properties imparted by Mn^{n+} ions.

On comparing the impact of impregnated Mn^{2+} and Mn^{7+} ions onto TiO_2, it was found out that higher oxidation state not only provides greater surface Lewis acidity but also the enhanced co-catalyst stability, adsorption and thus higher photodegradation ability. Many metals bear a variable range of oxidation states which can be exploited in this context for more interesting findings and future degradation of other toxic water/environment pollutants by inducing different catalyst-substrate associations.

Chapter 3

This work presented the effect of different oxidation states of Cr metal on charge carrier relaxation dynamics, optical and surface properties to further investigate the different adsorption and co-catalytic behaviour. The visible light sensitivity of TiO_2 photocatalyst extended from 400-800 nm upon Cr^{n+} co-catalyst loading. A remarkable quenching of photoluminescence peaks and further successive enhanced charge carrier relaxations from 3.62 ns (bare TiO_2) to 3.73 and 4.09 ns for Cr^{3+} and Cr^{6+} loaded TiO_2 catalysts were observed. It has been concluded that higher oxidation state significantly improve the recombination rate of charge carriers and surface charge demands. Apart from these, there are other parameters such as nature of substrate molecules, their functional groups, catalyst-substrate associations and their positions with respect to each other, etc. In this respect, this

study further confirmed that it is not only the surface structural and electrokinetic properties of the catalysts that matter but the chemical and nature of functional group attached to the substrate molecules also affect the photocatalysis mechanism.

In brief, this thesis demonstrates the importance of oxidation states as an important parameter needed to be considered while preparing a photocatalyst. Herein, the oxidation state effects of particularly Mn and Cr metals on the photophysical, electrokinetic, surface, crystallographic properties and adsorption-desorption equilibrium were investigated. The prepared catalysts were further employed for the degradation of differently charged substrates. It was found that apart from crystal structure and morphological factors which are usually given prior consideration, the oxidation state dependent surface charge demands, zeta and streaming potentials appreciably determine the fate of a photocatalytic process. Further, the substrate nature such as cationic/anionic or different functional groups present in its structure also influence the catalyst-substrate associations. Though, a detailed study has been done in this regard, still there are some points which could be followed to extend the research work.

There are so many metals such as Os, Sn, W, Re and Fe etc that exhibit a great variation in their oxidation states and are cost effective too. There are also charged substrate molecules which are otherwise non separable using neutral catalysts so, the oxidation states of these metals can be applied in this direction for environmental purposes. We have analyzed the catalytic oxidation properties of the prepared catalysts. However, the study of effect of variable oxidation states can be further continued for energy and other catalytic fields like hydrogen production and photoreduction reactions as well.

List of Publications

1. Sakshi Bhardwaj and Bonamali Pal, Effect of variable oxidation states of Mn^{+n} ion impregnated TiO_2 nanocomposites for superior adsorption and photoactivity under visible light. J. Alloys Compd. 816 (2020) 152639 **(IF = 4.65) (ISSN No. 0925-8388)**

2. Sakshi Bhardwaj and Bonamali Pal, Solar light driven photocatalytic oxidative degradation of methyl viologen using Mn^{2+}/Mn^{7+}-TiO_2 nanocomposites. J. Photochem. Photobiol. A 393 (2020) 112430 **(IF = 3.306) (ISSN No. 1010-6030)**

3. Sakshi Bhardwaj and Bonamali Pal, Oxidation state imparted improved charge carrier dynamics and catalyst substrate association for the degradation of drugs using Cr^{n+}-TiO_2 nanocomposites. (ready for submission).

Other Publications

1. Sakshi Bhardwaj and Bonamali Pal, Photodeposition of Ag and Cu binary co-catalyst onto TiO_2 for improved optical and photocatalytic degradation properties. Adv. Powder Technol. 29(9) (2018) 2119-2128 **(IF = 4.217)**

2. Sakshi Bhardwaj, Deeksha Dogra, Bonamali Pal and Satnam Singh, Photodeposition time dependant growth, size and photoactivity of Ag and Cu deposited TiO_2 nanocatalyst under solar irradiation. Sol. Energy 194 (2019) 618-627 **(IF = 4.608)**

3. Sakshi Bhardwaj, Diksha Sharma, Pooja Kumari and Bonamali Pal, Influence of photodeposition time and loading amount of Ag co-catalyst on growth, distribution and photocatalytic properties of Ag@TiO_2 nanocatalysts. Opt. Mater. 106 (2020) 109975 **(IF = 2.779)**

Conferences and workshops

1. Sakshi Bhardwaj and Bonamali Pal, participated in international Global Initiative for Academic Networks (GIAN) workshop on "Amphiphilic molecules and self-assembly: Principles and applications" held at Panjab University, Chandigarh on March 22-28, 2016.

2. Sakshi Bhardwaj and Bonamali Pal, Ag-Cu co-deposited TiO_2 photocatalyst: better synergy, crystallinity and efficient degradation rates; Thematic Conference in Chemical Sciences (TC_2S), IIT Ropar, 15-16 May, 2017 (Poster presentation).

3. Sakshi Bhardwaj and Bonamali Pal, attended the workshop on Intellectual Property Rights and Patenting at Thapar Institute of Engineering and Technology (TIET), Patiala on February 17, 2018.

4. Sakshi Bhardwaj and Bonamali Pal, Effect of variable oxidation states of Mn^{+n} ion impregnated TiO_2 nanocomposites for superior adsorption and photoactivity under visible light; 12^{th} National conference on Chemical and Environmental Sciences: Advanced Innovations-2020 (CESAI-2020), Punjabi University, Patiala, 19-20 February, 2020 (Poster presentation).

Journal of Alloys and Compounds xxx (xxxx) xxx

Contents lists available at ScienceDirect

Journal of Alloys and Compounds

journal homepage: http://www.elsevier.com/locate/jalcom

Effect of variable oxidation states of Mn^{+n} ion impregnated TiO_2 nanocomposites for superior adsorption and photoactivity under visible light

Sakshi Bhardwaj, Bonamali Pal*

School of Chemistry and Biochemistry, Thapar Institute of Engineering and Technology, Patiala, 147004, Punjab, India

ARTICLE INFO

Article history:
Received 11 July 2019
Received in revised form
25 September 2019
Accepted 9 October 2019
Available online xxx

Keywords:
Mn^{+n}-TiO_2 nanocomposites
Mn(II)/Mn(VII)–TiO_2 photocatalysts
Visible light sensitivity
Substrate adsorption specificity
Photocatalytic dye degradation

ABSTRACT

This paper deals with the importance of oxidation state and ionic size of Mn(II) and Mn(VII) co-catalyst impregnated TiO_2 for the observed electrokinetic, adsorption and photocatalytic properties of Mn^{+n}-TiO_2 nanocomposites. Due to difference in net electronic charge and ionic size of Mn(II) and Mn(VII) ions, the zeta potential, streaming potential and surface charge demand of Mn(II)–TiO_2 and Mn(VII)–TiO_2 nanocomposites are greatly varied. The absorption edge of Mn^{+n}-TiO_2 nanocatalysts revealed the red shift (515–550 nm) with increased oxidation state (from II to VII) of Mn^{+n} due to $^6A_{1g} \rightarrow {}^4T_{1g}$ transition. The photoluminescence (404–530 nm) of Mn(II)–TiO_2 is highly quenched relative to Mn(VII)–TiO_2 during 340 nm excitation. Further, the HRTEM analysis confirmed the presence of Mn(VII) (~20–45 nm) and Mn(II) (~40–60 nm) nanodeposits over TiO_2 surface. Binding energies at 639.1 and 640.3 eV showed the presence of Mn in (0) and (II) oxidation state for Mn(II)–TiO_2 and 646 eV alongwith a satellite peak for Mn(VII)–TiO_2 co-catalyst. As a result, the adsorption and photocatalytic degradation of cationic (Fuchsin blue and methylene blue) and anionic (Salicylic acid and Salicylaldehyde) pollutants by Mn^{+n}-TiO_2 nanocomposites are notably improved relative to bare TiO_2 depending on their respective oxidation state and surface morphological features.

1. Introduction

Noble Metal-TiO_2 nanocomposites offer a great deal of research interest due to their improved band energetics, optoelectronic and photocatalytic properties for solar energy conversions [1–6]. It has been found that metal-TiO_2 interfacial properties are strongly dependent on nature of metal, distribution of metal nanodeposits and preparation techniques e.g. photodeposition, doping and wet impregnation method etc [7]. Most of the preparation methods are associated with the reduction of metal ions into zero or lower valence state. However, in wet impregnation method, metals in their respective ionic state are loaded over support surface. These metal ions exhibit weak ionic or vander wall interactions with the semiconductor materials. This property of impregnation method can be better exploited to associate and photochemically process the charged/ionic substrate molecules which are otherwise difficult to remove. Under different preparation conditions, islands of metal/metal ion nanodeposits (1–100 nm) are either positioned on the TiO_2 surface or occupy the interstitial/substitutional sites. These metal deposits (0.1–2 wt%) act as co-catalysts by preventing the recombination rate of photogenerated charge carriers formed during the band gap excitation of TiO_2 by ultra violet light [8]. Generally, the work function difference between metal and TiO_2 lead to establishment of a helmholtz double layer at metal-TiO_2 interface due to fermi level equilibration with simultaneous formation of schottky barrier [9]. When the depletion/accumulation layer formed due to fermi level equilibration becomes equal to the photon penetration, maximum separation of electron-hole pair take place leading to highest photocatalytic efficiency.

Literature reveals that Au, Pt and Ag metals photodeposited onto TiO_2 exhibit higher and selective oxidation of benzene via electron depleted Au@TiO_2 catalyst [10–12]. In this method, no permanent bond exists between metal and TiO_2, but an association comprising ohmic/non-ohmic contact occurs. In another work, Fe^{+3} has been found to substitute Ti^{+4} species due to similar size of both ions ($Fe^{+3} = 0.064$ nm and $Ti^{+4} = 0.068$ nm) possessing maximum photoactivity for iodide oxidation to iodine [13]. Interstitially modified titania nanostructures by Ag metal show appreciable

* Corresponding author.
E-mail address: bpal@thapar.edu (B. Pal).

https://doi.org/10.1016/j.jallcom.2019.152639
0925-8388/

Journal of Photochemistry & Photobiology A: Chemistry 393 (2020) 112430

Contents lists available at ScienceDirect

Journal of Photochemistry & Photobiology A: Chemistry

journal homepage: www.elsevier.com/locate/jphotochem

Solar light driven photocatalytic oxidative degradation of methyl viologen using Mn^{2+}/Mn^{7+}-TiO_2 nanocomposites

Sakshi Bhardwaj, Bonamali Pal*

School of Chemistry and Biochemistry, Thapar Institute of Engineering and Technology, Patiala, 147004, Punjab, India

ARTICLE INFO

Keywords:
Mn^{2+}/Mn^{7+} co-catalysis
Mn^{n+}-TiO_2 photocatalysis
Influence of Mn^{n+} oxidation states
Methyl viologen degradation
Visible light sensitivity

ABSTRACT

Transition metal/metal ions are reported to impart very efficient co-catalytic activity to TiO_2 for various photocatalytic reactions depending on the nature and oxidation state of metal ions. However, when certain metals (M^{n+}) having different oxidation states like Mn^{2+}/Mn^{7+} or Cr^{3+}/Cr^{6+} act as co-catalysts, the photocatalytic properties of M^{n+}-TiO_2 nanocomposites may vary significantly. Different surface morphologies, electron transfer phenomena and adsorption efficacy provided by these co-catalysts will govern the M^{n+}-TiO_2 photoactivity. In this context, this paper demonstrates the preparation and characterization of Mn^{2+}/Mn^{7+}-TiO_2 nanocomposites for investigating the above physicochemical properties for the degradation of toxic herbicide Methyl viologen under sunlight irradiation. The optical spectra of these catalysts showed bathochromic shifts (from 355 to 572 nm) due to the presence of Mn^{2+} and Mn^{7+} ions. The higher co-catalyst stability, smaller D_{max} (maximum average diameter) and mixed morphological characteristics have been illustrated by SAXS and TEM analysis with size range ~ 25–30 and 20 – 35 nm for Mn^{2+}-TiO_2 and Mn^{7+}-TiO_2 nanocomposites, respectively. The adsorption-desorption studies using NH_3 gas revealed that Mn^{7+} ions generate enhanced Lewis acidity on the co-catalyst surface compared to Mn^{2+} impregnations. The best fit for Freundlich adsorption isotherm (K_f = 23.44 μg/mg) was possessed by Mn^{7+}-TiO_2 than Mn^{2+}-TiO_2 and TiO_2 photocatalyst confirming its higher substrate affinity and photodegradation efficiency. The Mn^{2+} and Mn^{7+} impregnations displayed 2.6 and 3.7 times higher photoactivity than bare TiO_2 which has been correlated to different oxidation states and surface structural properties imparted by Mn^{n+} ions.

1. Introduction

Metal ion (M^{n+}) based TiO_2 nanocomposites are believed to have better adsorption and photocatalytic properties than other conventional M^0-TiO_2 nanocatalysts [1–4]. The co-catalytic effect of these M^{n+}-TiO_2 nanocatalysts is considered to be the result of different oxidation states [5,6], surface charge density, isoelectric point, band energetics [7], electrokinetic [8] and interfacial electron transfer phenomena [9–11]. For example, metal ions Cr^{3+}, Fe^{3+} and V^{5+} impregnated TiO_2 photocatalysts have been found to have efficient photoredox properties [12,13]. Besides above, the impregnation method employed for the synthesis of these nanocomposites is simple, effective and does not require the use of any harmful UV radiations as in photodeposition method. Doped or impregnated metal ions are either located over the support surface or tend to occupy the interstitial sites depending on the ionic radii of metal ions [14]. The higher charge built over the surface of titania due to presence of metal ions also provide enhanced adsorption efficiencies rather than neutral metal atoms. In this regard, Fe^{3+}, Fe^0, Cu, Ag, Au^0, Au^{3+}, Cr^{3+} and Cr^{6+} have also been compared for iodide oxidation to iodine [15]. Various factors such as the oxidation state, ionic radii, catalyst surface acidity and electron affinity have been considered to influence the photocatalytic activity to a great extent [16–18]. Further, it has been established that appropriate doping of Sn^{4+} ions onto TiO_2 induces lower electron-hole pair recombination rate thereby increasing the degradation efficiency [19].

As solid-liquid heterogeneous photocatalysis is an interfacial phenomenon and depends upon the adsorption capability of the solid catalyst. Therefore, the photocatalyst adsorption efficiency/affinity is an important prerequisite to study. In a study, Al^{3+} modified TiO_2 nanocatalysts are found to offer appreciable adsorption efficacy for different kinds of dye molecules viz; rhodamine B, malachite green and alizarin red, etc [20]. Fe^{3+} and Pt^{4+} impregnated TiO_2 nanostructures of different shapes have also been evaluated for their adsorption behavior and photocatalytic oxidation of EBT dye under UV irradiation [21]. It was observed that the extra positive charge provided by metal ions facilitates greater interionic catalyst-substrate association enhancing

* Corresponding author.
E-mail address: bpal@thapar.edu (B. Pal).

https://doi.org/10.1016/j.jphotochem.2020.112430
Received 27 May 2019; Received in revised form 30 January 2020; Accepted 1 February 2020
Available online 08 February 2020

Advanced Powder Technology xxx (2018) xxx–xxx

Contents lists available at ScienceDirect

Advanced Powder Technology

journal homepage: www.elsevier.com/locate/apt

Original Research Paper

Photodeposition of Ag and Cu binary co-catalyst onto TiO_2 for improved optical and photocatalytic degradation properties

Sakshi Bhardwaj, Bonamali Pal *

School of Chemistry and Biochemistry, Thapar Institute of Engineering and Technology, Patiala 147004, Punjab, India

ARTICLE INFO

Article history:
Received 6 January 2018
Received in revised form 16 May 2018
Accepted 21 May 2018
Available online xxxx

Keywords:
Ag-Cu binary mixture
Co-catalytic effect
Visible light
Photodegradation

ABSTRACT

This paper deals with the influence of binary co-deposition of Ag and Cu metals on TiO_2 photocatalyst to investigate its adsorption, optical and photocatalytic properties relative to monometallic (Ag/Cu) deposition. Hence, different proportion of Ag and Cu has been simultaneously deposited on TiO_2 in an inert (argon) atmosphere under UV irradiations. It was found that the plasmonic absorption bands appeared in the visible region (480 and 640 nm for Ag and Cu, respectively) due to the binary deposition of Ag-Cu nanoparticles (~9–20 nm) onto TiO_2 surface as revealed by TEM size analysis and EDS/elemental mapping. The fluorescence spectrum of Ag-Cu-TiO_2 showed higher quenching of emission peak intensities at $\lambda > 450$ nm in a different extent due to efficient charge separation as compared to respective monometallic (Ag/Cu)-TiO_2 nanocomposites. The photocatalytic activities of binary Ag-Cu-TiO_2 for the degradation of methylene blue and salicylic acid under UV and visible irradiations were found to be notably higher than monometallic deposited TiO_2. The reaction rates and CO_2 formation exhibited due to binary deposition always gives enhanced photoactivity which could be useful for removal of toxic environmental pollutants under solar radiations.

1. Introduction

Coinage metals (Cu, Ag and Au) due to their strong surface plasmonic resonances (SPR) and fascinating electrical conductivities have been a matter of great interest [1]. In this respect, these metals have been used in different sizes, shapes and forms to modify the optical and surface properties of TiO_2 photocatalyst [2,3]. These metals owing to their suitable redox potentials (Cu = 0.337 eV, Ag = 0.799 eV and Au = 1 eV) have been photodeposited on TiO_2 surface and explored for various environmental photocatalytic applications. For example, Au, Pd and Pt metals have been photodeposited on mesoporous RuO_2-TiO_2 for CH_3OH oxidation in which RuO_2-TiO_2 composites containing Au showed significant photonic efficiency in visible light compared to Pd and Pt deposited catalysts [4]. Similarly, the Ag and CuO modified TiO_2 nanoparticles (NP's) have been considered as efficient electron scavangers for the photooxidation of phenol and acetic acid [1]. Also, the various Cu, Ag, Au and Pt modified TiO_2 nanocomposites have been reported to explore the effective oxidation-reduction pathways [5,6]. Among these metals, Au assisted nanoparticles (NP's) have been studied a lot due to their easy preparation, homogeneity and strong optical absorption properties. Previous reports of metal-TiO_2 nanocomposite preparation have discussed single metal deposition and their interfacial parameters affecting the photocatalytic activities. However, binary deposition of metals has been rarely found which may lead to the generation of dual and different interfacial charge transfer process.

The bimetallic nanostructures often exhibit better synergistic catalytic performance over their monometallic counterparts and, hence, they are useful in many applications [7]. However, to further improve the photocatalytic activity, the co-modified binary metallic catalysts have been prepared and Au and Pd co-modified TiO_2 bimetallics have been utilized for the degradation of malathion, a water polluting pesticide [8]. Au and Ag metal in combination with each other have been found to show appreciable oxidation reactions. The Ag-Au binary nanocomposites have been found to have higher rates (~2 times) for nitroaromatics reduction than their monometallic counterparts [9]. Ag-Cu co-impregnated on surface of TiO_2 are proven to be the efficient catalysts for the degradation of C.I. Acid orange 7 than their corresponding monometallic catalysts [10]. The TiO_2-supported Au-modified Ir catalysts have been utilized for the selective reduction of α-β unsaturated carbonyl compounds [11]. Thus, the literature observation reveals that appropriate metal selection to have maximal synergy, their electronic configuration, nature of support,

* Corresponding author.
E-mail address: bpal@thapar.edu (B. Pal).

https://doi.org/10.1016/j.apt.2018.05.020

Solar Energy 194 (2019) 618–627

Contents lists available at ScienceDirect

Solar Energy

journal homepage: www.elsevier.com/locate/solener

Photodeposition time dependant growth, size and photoactivity of Ag and Cu deposited TiO_2 nanocatalyst under solar irradiation

Sakshi Bhardwaj, Deeksha Dogra, Bonamali Pal*, Satnam Singh

School of Chemistry and Biochemistry, Thapar Institute of Engineering and Technology, Patiala 147004, Punjab, India

ARTICLE INFO

Keywords:
Ag-Cu@TiO_2 photocatalyst
Photodeposition time
Nanoparticle growth
Dye photodegradation
Solar irradiation

ABSTRACT

Ag and Cu metals due to their strong surface plasmons and visible light sensitivities have been incorporated with TiO_2 for various solar applications. But the effect of mutual interaction between these two metals and role of photodeposition (PD) time has not been studied which may bring new interfaces, more photonic absorptions and photocatalytic activities. So, the present work focuses not only on the enhanced photoactivity of binary deposition of Ag and Cu metal onto TiO_2 compared to their monometallic counterparts but on the importance of wt % and PD time as well. The higher activity possessed by the binary metal deposited TiO_2 catalyst has been credited to greater interfacial contact region, optimized photodeposition time and enhanced absorptions in the visible region. Further, Ag-Cu@TiO_2 photocatalyst was optimised by varying the wt% and PD time (15, 30, 60 and 90 min.) of deposited metals. It was observed that with increase in PD time, the DRS intensity (400–700 nm) also increased in the respective manner. It has been established that the co-catalyst size and growth of nanoparticles (evidenced by TEM, EDS and DLS analysis) play a major role which vary as a function of UV irradiation time during preparation of nanocatalyst. Consequently, Ag-Cu@TiO_2 co-catalyst prepared at 30 min PD time has been shown to have maximum co-catalytic activity for the degradation of neutral red ($k \times 10^{-3} = 0.061\ min^{-1}$) and phenol red ($k = 0.028\ min^{-1}$) dyes under solar irradiation which has been attributed to the controlled growth and well dispersed Ag-Cu nanodeposits.

1. Introduction

Noble metal-TiO_2 photocatalysts have pulled in a lot of consideration over recent years (Chatterjee et al., 2012; Muller and Pratsinis, 2016). Metal loading on the surface of TiO_2 not only lead to red shift absorption of solar spectrum but decreases the recombination rate of generated charge carriers also. Different metals such as Pd, Pt and Au etc. have been used in different interesting ways to enhance the photocatalytic efficiency of TiO_2 photocatalyst. For example, Pd, Pt and Au have been photodeposited onto mesoporous RuO_2-TiO_2 where Au modified catalysts showed remarkable photonic efficiency for CH_3OH oxidation (Ismail et al., 2012). Plasmonic metals such as Au, Cu and Ag due to their strong surface plasmonic resonances (SPR), suitable redox potentials and easy reducible nature on the surface of TiO_2 make their utility more reproducible (Pascucci et al., 2014; Liu et al., 2014).

$$Ag^{+} + e^{-} \rightarrow Ag\,(E^{\circ} = 0.799\ V)$$

$$Cu^{+2} + 2e^{-} \rightarrow Cu\,(E^{\circ} = 0.337\ V)$$

In this respect, these metals have been photodeposited onto TiO_2 and have been applied for various photocatalytic application purposes. For example, under visible light irradiation Ag modified TiO_2 nanoparticles have been viewed as good photocatalysts for the degradation of Rhodamine B (Xiang et al., 2010). In another study, Cu, Ag and Au-TiO_2 catalysts have been compared for the degradation of methylene blue dye and activity order has been found in manner: Cu-TiO_2 > Au-TiO_2 > Ag-TiO_2 (Sangpour et al., 2010).

Apart from doped frameworks, the composite nanostructures (binary/bimetallics) may combine the unique properties of semiconductors and noble metals/magnetic metals demonstrating multifunctional behaviors (Monga et al., 2017; Rojas et al., 2015). However, the simultaneous and effective control of morphology, structure, composition and distribution of metal nanoparticles is still a major concern. There exist several reports on the effective photocatalytic activity of binary metal doped TiO_2 nanoparticles. For example, effective aerobic oxidation has been attributed to the efficient charge separation on the Pt-Cu/anatase interface due to decrease in schottky barrier (Shiraishi et al., 2013). Au-Ag modified TiO_2 NP's have been proven to be effective photocatalysts for benzyl alcohol oxidation due to high thermal stability, tailorable shape and size of the catalysts (Guan et al., 2013).

* Corresponding author.
E-mail address: bpal@thapar.edu (B. Pal).

https://doi.org/10.1016/j.solener.2019.10.055
Received 22 July 2019; Received in revised form 17 October 2019; Accepted 20 October 2019
Available online 12 November 2019

Optical Materials 106 (2020) 109975

Contents lists available at ScienceDirect

Optical Materials

journal homepage: http://www.elsevier.com/locate/optmat

Influence of photodeposition time and loading amount of Ag co-catalyst on growth, distribution and photocatalytic properties of $Ag@TiO_2$ nanocatalysts

Sakshi Bhardwaj, Diksha Sharma, Pooja Kumari, Bonamali Pal *

School of Chemistry and Biochemistry, Thapar Institute of Engineering and Technology, Patiala, 147004, Punjab, India

ARTICLE INFO

Keywords:
Ag co-catalysis
Particle size distribution
Effect of photodeposition time
Salicylic acid
Photocatalytic degradation

ABSTRACT

The activity of different wt% Ag co-catalyst over TiO_2 surface under varying UV illuminations (30, 60 and 90 min) for the photodegradation of salicylic acid has been studied. A considerable red shift in the plasmon band was observed with a significant color change (white to light brown) with increased photodeposition time (30–90 min) of Ag over TiO_2. Further, the elemental mapping confirms a continuous increase in the wt% of Ag with increased deposition time from 30 min (0.21 wt%) to 90 min (1.69 wt%). These 1, 3 and 5 wt% Ag deposited nanocatalysts prepared at 90 min duration showed higher activity for the photodegradation of salicylic acid under UV light irradiation compared to their counter parts of 30 and 60 min. The higher rate constant ($k = 2.73 \times 10^{-2}$ min^{-1}) value shown by (5 wt% $Ag)_{90}@TiO_2$ is appreciably higher compared to (1 wt% $Ag)_{90}@TiO_2$ ($k = 2.29 \times 10^{-2}$ min^{-1}) and (3 wt% $Ag)_{90}@TiO_2$ ($k = 2.33 \times 10^{-2}$ min^{-1}) photocatalyst and followed pseudo first order kinetics. The maximum activity of (5 wt% $Ag)_{90}@TiO_2$ catalyst has been credited to higher size, number and distribution of Ag co-catalyst nanoparticles over TiO_2 surface which greatly vary with change in amount and photodeposition time of Ag nanoparticles.

1. Introduction

The unique optical properties of plasmonic metals (M = Cu, Ag and Au) related to collective oscillations of their surface electrons are known as surface plasmonic resonance (SPR) [1–3]. This property renders these metals greater importance in recent times and have been used in different shapes, sizes [4] and forms to further improve the optical and surface properties of TiO_2 photocatalyst. These metals are when photo deposited (Au, Ag, Cu) create traps to capture the photo-induced electrons leading to the formation of reduced metal species on the surface of TiO_2. The increased absorption capability of these $M@TiO_2$ nanoparticles is a consequence of strong SPR effect which leads to electron transfer from metal to the conduction band (CB) of TiO_2. Among these, Au-TiO_2 photocatalysts have been considered to be efficient for environmental [5], water splitting and other energy storage applications. Since, the SPR band of Au NPs depends largely on morphology, size and chemical environment, therefore modification of any of these properties is considered to affect the frequency of plasmon band [6], surface structural and interfacial properties. In this concern, the Falaras and co-workers reported the degradation of azo-dye (methyl orange) two times faster using Au-TiO_2 thin films [7,8] compared to bare TiO_2. Lu and co-workers also reported the phenol oxidation and chromium reduction using mesoporous Au-TiO_2 nanocomposites by varying Au loading amount [9]. Further, Gupta and co-workers also reported the photocatalytic hydrogen production [10,11] using Au modified TiO_2 NPs. Apart from these, the optical absorption, surface structure and particle size of the metallic species have also been established to play an important role in the photocatalytic activity of TiO_2 under visible-light irradiation [12].

Besides various advantages, the higher cost of Au metal makes its use limited and scarce. On the other hand, Cu and Ag nanocomposites are gaining much attention due to their cost effective precursors, easy availability and suitable reduction potentials ($Cu^{+2} = 0.337$ V and $Ag^{+} = 0.799$ V). Literature reveals that the photodeposited Ag over TiO_2 greatly enhances the co-catalytic activity than in oxidised form (Ag^{+}) such as the degradation of malic acid [13]. Ag-TiO_2 thin films have been proven to decolourize the methyl orange much efficiently [14,15]. Apart from pollutant treatment, Ag-TiO_2/Ag/a-TiO_2 based nanocomposites have also been observed to efficiently degrade *E.coli* bacteria [16]. It was observed that the bactericidal effect of these composites was 5.1 times

* Corresponding author.
E-mail address: bpal@thapar.edu (B. Pal).

https://doi.org/10.1016/j.optmat.2020.109975
Received 28 March 2020; Received in revised form 28 April 2020; Accepted 30 April 2020
Available online 12 May 2020
0925-3467/